UNIVERSITÀ DEGLI STUDI DI PADOVA

Corso di Laurea Magistrale in Ingegneria Energetica

Tesi di Laurea Magistrale

WATER VAPOUR IN METALLIC VACUUM SYSTEMS: MODELLING AND EXPERIMENTAL STUDIES FOR THE LHC INJECTOR CHAIN

Relatore: **Prof. Paolo Bettini**
Dipartimento di Ingegneria Industriale

Correlatore: **Prof. Piergiorgio Sonato**
Dipartimento di Ingegneria Industriale

Correlatori: **Paolo Chiggiato**, **Jose Antonio Ferreira Somoza**
CERN Vacuum, Surface and Coatings Group

Laureando: **Riccardo Renzi**

Matricola: **1034774**

Anno Accademico 2013 - 2014

Ai miei genitori,

"Now this is not the end.
It is not even the beginning of the end.
But it is, perhaps, the end of the beginning."

Winston Churchill, 1942

Acknowledgements

I would like to thank Prof. Paolo Bettini and Prof. Piergiorgio Sonato, for their support during this Technical Student program at CERN.

I would like to express my deepest appreciation to Paolo Chiggiato and Jose Antonio Ferreira Somoza who gave me the opportunity to work at CERN and continually guided me during my internship. The incredible passion and depth they put into their scientific work has been inspirational and fundamental.

I would like to thank Roberto Kersevan, Chiara Pasquino, Mauro Taborelli for useful discussions; Nicholas Zelko, Berthold Jenninger, Sophie Meunier, Philippe Lançon, Ivo Wevers for their patience and assistance with the experimental set-up; Jean Philippe Rigaud and Mounir Driss Mensi for providing surface analysis measurements; Marina Malabaila for the asap cleaning and electropolishing treatments; Antonios Sapountzis and all the people from bdg. 181 for performing the silver-palladium coating.

Ringraziamenti

Vorrei ringraziare brevemente tutti coloro che mi hanno aiutato ed incoraggiato durante il percorso di laurea. Il ringraziamento piú grande va ai miei genitori: grandi ispiratori, motivatori e spettatori paganti del mio cammino. Senza i loro sacrifici niente di tutto ció sarebbe stato possibile.
Un grazie alla mia famiglia ed ai miei fratelli, che mi hanno sempre aiutato e confortato nei momenti del bisogno.
Un grazie agli amici di sempre [cit. Dott. Giulio Umbrella], agli amici di Parigi ed a quelli di Ginevra per il sostegno costante ed il divertimento assicurato.
Infine ringrazio la mia Amica Elena, che mi é stata vicina in ogni momento e che (di nascosto) ha messo qualcosa di suo in questa laurea.

Abstract

The study hereafter was aimed at the comprehension of water desorption from metal vacuum chambers. This phenomenon is considered the main obstacle for a fast achievement of UHV (Ultra High Vacuum) pressures in the LHC injectors. Although they have been studied for more than 40 years, water molecules interactions with metal vacuum chambers are still poorly understood. In this thesis, a numerical model for the calculation of pressure evolution has been analysed. This model simulates water desorption through the implementation of three different adsorption isotherms (Freundlich, Temkin and Sips) and hydrogen outgassing using a diffusive model. A set of experimental measurements at different temperatures have been performed on four stainless steel chambers. These have been differently treated: cleaned for UHV, air-baked, silver-palladium coated, vacuum fired followed by electropolishing.

Furthermore, the opportunity of improving the vacuum by adding five NEG lump pumps in the most radioactive sector of the SPS (LSS1) has been analysed. To do this, a numerical model based on electrical network analogy has been created.

Sommario

L'obiettivo dello studio seguente è la comprensione del desorbimento del vapore acqueo da parte di camere da vuoto metalliche. Questo fenomeno è ritenuto il principale ostacolo all'ottenimento di pressioni di Ultra Alto Vuoto negli iniettori del Large Hadron Collider (LHC). In questa tesi, viene proposto un modello numerico per simulare la discesa di pressione nei sistemi da vuoto. Tale modello include il desorbimento di acqua, simulato attraverso tre isoterme di adsorbimento (Freundilich, Temkin e Sips) ed il degassaggio di idrogeno, simulato come processo diffusivo.

È stata eseguita una campagna sperimentale, con misure a diverse temperature, in quattro camere di acciaio austenitico trattate differentemente: una pulita per applicazioni di Ultra Alto Vuoto, una air-baked, una vacuum fired e successivamente elettropulita, una rivestita di palladio-argento.

Infine è stato analizzato l'effetto dell'aggiunta di cinque pompe NEG nel settore più radioattivo dell'SPS, tramite un modello numerico basato sul metodo della rete elettrica equivalente.

Contents

List of Figures

Chapter 1

Introduction

This thesis is the result of the work carried out during one-year project at the European Organization for Nuclear Research (CERN) in Geneva, Switzerland. At CERN, the world's largest particle accelerator is used by physicists to study the basic constituents of matter - the fundamental particles. The particles are accelerated close to the speed of light and their collision is studied in the detectors. The process gives clues about how the particles interact each other, and provides insights into the fundamental laws of nature.

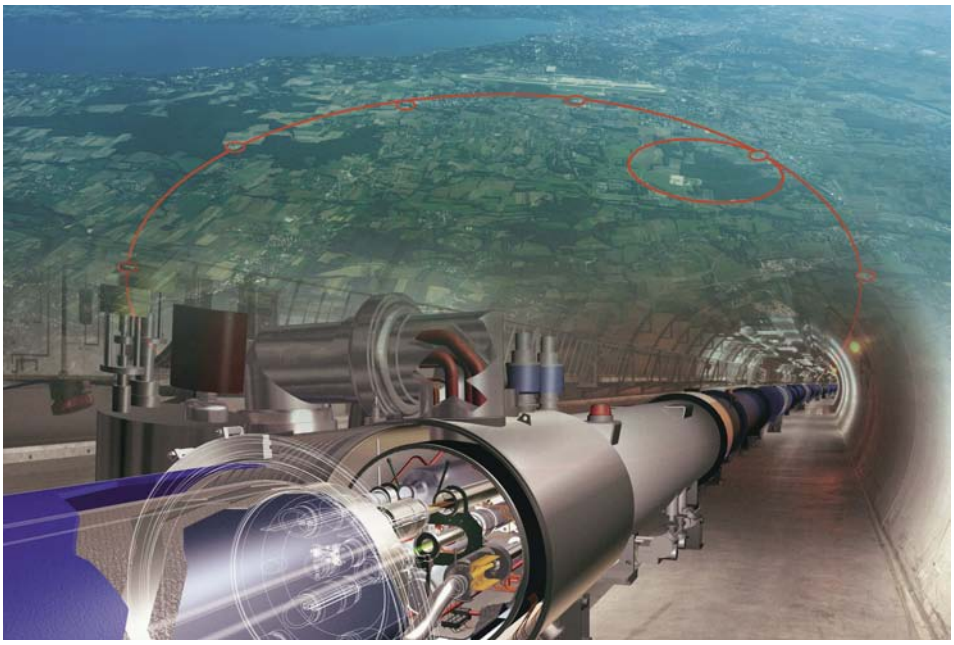

Figure 1.1: Model of the LHC tunnel and, on the map, the position of the accelerator (the tunnel is more than 100 meters below the surface).

In Fig. 1.2 an overview of CERN accelerators and detectors is shown. The particles follow different paths depending on the experiment they are allocated. For example, in case of particles for ATLAS and CMS experiments, the protons are created and accelerated in the linear accelerator, LINAC 2. They pass through

the BOOSTER, the PS and the SPS rings, where their velocity approaches more and more the light speed. Finally the protons enter the LHC, the Large Hadron Collider, where they reach their maximum energy before colliding in the detectors. The design energy is 7 TeV.

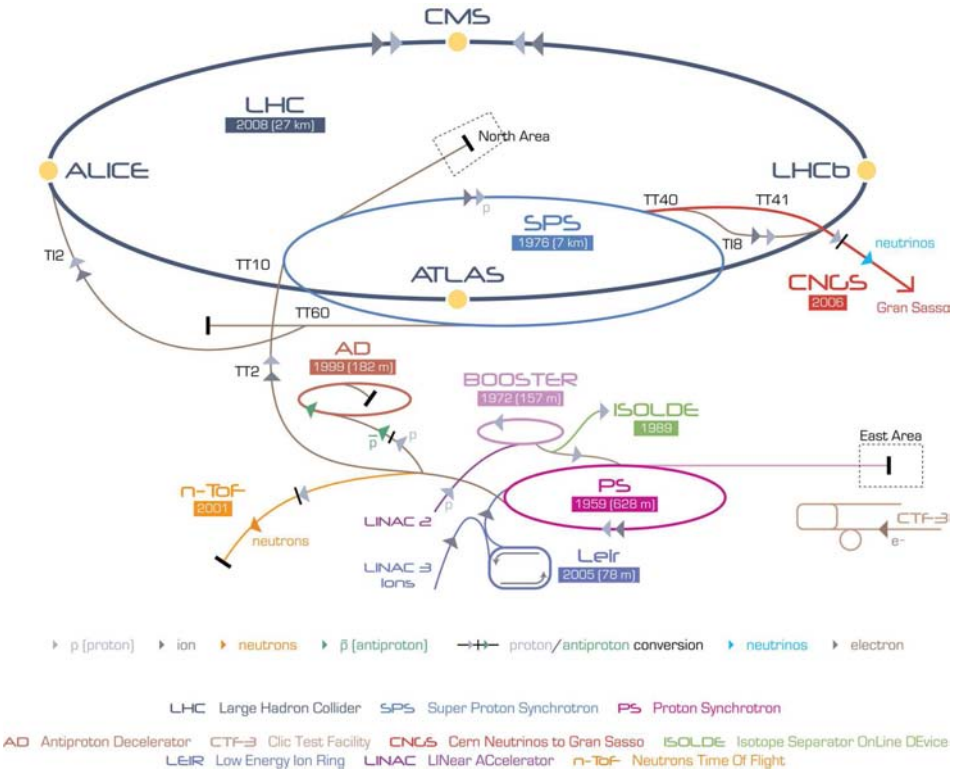

Figure 1.2: Scheme of CERN accelerators complex.

To build and test the machines and systems the physicists rely on, teams of engineers working on several sciences and techniques.
Among these engineering branches, vacuum technology plays a crucial role. To get an idea, more than 104 kilometres of vacuum chambers are kept under vacuum, at a pressure 1'000 billion times lower than atmosphere, in the LHC accelerator.

Vacuum at CERN

In particle accelerators, the main aim of vacuum is to avoid gas interaction with the circulating beam. The degrees of vacuum needed to circulate the beam, as well as the techniques to obtain it and to keep it, are different from one machine to the other.
In the SPS for example, the operating pressure (10^{-8} mbar) is reached in two steps: first an external pumping group acts until 10^{-5} mbar; then ion pumps are switched on obtaining and keeping the desired vacuum level. The entire process of pressure decrease (called pump-down) takes between 12 and 48 hours, depending on the surface area and available pumps of the vacuum sector.
Conversely, in the LHC arcs, the operating pressure must be lower than 10^{-9} mbar. This value is obtained by cryogenic pumping for the refrigerated sectors (48 km

long); in fact, as the magnet cold bores are cooled to extremely low temperatures (1.9 K), the gases condense and adhere by cryosorption. For the long straight sections (at room temperature) a procedure called bake-out, consisting in heating all components at 300°C from the outside, is implemented to achieve pressures lower than 10^{-10} mbar. That level is needed to reduce the background in the particle detector. Two families of pumps are used: Non Evaporable Getter (NEG) coating that absorbs residual molecules after activation and 780 ion pumps needed to pump the gases that NEG cannot absorb (noble gases and methane).

The reason of the long pumping time in the injectors and of bake-out use on the LHC is the presence of water vapour on the surfaces of the vacuum chambers. These molecules are adsorbed on the walls of vacuum chambers every exposure to the atmosphere. If water didn't present this behaviour, Ultra High Vacuum would be achieved much faster and in a much cheaper way. A small overview of the costs linked to water presence in CERN accelerators vacuum chambers is presented in next section.

Costs linked to water desorption for CERN accelerator complex

CERN accelerators, during their operation, undergo several unforeseen stops. From 2010 tens of interventions were needed to repair, replace or upgrade elements in the beam lines [25]. Each time, vacuum needs to be re-established before running again the machine. This long operation, delayed by water outgassing or by bake-out, implies a series of costs. These can be classified as follows:

- Non-exploitation costs. In 2012, the interventions took nearly 500 hours in total. In average, half of this time is lost in obtaining again low pressures in the line. The whole LHC accelerator complex, a 1.5 billions € machine is blocked 250 hours each year because of pump-down or bake-out.

- Intervention costs: costs linked to the equipement and man-power needed to reduce water outgassing. For example, nearly 20 sectors per year need to be baked for technical stops, representing a cost of 300'000 €/year [39].

- Design costs. In order to be able to undergo bake-outs, LHC vacuum chambers require a dedicated design. For example, the copper used for the 6 km room temperature beam lines, is doped with silver in order to obtain higher thermal conductivity, resulting 40% more expensive then usual OFHC (Oxygen free high thermal conductivity) copper [10].

From what exposed above it is evident how much the water outgassing influences LHC and injectors operations as soon as they are exposed to atmospheric pressure. For this reason, a study to understand how water molecules behave on metal vacuum surfaces was developed. A model to simulate water vapour behaviour was proposed and compared with dedicated experimental results.
In addition, by exploiting this model, a sector of SPS injector in the long straight section 1 (LSS1) was simulated. The aim was to analyse how vacuum can be improved by lump NEG pumps.

Chapter 2

Introduction to vacuum systems

Vacuum technology finds application in many fields: from food processing and wood drying to medical, aerospace and coating science. Among these applications, vacuum plays a crucial role in accelerators technology.
In this context, the main goal of vacuum is to avoid the gas-beam interaction leading to a series of unwanted phenomena as beam size increase, beam life-time reduction, etc. [30]. In addition, vacuum protects high-voltage equipment and provides thermal insulation for cryogenic systems [3].

2.1 Basic notions on vacuum technology

In the framework of vacuum technology for particle accelerators, a rarefied gas in equilibrium is always described by the ideal gas equation of state [19]:

$$pV = Nk_BT \tag{2.1}$$

or

$$p = nk_BT \tag{2.2}$$

where p, V and T are the gas pressure, volume and temperature, respectively; k_B is the Boltzmann constant ($1.38\,10^{-23} J/K$); N is the total number of molecules in the gas and n is the gas density.

The most common pressure units are mbar and Torr which are related to International System of Unit, the Pascal 1 Pa=1 N/m^2, by the following relations:

$$1\,\text{mbar} = 10^2\,\text{Pa} = 0.75\,\text{Torr}$$

$$1\,\text{Torr} = 133.32\,\text{Pa} = 1.33\,\text{mbar}$$

The number of molecules of gas can be expressed as pressure-volume ($p \times V$) values at a given temperature. Pressure-volume quantities are converted to number of molecules dividing them by k_BT as given in the equation of state. For example, 1 mbar $\cdot\,\ell$ at 293 K is

$$N = \frac{1[\text{mbar}\cdot\ell]}{1.38\,10^{-23}[\text{J/K}]\,293[\text{K}]} = \frac{0.1[\text{Pa}\cdot\text{m}^3]}{1.38\,10^{-23}[\text{J/K}]\,293[\text{K}]} = 2.47\,10^{19}\,\text{molecules}$$

In vacuum systems, pressures span several orders of magnitude. Degrees of vacuum are defined by upper and lower pressure boundaries. Different degrees of vacuum are characterized by different pumping technologies, pressure gauges, materials and surface treatments. For example, ion sources operate in the degrees of vacuum that are usually called medium and high vacuum, while in the LHC experimental beam pipes the unltra high vacuum range is attained.

Definition	**Pressure Boundaires [mbar]**
Low Vacuum LV	$10^{3} - 1$
Medium Vacuum MV	$1 - 10^{-3}$
High Vacuum HV	$10^{-3} - 10^{-9}$
Ultra High Vacuum UHV	$10^{-9} - 10^{-12}$
Extreme Vacuum XHV	$< 10^{-12}$

Table 2.1: Degrees of vacuum and their pressure boundaries from Lafferty [19].

2.2 Knudsen Number

In any physically limited vacuum system, molecules collide between each other and with the walls of the vacuum envelope. In the first case, a characteristic parameter is defined as the average length of the molecular path between two points of consecutive collisions, i.e. the mean free path $\bar{\lambda}$. It is inversely proportional to the number density $n = \frac{p}{k_B T}$ and the collision cross section σ_c [19]:

$$\bar{\lambda} = \frac{1}{\sqrt{2}\pi n \sigma_c} \tag{2.3}$$

For elastic collisions between hard spheres, Eq. 2.3 can be written in terms of the molecular diameter δ:

$$\bar{\lambda} = \frac{1}{\sqrt{2}\pi n \delta^2} = \frac{k_B T}{\sqrt{2}\pi P \sigma_c} \tag{2.4}$$

The ratio of $\bar{\lambda}$ and the characteristic dimension of a vacuum system (D), called Knudsen number is a key parameter for the gas dynamic regime definition [19]:

$$K_n = \frac{\bar{\lambda}}{D} \tag{2.5}$$

In fact, when the mean free path is very small, like at atmospheric pressure, the collisions between particles have big influence on the gas flow. When the path is in the range of the dimensions of the vacuum vessel, molecular collisions with the wall become preponderant. For even longer $\bar{\lambda}$, the gas dynamic is dominated by molecule-wall collisions: intermolecular interactions lose any effect on the gas flow. Typical beam pipe diameters are of the order of 10 cm. Therefore, free molecular regime is obtained for pressures in the low 10^{-3}mbar range or lower. Except for ion sources, vacuum systems for accelerators operate in free molecular regime. [3]

K_n range	Regime	Description
$K_n > 0.5$	Free molecular flow	Gas dynamics dominated by molecule-wall collisions
$K_n < 0.01$	Continuous (viscous) flow	Gas dynamics dominated by intermolecular collisions
$0.01 < K_n < 0.5$	Transitional flow	Transition between molecular and viscous flow

Table 2.2: Gas dynamic regimes defined by Knudsen number.

2.3 Gas kinetics

The kinetics of ideal-gas molecules are described by Maxwell-Boltzmann distribution [19]. For an isotropic gas, the model provides the distribution of the molecular speed magnitudes. The average speed of molecules $\bar{v}$ in a Maxwell-Boltzmann distribution is given by:

$$\bar{v} = \sqrt{\frac{8k_BT}{\pi m}} = \sqrt{\frac{8RT}{\pi M}} \quad \left[\frac{\mathrm{m}}{\mathrm{s}}\right] \tag{2.6}$$

where m is the mass of the molecule, M is the molar mass, R is the ideal gas constant, T the temperature and k_B in the Boltzmann constant. Tab. 2.3 shows the mean speed for common gas at room temperature.

	$\mathbf{N_2}$	$\mathbf{H_2}$	$\mathbf{H_2O}$	$\mathbf{CH_4}$
$\bar{\mathbf{v}}$	470	1761	588	622

Table 2.3: Mean speed according Maxwell Boltzmann distribution for common gases at 293 K.

Another important result of Maxwell-Boltzmann theory is the calculation of the molecular impingement rate ν on a surface, i.e. the rate at which gas molecules collide with a unit surface area exposed to the gas. Assuming that the density of molecules all over the volume is uniform, it can be shown [19] that:

$$\nu = \frac{1}{4} n\bar{v} \qquad \left[\frac{\text{molecules}}{\text{unit area} \cdot \text{unit time}}\right] \tag{2.7}$$

Usually ν is expressed in $\mathrm{mbar} \cdot \ell\,\mathrm{cm}^{-2}\mathrm{s}^{-1}$.
Numerical values as a function of pressure, at room temperature are shown in Tab. 2.4.

Gas	**Pressure [mbar]**	$\nu \left[\frac{\textbf{molecules}}{\textbf{s cm}^\mathbf{2}}\right]$
$\mathbf{N_2}$	10^{-3}	2.9×10^{17}
	10^{-8}	2.9×10^{12}
$\mathbf{H_2}$	10^{-3}	1.1×10^{18}
	10^{-8}	1.1×10^{13}
	10^{-14}	1.1×10^{7}
$\mathbf{H_2O}$	10^{-3}	3.6×10^{17}
	10^{-8}	3.6×10^{12}

Table 2.4: Impingement rate for common gases at room temperature at some selected pressures.

2.4 Conductance in free molecular flow

In free molecular regime, the net gas flow Q between two points of a vacuum system is proportional to the pressure difference $(p_1 - p_2)$ at the same points:

$$Q = C(p_1 - p_2) \tag{2.8}$$

C is called the gas conductance of the vacuum system between the two points. In free molecular regime, the conductance does not depend on pressure. It depends only on the mean molecular speed and vacuum system geometry. If the gas flow units are expressed in terms of pressure-volume (for example mbar $\cdot\, \ell$/s), the conductance is reported as volume per unit time, i.e. ℓ/s.

2.4.1 Conductance of an orifice

The conductance is easily calculated for the simplest geometry, i.e. a small orifice of surface A and infinitesimal thickness dividing two volumes of the same vacuum system (see Fig. 2.1) in isothermal condition.

The net molecular flow from one volume to the other may be calculated by the molecular impingement rate given by Eq. 2.7. The number of molecules of volume 1 that goes into volume 2 ($\varphi_{1\to2}$) is:

$$\varphi_{1\to2} = \frac{1}{4} A n_1 \bar{v}$$

while from volume 2 to volume 1 is:

$$\varphi_{2\to1} = \frac{1}{4} A n_2 \bar{v}$$

The net molecular flow is given by the difference of the two contributions:

$$\varphi_{1\to2} - \varphi_{2\to1} = \frac{1}{4} A \bar{v} (n_1 - n_2)$$

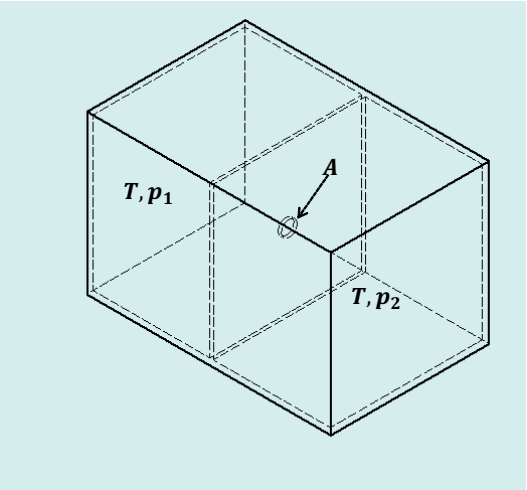

Figure 2.1: Schematic drawing of two volumes at different pressures p_1 and p_2 divided by a small orifice of surface A.

and from Eq 2.2,

$$\varphi_{1\to 2} - \varphi_{2\to 1} = \frac{1}{4}\frac{\bar{v}}{k_B T} A(p_1 - p_2) \qquad \left[\frac{\text{molecules}}{\text{unit time}}\right]$$

Expressing the flux in pressure-volume units we finally obtain:

$$Q = \frac{1}{4}\bar{v}A(p_1 - p_2) \tag{2.9}$$

Comparing Eq. 2.8 and 2.9, it is clear that the conductance of the orifice is proportional to the surface area of the orifice and the mean speed of the molecules:

$$C = \frac{1}{4}\bar{v}A \propto \sqrt{\frac{T}{m}} \tag{2.10}$$

In particular the conductance of the orifice is inversely proportional to the square root of the molecular mass:

$$\frac{C_1}{C_2} = \sqrt{\frac{m_2}{m_1}} \tag{2.11}$$

As an example, $C_{N_2} = \sqrt{2/28}\, C_{H_2} = 0.27\, C_{H_2}$. Table 2.5 collects conductance values for an orifice C', per unit surface area at room temperature for common gas species.

Gas	H_2	He	CH_4	H_2O	N_2	Ar
$C'\left[\frac{\ell}{s\,cm^2}\right]$	44	31.1	15.5	14.7	11.75	9.85

Table 2.5: Unit surface area conductances for common gas species.

2.4.2 Conductance in a complex geometry

For geometries more complex than orifices, the transmission probability τ is introduced. If two vessels, at the same temperature, are connected by a duct (see Fig. 2.2), the gas flow from V_1 to V_2 is calculated multiplying the number of molecules impinging on the entrance section of the duct by the probability $\tau_{1\to2}$ for a molecule to be transmitted into vessel 2 without coming back to vessel 1:

$$\varphi_{1\to2} = \frac{1}{4} A_1 n_1 \bar{v} \tau_{1\to2} \tag{2.12}$$

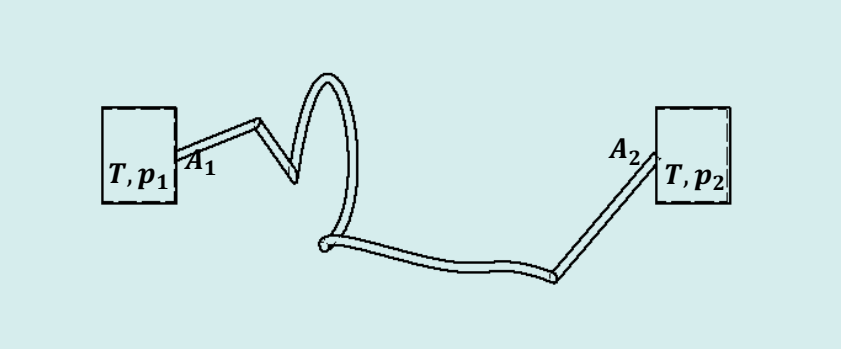

Figure 2.2: Schematic drawing of two vessels connected by a complex duct.

Similarly, the gas flow from V_2 to V_1 is written as:

$$\varphi_{2\to1} = \frac{1}{4} A_2 n_2 \bar{v} \tau_{2\to1} \tag{2.13}$$

In absence of net flow $\varphi_{2\to1} = \varphi_{1\to2}$ and $n_1 = n_2$, then:

$$A_1 \tau_{1\to2} = A_2 \tau_{2\to1} \tag{2.14}$$

When $n_1 \neq n_2$ a net flow is set up. It can be calculated taking into account Eq. 2.12, 2.13, 2.14 and 2.2:

$$Q = \frac{1}{4} A_1 \bar{v} \tau_{1\to2} (p_1 - p_2) = C' A_1 \tau_{1\to2} (p_1 - p_2) \tag{2.15}$$

where, C' is the conductance of an orifice. Finally for a complex geometry it has been found that:

$$C = C' A_1 \tau_{1\to2} \tag{2.16}$$

These results show that the conductance depends only on the speed of molecules and on the transmission probability, which depends on the geometry of the connecting duct. One of the main goals of vacuum computation is to find the value of $\tau_{1\to2}$.

2.4.3 Evaluation of the transmission probability

The transmission probability depends only on the geometry of the vacuum components. It may be calculated analytically for simple geometries by means of relatively complex integral equations (Clausing equations, see Ref. [5]).

For the very common case of tubes of uniform circular cross section of length L and radius R the Santeler equation [31] gives transmission probability with less than 0.7 % error.

$$\tau = \tau_{1\to 2} = \tau_{2\to 1} = \frac{1}{1 + \frac{3L}{8R}\left(1 + \frac{1}{1+\frac{L}{7R}}\right)} \tag{2.17}$$

For long tubes, i.e. $L/R \gg 1$, this equation can be simplified:

$$\tau \approx \frac{1}{1 + \frac{3L}{8R}} \approx \frac{8R}{3L} \tag{2.18}$$

Combining Eq. 2.18 with 2.16 gives the conductance for long circular pipes. For N_2 it can be written as:

$$C \approx 11.75 \frac{\pi D^2}{4} \frac{4D}{3L} = 12.3 \frac{D^3}{L} \quad \left[\frac{\ell}{s}\right]$$

As a result, the conductance of a tube is strongly dependent on its diameter.

Conductances of more complicated components are calculated by Test-Particle Monte Carlo methods (TPMC). The system is first modelled in three dimensions, then TPMC codes generate molecules at the entrance of the component, pointing in "random" directions according to the cosine distribution. When molecules impinge on the internal wall of the component, they are re-emitted again randomly. The program follows the molecular traces until they reach the exit of the component. The transmission probability is given by the ratio of number of "escaped" particles and "injected" molecules [6]. Many simulated molecular trajectories are needed to reduce the statistical scattering.

The reference TPMC software at CERN is Molflow+ [17]. This powerful tool imports 3D drawing of vacuum components and generates "random" molecules on any surface of interest. During this thesis it has been widely used for SPS pressure profile studies. Fig. 2.3 shows an example of a kicker magnet in the LSS1 section simulated by Molflow+.

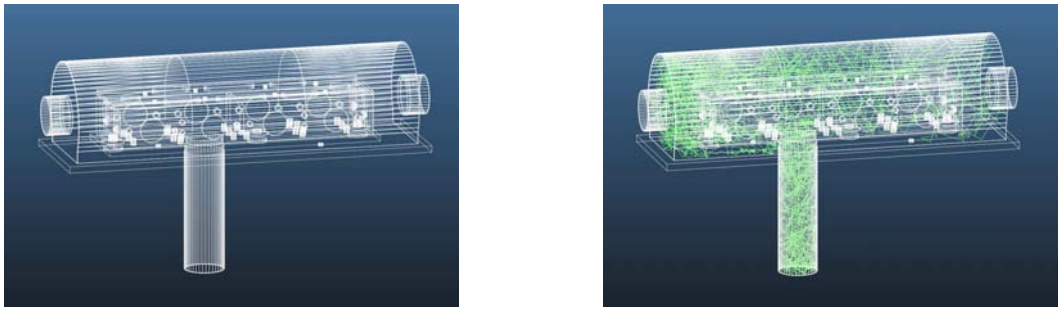

Figure 2.3: Meshes used for Monte Carlo simulation of the MKQVL kicker of SPS BA1. The second picture shows molecular tracks (in green) generated by Molflow+ code.

2.4.4 Combination of conductances

Elementary vacuum components are installed either in series, i.e. traversed by the same net gas flow, or in parallel, i.e. with equal pressures at the extremities.

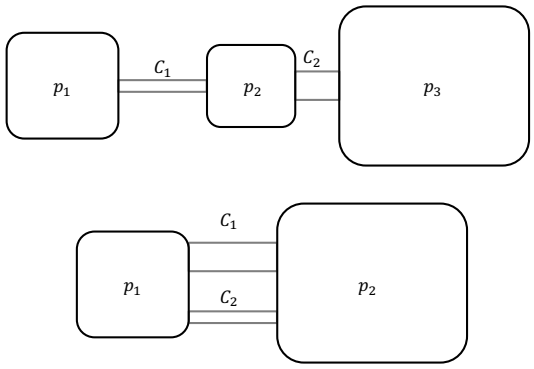

Figure 2.4: Schematic drawings of components installed in series (top) and parallel (bottom).

With reference to Fig. 2.4, the net gas flow in the two components connected in series is given by the following eqations:

$$Q = C_1(p_1 - p_2)$$

$$Q = C_2(p_2 - p_3)$$

A total conductance C_{TOT} equivalent to C_1 and C_2 is introduced in a way that:

$$Q = C_{TOT}(p_1 - p_3)$$

The resulting conductance is:

$$\frac{1}{C_{TOT}} = \frac{1}{C_1} + \frac{1}{C_2} \tag{2.19}$$

In general for N components in series:

$$\frac{1}{C_{TOT}} = \sum_{i=1}^{N} \frac{1}{C_i} \tag{2.20}$$

In the same way it can be shown that for N components installed in parallel the total conductance is the sum of the conductances of all components:

$$C_{TOT} = \sum_{i=1}^{N} C_i \tag{2.21}$$

2.5 Pumping speed

In vacuum technology, a pump is any component that removes molecules from the gas phase. A vacuum pump is characterised by its pumping speed S, which is

defined as the ratio between the pumped gas flow Q_p (pump throughput) and the pump inlet pressure p.

$$S = \frac{Q_p}{p} \quad \left[\frac{\ell}{\mathrm{s}}\right] \tag{2.22}$$

The pumping speed unit is volume over time, thus the same unit as conductance. In a more general way, S can be defined as the derivative of the pump throughput with respect to the pump inlet pressure:

$$S = \frac{\partial Q_p}{\partial p}$$

The pump throughput can be written as the gas flow φ through the cross section of the pump inlet (surface area A_p) multiplied by the capture probability σ, i.e. the probability for a molecule that enters the pump to be definitely removed and never reappear in the gas phase of the vacuum system.

$$Q_p = \varphi A_p \sigma = \frac{1}{4} A_p \, n \bar{v} \sigma$$

Considering Eq. 2.10 and 2.2, we obtain that:

$$Q_p = A_p C' n \sigma = A_p C' \sigma \frac{p}{k_B T}$$

From the definition of pumping speed and converting in pressure volume units:

$$S = A_p C' \sigma \tag{2.23}$$

Therefore, the pumping speed is equal to the conductance of the pump inlet cross section multiplied by the capture probability. The maximum theoretical pumping speed of any pump is obtained with

$$\sigma = 1$$

and it is equal to the conductance of the pump inlet cross section.

The pumping speed given by the suppliers is called nominal pumping speed; it refers to the pump inlet. The effective pumping speed S_{eff} is the one acting directly in the vacuum vessel of interest. The effective pumping speed is lower than the nominal due to gas flow restrictions interposed between the pump and the vessel.

The effective pumping speed is calculated considering the gas flow from the vessel to the pump. Taking into account Eq. 2.10 and Eq. 2.22

$$Q = C_1(p_1 - p_2) = S p_2 = S_{eff} p_1$$

$$\frac{1}{S_{eff}} = \frac{1}{S} + \frac{1}{C} \tag{2.24}$$

As a result, for $C \ll S$, $S_{eff} \approx C$. In other words, the effective pumping speed does not depend on the installed pump if the conductance of the interposed connection is very low.

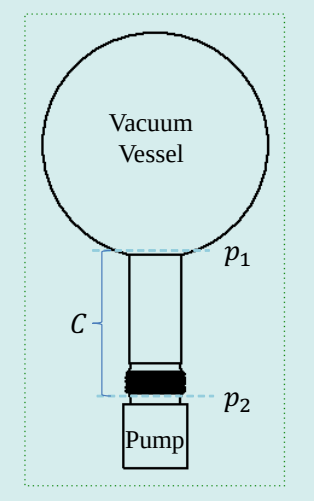

Figure 2.5: Schematic drawings of component of a gas flow restriction of conductance C interposed between a pump of pumping speed S and a vacuum vessel.

2.6 Pressure profile calculation

The calculation of the pressure profile is an essential task for vacuum system design. In general, the contributions to the total pressure of localized and distributed gas sources are considered separately and finally added. This is possible because in most of the cases the equations that describe pressure profiles are linear [3]. This may not be true if the pumping speed is pressure dependent.

Examples of pressure profiles generated by localized gas sources

The pressure in a vacuum vessel is obtained by taking into account Eq. 2.22 and the intrinsic limitation p_0 of the installed pumping system:

$$p = \frac{Q}{S} + p_0 \tag{2.25}$$

The base pressure p_0 can be expressed as the pressure attained by the system without any gas load [3].

When many vessels are interconnected, the flow balance is written (node analysis [3]). This analysis leads to a system of linear equations from which the pressure values in each vessel are calculated. As an example, with reference to Fig. 2.6, in the first vessel, the injected gas flow Q is either pumped $p_1 S_1$ or transmitted to the second vessel $C(p_1 - p_2)$. This latter flow is pumped in the second vessel or transmitted in the third vessel and so on.

$$\begin{cases} Q = p_1 S_1 + C_1(p_1 - p_2) \\ C_1(p_1 - p_2) = C_2(p_2 - p_3) + p_2 S_2 \\ C_2(p_2 - p_3) = C_3(p_3 - p_4) + p_3 S_3 \\ C_3(p_3 - p_4) = p_4 S_4 \end{cases} \tag{2.26}$$

When a second localised gas flow is settled, the node analysis is repeated. The contributions of each localised gas flow to the pressure values are then added.

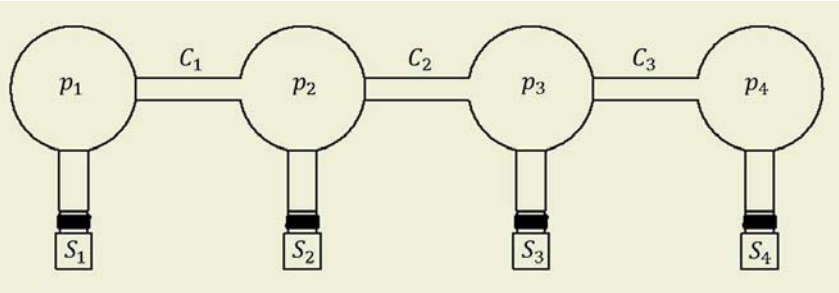

Figure 2.6: Schematic drawing of 4 interconnected vacuum vessels.

Equivalent electrical network

Looking at some of the equation studied (Eq. 2.8, Eq. 2.21, Eq. 2.20) it's possible to realise that there is an analogy between vacuum systems and electrical networks [3, 19]. For example the following equation:

$$Q = C(p_1 - p_2)$$

can be related to the electric equation

$$I = C(V_1 - V_2)$$

where I represents the electric current, C the electrical conductance and V the potential. It is possible to correlate each vacuum component and variable with electrical elements and characteristics. The ground potential is equivalent to zero

Vacuum element	**Electrical element**
Pressure p	Voltage V
Gas Flow Q	Current I
Conductance C	Conductance C or Resistance $1/C$
Volume V	Capacitance C connected to the ground
Pump	Conductance or resistance (inverse) connected to the ground
Gas source	Current generator
Constant pressure source	Voltage supply

Table 2.6: Electrical analogy for vacuum components and variables.

pressure. A vacuum chamber of a given conductance and volume corresponds to two resistances and a capacitance. For symmetry, the capacitance is placed into the middle of two resistances. If a local gas source and a pump are added, a current generator and a resistance to ground are connected to the circuit.
An example of electric analogy is shown below. The simple pumping element shown in Fig. 2.5 can be translated in the electrical network shown in Fig. 2.7.

In case of uniformly distributed outgassing and lump pumps, the pressure profiles are calculated analytically for simple geometries [3, 19].
For more complex systems numerical solutions are needed. For example, long beam

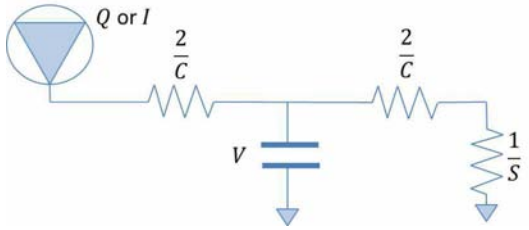

Figure 2.7: Electric network of a simple pumping unit as in Fig. 2.5.

pipes are subdivided into small units to calculate the axial pressure distribution; the small units are considered as single vacuum chambers (volume and conductance) in series. The conductance of a single small unit is equal to the conductance of the entire vacuum chamber times the number of units [3]. Distributed outgassing is taken into account by inserting a current generator on each unit.

The electrical network is solved by dedicated software, for example LTSpice [8]. The time evolution and pulsed sources are easily included in the calculation. Non-linear electric components are used to simulate pressure and time dependent conductances and pumping speeds. A clear application of this analysis method is shown in Chap. 5 with the study of the pressure profile of one SPS sector.

2.7 Pumps description

The vacuum pumps can be classified according to the physical principle they use to empty the vessels. A simplified overview on existing vacuum pumping technologies is shown on Fig. 2.8. In particular, a distinction is made between gas-

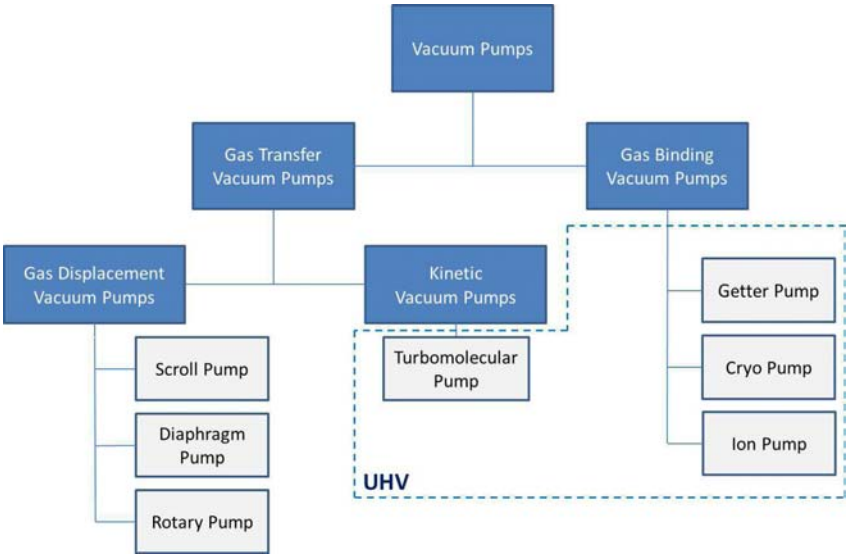

Figure 2.8: Scheme of the main types of vacuum pumps. In every family are highlighted only the ones used in this thesis.

displacement vacuum pumps and gas-binding (capture) vacuum pumps. In capture vacuum pumps the molecules remain inside the pump itself by chemical bonds (Get-

ter Pump, Ion Pump) or cryopumping. The Gas Transfer Pumps instead displace gas from the vacuum side to an exhaust side, thanks to a mechanical action on gas molecules [27].

2.8 Outgassing in vacuum systems

Several gas sources contribute to the total gas load in a vacuum system. Intentional gas injections may be the main source of gas in beam-gas interaction monitors and ion sources [3]. Air leaks due to loss of tightness of components, welds and gaskets can be eliminated by an appropriate design and choice of materials. Finally, the release of molecules from materials represents, in most of the cases, the dominant source of gas when the system is in free molecular regime. This gas release can be defined as [3]:

- Outgassing: when the gas removal is spontaneous, i.e. provoked by thermal vibration at standard temperature of the apparatus;
- Degassing: when gas molecules are freed by deliberate action, for example heating at high temperatures or bombarding the surface with particles (photons, electrons, ions);

Different phenomena can explain outgassing, like gas dissolution and diffusion (see Fig. 2.9). Outgassing properties depends on the nature of materials, and on the applied surface and thermal treatments.

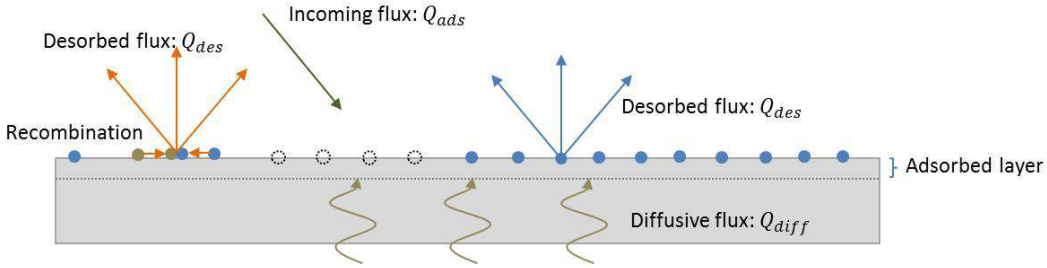

Figure 2.9: Fluxes for a general surface.

2.8.1 Water outgassing in metals

Widely recognised experimental results [7, 13, 16, 21] show that water vapour dominates the outgassing process of metals in vacuum. For smooth metals, the outgassing rate is inversely proportional to the pumping time t. The outgassing rate for stainless steel at room temperature can be empirically described by the following equation [3]:

$$Q_{H_2O} \approx \frac{3 \times 10^{-9}}{t[\mathrm{h}]} \frac{\mathrm{mbar}\ell}{\mathrm{cm}^2\mathrm{s}} \tag{2.27}$$

Such behaviour determines the pressure-time evolution of unbaked metallic vacuum systems.

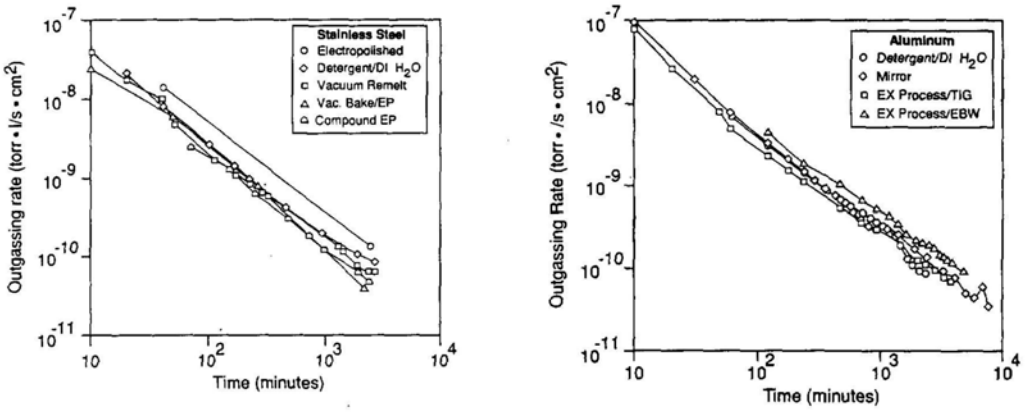

Figure 2.10: Water vapour outgassing rate of stainless steel and aluminium after four different surface treatments as measured by Dylla [7].

The average time that a molecule spends on the surface before being desorbed is defined as mean sojourn time τ. This term is dependent on the surface temperature T and on the molecule binding energy E [19]:

$$\tau = \tau_0 e^{\frac{E}{RT}} \tag{2.28}$$

with τ_0 the nominal period of vibration of an adsorbed molecule, of the order of 10^{-13} s [19] and R the gas constant.
In Tab. 2.7 are reported some values of τ as function of the binding energy at room temperature. In the case of water vapour, the sojourn time varies between some minutes to several hours (see Fig. 2.10). Thus, at room temperature, water binding energies during a pump-down varies in a window between 15 kcal/mole and 25 kcal/mole [28].

Binding energy: E [kcal/mole]	Mean sojourn time τ
10	2.6 μs
15	13 ms
20	66 s
22	33 min
23	3.1 h
24	17 h
25	92 h

Table 2.7: Mean sojourn times for different energies, $\tau_0 = 10^{-13}$ s, $T = 295$ K [28].

Water vapour outgassing rate may be reduced by acting either on molecules binding energies (changing the surface nature) or on the system temperature. The latter may be divided in two alternative solutions [3]:

1. Heating in situ during part of the pump-down time (bakeout). The bakeout is very effective for metals if it is carried out of at least 12h at temperatures

higher than 120°C. Water molecules are removed (since τ decreases at higher T) and are pumped out faster during the heating time. A much lower pressure is obtained when the system is cooled down again to room temperature, see Fig. 2.11.

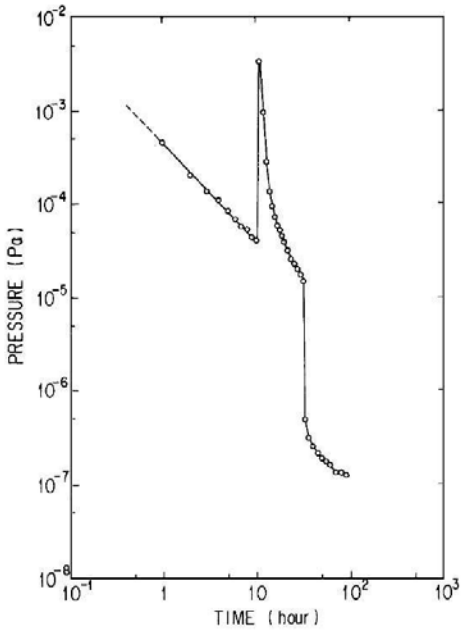

Figure 2.11: Pressure evolution in aluminium chamber [16]. The pressure increase represents the beginning of the bakeout. The pressure drop follows the system cooling down to room temperature.

2. Permanently cooling the vacuum system to cryogenic temperature during operation: water molecules have a longer sojourn time and lower pressures are quickly achieved. Note that the molecules are still on the surface, but the temperature is too low for them to be desorbed.

2.8.2 Hydrogen outgassing

When water vapour desorption is strongly reduced, the outgassing process is led by H_2. This gas is dissolved in metals as single H atoms. Its diffusion is relatively fast and, after recombination on the surface, it can be released as molecular hydrogen [3]. As for water vapour, hydrogen-outgassing rate is reduced by heating the vacuum components. Higher temperatures increase the H atoms mobility and, as a result, accelerate the depletion of the residual hydrogen content. However, there is a crucial difference between water vapour and hydrogen. Each time the vacuum system is exposed to air, water molecules re-adsorb on the surface, while hydrogen is not recharged in the bulk of the metal [3, 7].
Typical values of hydrogen outgassing are shown in Tab. 2.8. As for an activated

Material	**Bakeout T**[°C × 24h]	$\mathbf{Q_{H_2}}$ [mbarℓ/s/cm^2]
Austenitic st. steel	150	3×10^{-12}
Copper Silver added	150	3×10^{-12}
Beryllium	150	$< 10^{-14}$
Al alloys	150	$< 10^{-13}$

Table 2.8: Typical hydrogen outgassing rates after bakeout of metals used in particle accelerators [3].

process, Q_{H_2} depends exponentially on temperature [3]:

$$Q_{H_2} \propto e^{-\frac{E}{k_B T}} \tag{2.29}$$

where E is the activation energy for the diffusion process (about 0.52 eV for austenitic stainless steel, [14]).

2.8.3 Pump-down of metal vacuum chamber

The pressure over time curve for a vacuum chamber from atmospheric pressure to any degree of vacuum is called the pump-down curve [3]. During this descent, after the evacuation of atmospheric gases, the pressure level is determined by the wall outgassing (desorption of adsorbed layers or diffusing molecules) and the pumping surfaces (pumps, wall itself).
In any vacuum chamber, the mass balance equation can always be set as:

$$\frac{V}{k_B T}\frac{dp}{dt} + \frac{S}{k_B T}p + \frac{dN_a}{dt} = 0 \tag{2.30}$$

where p is pressure in the gas phase in mbar, N_a the number of adsorbed molecules. The term $\frac{V}{k_B T}\frac{dp}{dt}$ represents the change of number of molecules in the gas phase. $\frac{S}{k_B T}p$ is the flow leaving the gas phase, pumped-out by the pump.
The third term ($\frac{dN}{dt}$) represents the change of molecules adsorbed on the surfaces of the vacuum system. It can be defined as the net flow to the surface from the gas phase [28]:

$$\frac{dN_a}{dt} = Q_{ads} - Q_{des} \tag{2.31}$$

where Q_{ads} and Q_{des} represent the flow of molecules respectively adsorbed and desorbed by the surface exposed to vacuum. At the beginning of the pump-down the main contribution to the pumped flux is given by the atmospheric gases present in the volume. In this situation, the influence of the desorbed flux is negligible [19]. The mass balance becomes:

$$V\frac{dp}{dt} + Sp = 0 \tag{2.32}$$

The solution of this differential equation gives an exponential decay seen in the first part of the pump-down curve in Fig. 2.12 :

$$p = p_0 e^{-\frac{t}{\tau_p}} \tag{2.33}$$

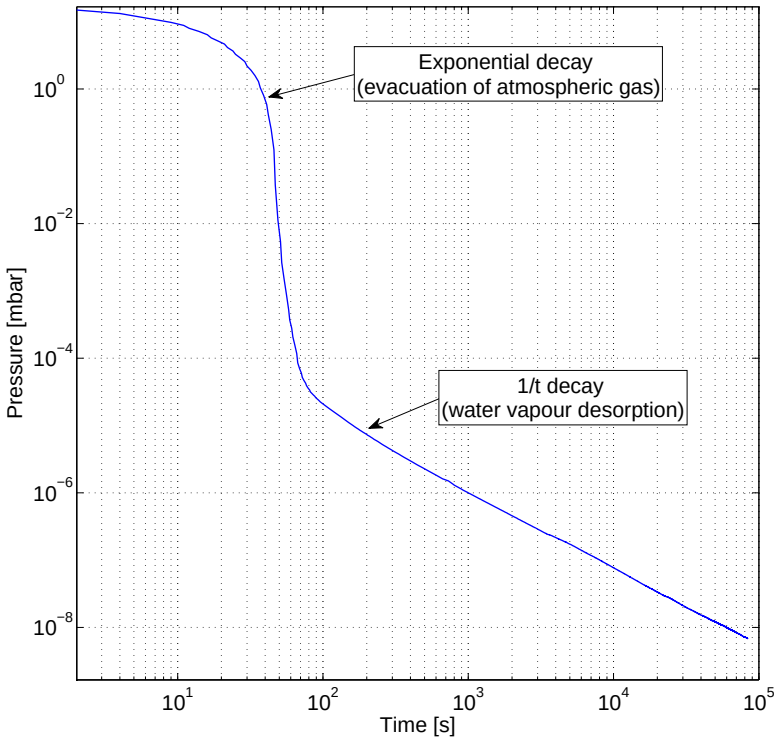

Figure 2.12: Pump down for a SS 316L chamber at 293 K.

where $\tau_p = \frac{V}{S}$ is the characteristic pumping time.

The second part of the pump-down is governed by water vapour outgassing. Fig. 2.12 shows the $1/t$ behaviour described in Eq. 2.27. Horikoshi [13] and Kanazawa [16], demonstrated that water vapour desorption can be described as a quasi-static solution of the mass balance (Eq. 2.30).
The concept of quasi-static solution lies on considering the adsorption/desorption process fully reversible, i.e. the gas and the surface phases are in equilibrium with a reaction time that is short compared to the time for an observable change in pressure. This implies that the number of adsorbed molecules adapts quickly to pressure changes [28].
This condition is verified for water desorption. In fact, at the beginning of the pump-down, when observable changes in pressure occur in seconds, molecules with $E \approx 15$ kcal/mole are desorbed (mean sojourn time is of the order of millisecond for these energies, see Tab. 2.7). At the end of the pump-down, when measurable changes in pressure occur in hours, the molecules with $E = 22 \div 23$ kcal/mole are desorbed ($\tau = 30$ min $\div$ 3 hours, see Tab. 2.7). Due to their energy during the pump-down, the sojourn time of the water molecules is lower than the time it takes for observable changes in pressure.

The comprehension of the variation of the number of adsorbed water molecules dN_a/dt is the key for the pump-down understanding and simulation. The next

chapter is focused on this term and on how it can be written in the frame of the quasi-static model.

Chapter 3

Adsorption isotherm model for water

3.1 Choice of the model: Diffusion vs Adsorption

As shown in Fig. 2.9, outgassing can be the result of different phenomena. In the literature, two main theories have been developed in order to model water desorption: one based on diffusion-limited outgassing and the other described on the basis of adsorption isotherm. Li and Dylla [21–23] assume that desorption from the adsorbed phase occurs so rapidly that the process is governed only by the rate of diffusion of molecules along pores or grain boundaries of the oxide layer [28]. Redhead [28], Kanazawa [16] and Horikoshi [13] assume that molecular diffusion is either non-existent or occurs very fast so that the outgassing is regulated only by the rate of desorption.

At the beginning of the project it has been decided to follow adsorption isotherm models, ignoring the possible diffusion of water on the surface. Adsorption studies have a generic approach: the geometric arrangement of molecules on the surface and the species distribution are not detailed. The only necessary information for such models is the order of the desorption process and the binding energy distribution of molecules on the surface. The good agreement with experimental data makes these models the most developed in the literature [4, 13, 16, 28].

3.2 Adsorption isotherm model

The adsorption isotherm model, proposed first by Horikoshi [13], and developed by Kanazawa [16] and Redhead [28] is based on the following hypothesis and definitions:

1. The surface is seen as an ensemble of N_{sites} sites. Each site is considered filled with only one molecule, without dissociation [16]. The ratio of the number of filled sites N_a to the total number of available sites N_{sites} is called surface coverage θ:

$$\theta = \frac{N_a}{N_{sites}} = \frac{n_a}{n_{sites}} \tag{3.1}$$

where n_a represents the surface density of filled sites and n_{sites} the total surface density of sites;

2. The surface has a sticking probability s (i.e. the probability that an impinging molecule is captured by a site) equal and constant for all water sites [28].

3. The quasi-static solution and the reversibility condition are fulfilled (see Sec. 2.8.3). Kanazawa [16] showed that these hypothesis are verified if:

$$\left|\frac{1}{p}\frac{dp}{dt}\right| \ll s\frac{A}{V}\frac{\bar{v}}{4} \tag{3.2}$$

where $\bar{v}$ is the average molecular velocity, A and V the surface and volume of the system. Considering a standard 1 meter long SPS chamber (diameter of 159 mm), with $A = 4.995 \times 10^3$ cm^2, $V = 19.86\ \ell$, and taking $\bar{v} = 5.94 \times 10^4$ cm/s for water at 300K:

$$\left|\frac{1}{p}\frac{dp}{dt}\right| \ll s\,3.7 \times 10^3 \quad \text{s}^{-1}.$$

When $p = 10^{-8} mbar$ (with $s = 0.1$) $dp/dt \ll 3.7 \times 10^{-6}$ mbar/s.
When $p = 10^{-4} mbar$ (with $s = 0.1$) $dp/dt \ll 3.7 \times 10^{-2}$ mbar/s.
During the pump down of a typical vacuum system the change rate of pressure is far below these limits: the quasi static solution is applicable.

The first consequence of reversible adsorption assumption is that surface coverage may be expressed as a function of pressure by a suitable adsorption isotherm [28]. This is represented in general as

$$\theta = \frac{N_a}{N_m} = \frac{n_a}{n_m} = f(p, T) \tag{3.3}$$

where m indicates monolayer coverage [1].

Substituting Eq. 3.3 in Eq. 2.30,

$$\frac{1}{p}\frac{dp}{dt} + \frac{N_m k_B T}{V}\frac{1}{p}\frac{d\theta}{dt} = -\frac{1}{\tau_p} \tag{3.4}$$

where τ_p is the characteristic pumping time.
In isothermal conditions:

$$\frac{1}{p}\frac{dp}{dt}\left(1 + \frac{N_m k_B T}{V}\frac{d\theta}{dp}\right) = -\frac{1}{\tau_p} \tag{3.5}$$

[1] The term monolayer refers to a single, closely packed layer of atoms or molecules [26]. In metal surfaces one monolayer has a density of the order of 10^{15} molecules per square centimeter of geometrical area [21]. For 1 meter-long SPS vacuum chamber

$$1\ \text{ML} \cong 4955\ \text{cm}^2 \times 10^{15}\ \frac{\text{molecules}}{\text{cm}^2} \approx 5 \times 10^{18}\ \text{molecules}$$

For variable temperature:

$$\frac{1}{p}\frac{dp}{dt}\left(1+\frac{N_m k_B T}{V}\frac{\partial\theta}{\partial p}\right)+\frac{1}{p}\frac{N_m k_B T}{V}\frac{\partial\theta}{\partial T}\frac{dT}{dt}=-\frac{1}{\tau_p} \tag{3.6}$$

then

$$\frac{dp}{dt}=-\frac{\frac{p}{\tau_p}+\frac{1}{p}\frac{N_m k_B T}{V}\frac{\partial\theta}{\partial T}\frac{dT}{dt}}{\left(1+\frac{N_m k_B T}{V}\frac{\partial\theta}{\partial p}\right)} \tag{3.7}$$

From this general form, specific solutions on pressure evolution can be found once the isotherm expression $\theta(p,T)$ and temperature evolution dT/dt are known. In the next section are detailed some relevant isotherms and the influence they have on the pump-down model.

3.3 The adsorption isotherms

The adsorption isotherms are functions that describe the equilibrium between adsorbed and gas phases at a constant temperature [15]. For the simplest case of a single adsorption energy (E) in sub-monolayer coverage, the Langmuir isotherm is obtained [16, 24].

From a generic energy distribution $\rho(E)$ of adsorption sites, supposing that every energy site has a Langmurian behaviour (θ_L), it's possible to obtain the following isotherm expression:

$$\theta(p)=\int \rho(E)\theta_L(p,E)dE \tag{3.8}$$

Fig. 3.1 shows the energy distribution as a function of the surface coverage for four isotherms: Langmuir (constant energy for every coverage), Temkin (linear dependence on coverage), Freundlich (logarithmic dependence on coverage) and Sips (similar to Freundlich with finite energy boundaries).

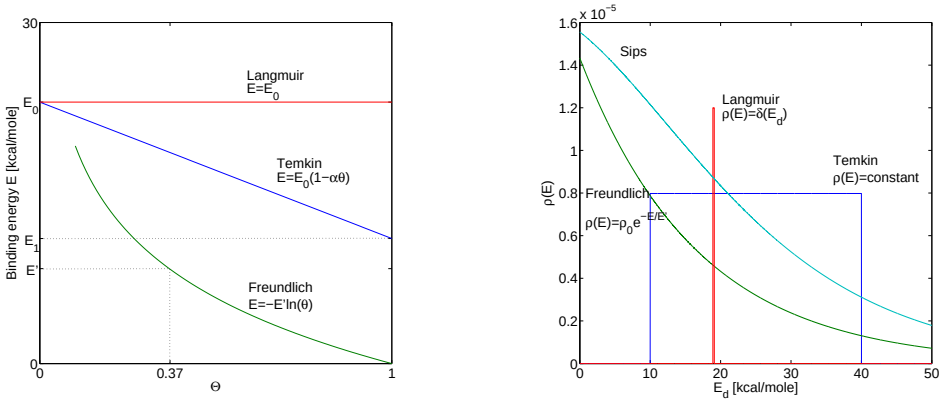

Figure 3.1: Diagrams of binding energy E vs coverage θ (left), and density of adsorption sites ρ vs binding energy, for the four considered isotherms. [28]

3.3.1 Langmuir isotherm

Langmuir isotherm [20] assumes that the rate of adsorption is proportional to the number of empty sites, and the rate of desorption is proportional to the number of filled sites. The binding energy E_d is assumed constant for any coverage. The

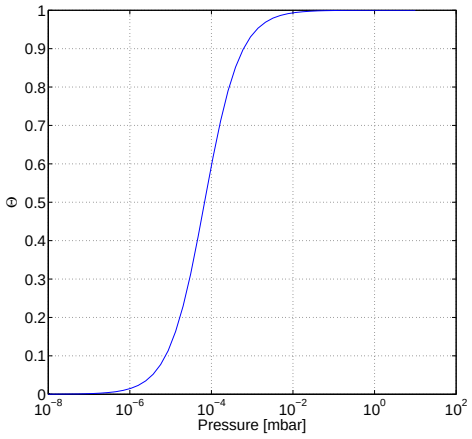

Figure 3.2: Coverage as a function of pressure for a system following Langmuir adsorption isotherm. Parameters: $E_d = 19$ kcal/mole, $n_m = 3 \times 10^{15}$ molecules/cm^2, $\tau_0 = 10^{-13}$ s, $s_0 = 1$.

mathematical expression of this isotherm can be derived from the first degree reaction equilibrium [15]. According to the hypothesis above, the desorbed flux can be expressed as:

$$Q_{des} = \frac{\theta n_m}{\tau}$$

and the adsorbed flux can be obtained from [19]:

$$Q_{ads} = (1 - \theta) s_0 p \nu$$

with s_0 the sticking probability for an empty site. Imposing the equilibrium of adsorption/desorption reaction, the two fluxes are equivalent:

$$Q_{ads} - Q_{des} = 0$$

$$\frac{\theta n_m}{\tau} - (1 - \theta) s_0 p \nu = 0 \tag{3.9}$$

This lead to the expression of Langmuir isotherm [20, 28]:

$$\theta_L = \frac{ap}{1 + ap} \tag{3.10}$$

The parameter a is expressed as:

$$a = \frac{\tau_0 s_0 \nu}{n_m} e^{\frac{E_d}{RT}} \tag{3.11}$$

Applying Eq. 3.10 in Eq. 3.5 and solving the differential equation,

$$\ln \frac{p}{p_0} + \frac{aN_m}{KV}\left[\frac{1}{1+ap_0} - \frac{1}{1+ap} + \ln\left(\frac{1+ap}{p}\frac{p_0}{a+ap_0}\right)\right] = \frac{t}{\tau_p} \tag{3.12}$$

where p_0 is the initial pressure of the pumpdown for a monolayer coverage (usually $p_0 = 3$ Torr [28]).

This equation allows to calculate the pump-down of a surface obeying Langmuir isotherm. Fig. 3.3 shows the influence of binding energy on the pump-down curve. It can be seen that the lower the energy of adsorption, the faster the decrease of

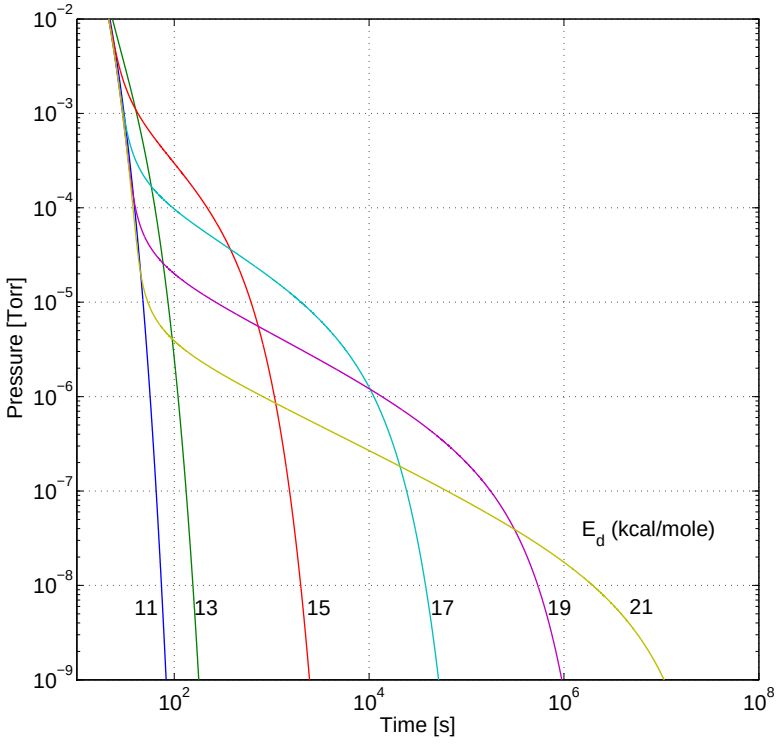

Figure 3.3: Pressure vs time for a vacuum system with a reversibly adsorbed layer obeying the Langmuir adsorption isotherm for different heats of adsorption from 11 to 21 kcal/mole. [28]. Other parameters: $n_m = 3 \times 10^{15}$ molecules/cm^2, $\tau_0 = 10^{-13}$ s, $s_0 = 1$, $A = 4740$ cm^2, $V = 16.7$ ℓ, pumping speed for nitrogen $S = 4.7$ ℓ/s and $T = 295$ K.

pressure. Note that, for high E_d, the linear portion of the curves has a slope of -0.5 in the $\log p$-$\log t$ plot. The convolution of the curves for different values of E_d approximates a straight line with slope -1 [28]. This observation is fundamental: it shows that $1/t$ behaviour (i.e. the experimental one) can be simulated by taking into account a density $\rho(E)$ encompassing more than one energy.

3.3.2 Freundlich isotherm

Freundlich isotherm [9] may be derived by taking Langmurian assumptions and using a binding energy which varies logarithmically with coverage as [28]

$$E = -E' \ln \theta \tag{3.13}$$

or [16],

$$\rho(E) = \alpha e^{-\alpha E} \tag{3.14}$$

where E' is the adsorption energy for $\theta = 0.37$ and $\alpha = 1/E'$.

Recalling Eq. 3.8

$$\theta_F(p) = \int \rho(E)\theta_L(p,E)dE$$

$$\theta_F(p) = \int \alpha e^{\alpha E} \frac{p\frac{\tau_0 s_0 \nu}{n_m} e^{\frac{E}{RT}}}{1 + p\frac{\tau_0 s_0 \nu}{n_m} e^{\frac{E}{RT}}} dE$$

After some calculations (see Ref. [16] for details) the obtained solution is:

$$\theta_F = \frac{\pi\alpha RT}{\sin \pi\alpha RT} \left(\frac{p}{p_*}\right)^{\frac{RT}{E'}} \cong \left(\frac{p}{p_*}\right)^{\frac{RT}{E'}} \tag{3.15}$$

where,

$$p_* = \frac{n_m}{\nu s_0 \tau_0} \tag{3.16}$$

In the calculation $p/p_* \ll 1$ is assumed. For typical values of $n_m = 10^{15}$molecules/cm^2, $\nu = 10^4$cm/s , $s_0 = 1$, $\tau_0 = 10^{-13}$s this gives the condition $p \ll 10^8$ mbar [16], which is always respected.

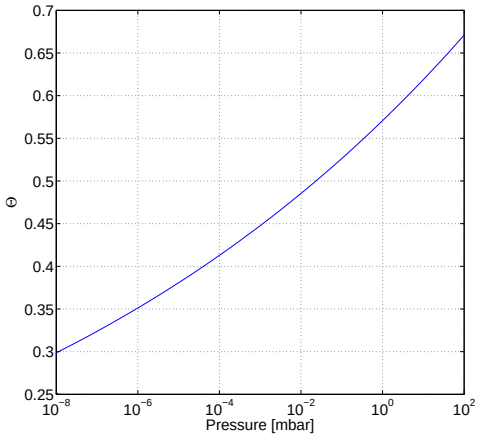

Figure 3.4: Coverage evolution as function of pressure for a surface following Freundlich adsorption isotherm. Parameters: $E' = 16.7$ kcal/mole, $n_m = 1.54 \times 10^{16}$ molecules/cm^2, $\tau_0 = 5 \times 10^{-11}$ s, $s_0 = 1$.

The function for typical parameters is shown in Fig. 3.4. It is worth noting that this isotherm is unrealistic for coverage equal 1 or 0. In fact (see Fig. 3.1) in the

Freundlich isotherm, for $\theta = 1$ the binding energy is zero and for $\theta = 0$ it goes to infinity, which is not realistic. Thus, Freundlich isotherm is useful only over a limited range of coverages.

Recalling the mass balance equation 3.6

$$\frac{1}{p}\frac{dp}{dt}\left(1 + \frac{N_m}{KV}\frac{\partial\theta}{\partial p}\right) + \frac{1}{p}\frac{N_m}{KV}\frac{\partial\theta}{\partial T}\frac{dT}{dt} = -\frac{1}{\tau_p}$$

and substituting Freundlich expression for $\theta(p, T)$, a differential equation is obtained, and its solution is showed in Fig. 3.5. The slope of pressure vs. time in the $\log p$-$\log t$ plot for an outgassing surface following Freundlich isotherm is almost -1 [28].

The most important parameters in this isotherm are E', n_m, s_0, τ_0. Their variations (except for the density of sites) have very little influence on the pump down curve. For example, Fig. 3.5 shows reference energy variation between 50 kcal/mole (very strong bonds) and 10 kcal/mole (nearly water condensation energy).

Changing the density of sites n_m have an important effect in pump down curve (see Fig. 3.6). Finally the temperature dependence of the pump down is shown in Fig. 3.7.

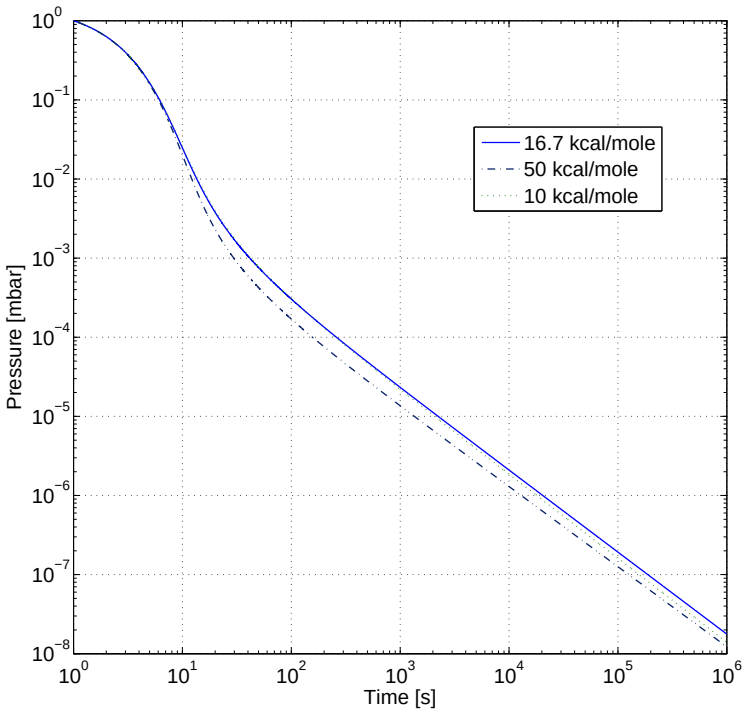

Figure 3.5: Pressure vs time with Freundlich isotherm with change of E' parameter at 293 K. Kanazawa paper [16] values are used for this graph: $n_m = 4.6 \times 10^{16}$molecules/cm^2, $\tau_0 = 5 \times 10^{-11}$s, $s_0 = 1$, $V = 5.1\ \ell$, $A = 2600$ cm^2, pumping speed for nitrogen $S = 3.3\ \ell/s$, $T = 295$ K.

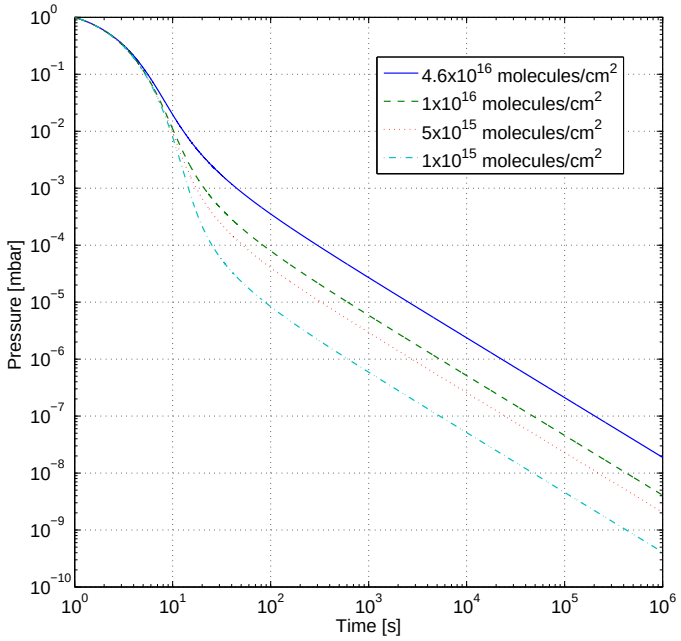

Figure 3.6: Pressure vs time with Freundlich isotherm with change of n_m parameter at 295 K. Data for the calculations are the same as for Fig. 3.5.

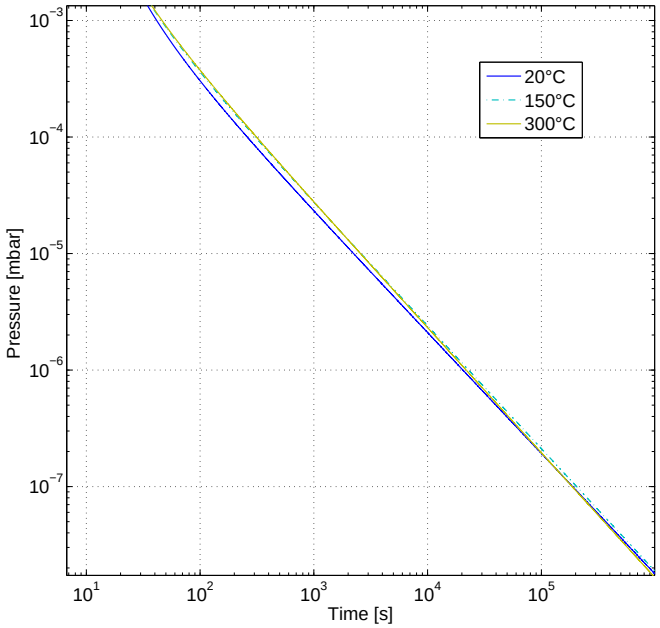

Figure 3.7: Pressure vs time with Freundlich isotherm with temperature variation. Data for the calculations are the same as for Fig. 3.5.

3.3.3 Temkin Isotherm

Temkin isotherm [35,36] can be derived from Langmuir isotherm with a heat of adsorption decreasing linearly with increasing coverage [28], i.e.

$$E_d = E_0(1 - \alpha\theta). \tag{3.17}$$

or,

$$\rho(E) = \begin{cases} \frac{1}{E_0 - E_1} & \text{if } E_1 < E < E_0 \\ 0 & \text{if } E < E_1 \text{ and } E > E_0 \end{cases} \tag{3.18}$$

The isotherm may be derived, for a non-uniform surface, by dividing it into a number of uniform elements di, on each of which the heat of adsorption is constant, each element is assumed to obey a Langmuir isotherm [28]. The value of θ can be found from 3.8:

$$\theta_T(p) = \int_{E_1}^{E_0} \frac{1}{E_0 - E_1} \frac{p\frac{\tau_0 s_0 \nu}{n_m} e^{\frac{E}{RT}}}{1 + p\frac{\tau_0 s_0 \nu}{n_m} e^{\frac{E}{RT}}} \, dE$$

$$\theta_T = \frac{RT}{E_0 - E_1} \left[\ln\left(1 + p\frac{\tau_0 s_0 \nu}{n_m} e^{\frac{E}{RT}}\right) \right]_{E_1}^{E_0}$$

finally,

$$\theta_T = \frac{RT}{E_0 - E_1} \ln\left(\frac{1 + \frac{p}{p_*} e^{\frac{E_0}{RT}}}{1 + \frac{p}{p_*} e^{\frac{E_1}{RT}}}\right) \tag{3.19}$$

where $p_* = n_m/\nu s_0 \tau_0$, E_1 is the heat fo adsorption at $\theta = 1$, E_0 is the heat of adsorption at $\theta = 0$.

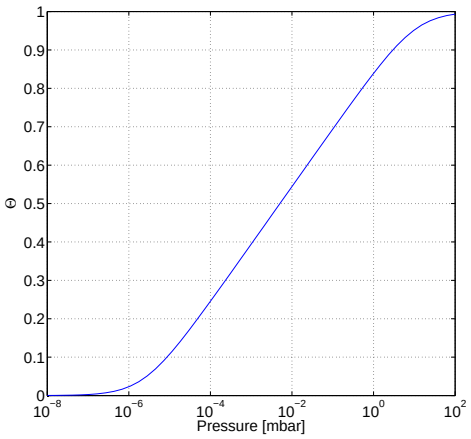

Figure 3.8: Coverage evolution as function of pressure for a surface following Temkin adsorption isotherm. Parameters: $E_0 = 23$ kcal/mole, $E_1 = 12$ kcal/mole, $n_m = 2.9 \times 10^{15}$ molecules/cm^2, $\tau_0 = 10^{-13}$ s, $s_0 = 1$.

Temkin isotherm gives a 1/t behavior once inserted in equation 3.7. Main parameters for this isotherm are the energy boundaries E_0, E_1 and the density of sites n_m (s_0 and τ_0 variations have no effect). Unlike Freundlich isotherm, energy

boundaries change can give big variations on the pump down curve when Temkin isotherm is used.

Fig. 3.9 shows the effect of the E_0 variation. With increasing E_0, the pump down becomes less steep. This trend is due to additional sites with higher binding energy and so with longer mean sojourn time.

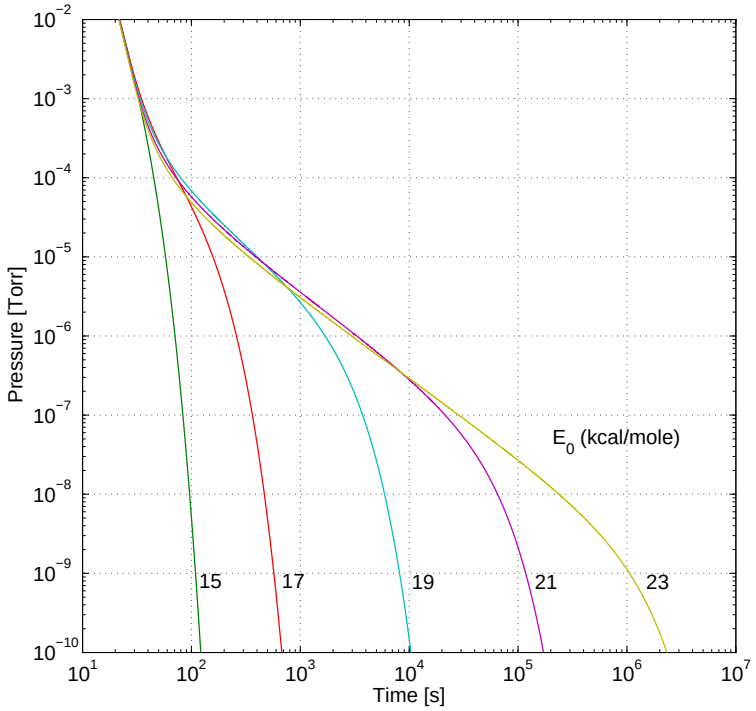

Figure 3.9: Variation of pump-down curve following the change of E_0 energy. Data for calculations are the same as Redhead [28]: $n_m = 2 \times 10^{16}$ molecules/cm^2, $E_1 = 10.6$ kcal/mole, $\tau_0 = 10^{-13}$ s,$s_0 = 1$, $A = 4740$ cm^2, $V = 16.7\ \ell$, $S = 4.7\ \ell/s$.

With the variation of E_1 a different effect is obtained (see Fig. 3.10). The major change is seen on the first part of the pump-down, while in the end all curves tend to the same slope. The term E_1 set the lowest energy of adsorption. If it increases, so does the minimum mean sojourn time.

Finally, the variation of the density of sites is analyzed (Fig. 3.11). The effect of an increase of n_m is a translation of the pump-down curve toward higher pressures.

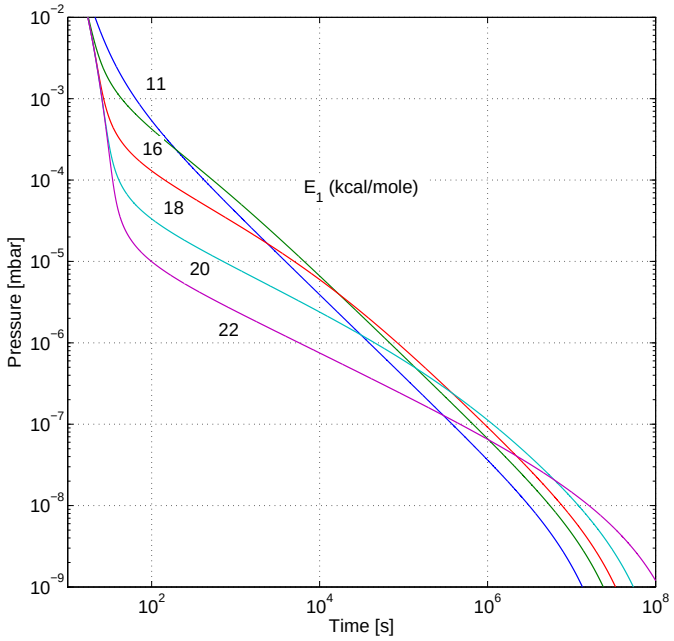

Figure 3.10: Variation of the slope of pump-down curve following the change of E_1 energy. Data for the calculations are the same as for Fig. 3.9 with $E_0 = 23$ kcal/mole.

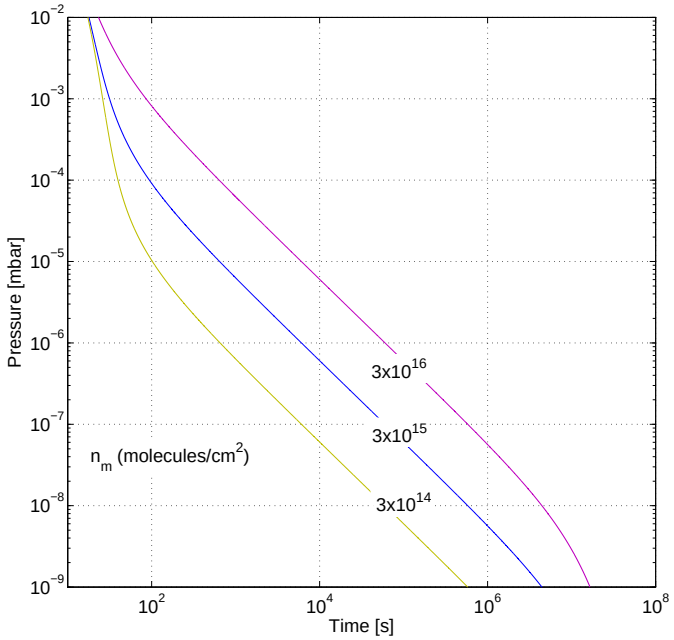

Figure 3.11: Variation of pump-down curve following the change of n_m density of sites. Data for the calculations are the same as for Fig. 3.9 with $E_0 = 23$ kcal/mole and $E_1 = 10.6$ kcal/mole.

3.3.4 Sips isotherm

Sips isotherm is an evolution of Freundlich isotherm. The main limit of Freundlich isotherm is that the area below its energy distribution is infinite [32].
Sips [32, 33] combined Langmuir isotherm with Freundlich isotherm, obtaining the following expression:

$$\theta_S(p) = \frac{K_s p^\alpha}{1 + K_s p^\alpha} \tag{3.20}$$

where

$$K_s = \left(\frac{s_0 \tau_0 \nu}{n_m}\right)^{\frac{RT}{E'}} = \left(\frac{1}{p_*}\right)^{\frac{RT}{E'}} \text{ and } \alpha = \frac{RT}{E'} \tag{3.21}$$

The energetic distribution as proposed by Kumar et al. [18] for this isotherm is:

$$\rho(E) = \frac{\left(\frac{p_S}{p_*}\right)^{\frac{RT}{E'}} e^{-\frac{E}{E'}}}{\left(\left(\frac{p_S}{p_*}\right)^{\frac{RT}{E'}} e^{-\frac{E}{E'}} + 1\right)^2 E'} \tag{3.22}$$

where p_S is the vapour pressure of water at temperature T, E' the reference energy, $p_* = s_0 \tau_0 \nu / n_m$.

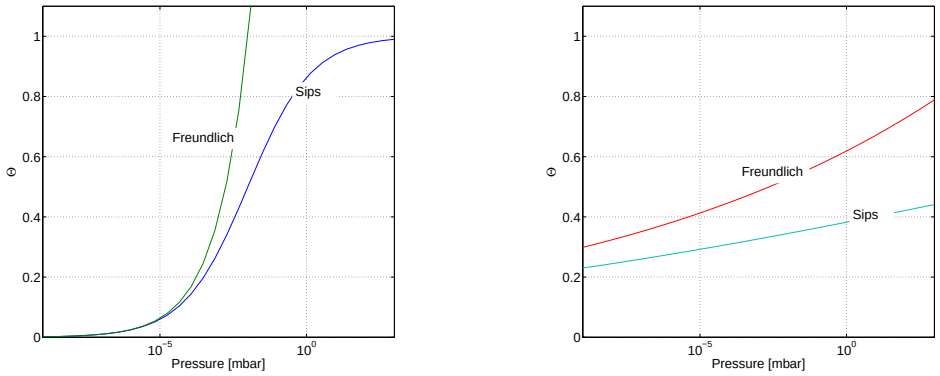

Figure 3.12: Coverage evolution as function of pressure: Sips and Freundlich comparison with $K_s = 1$ and $\alpha = 0.4$ (left), and $K_s = 0.5263$ and $\alpha = 0.0352$ (right, values compatible with water pump-down).

As for Freundlich isotherm, the main parameters are E' and n_m. The variation of the parameters of Freundlich and Sips isotherms, applied to a vacuum system, have the same effect on its pump-down curve, as the two isotherms behaviour tends to coincide for very low pressures (see Fig. 3.13 and Fig. 3.14).

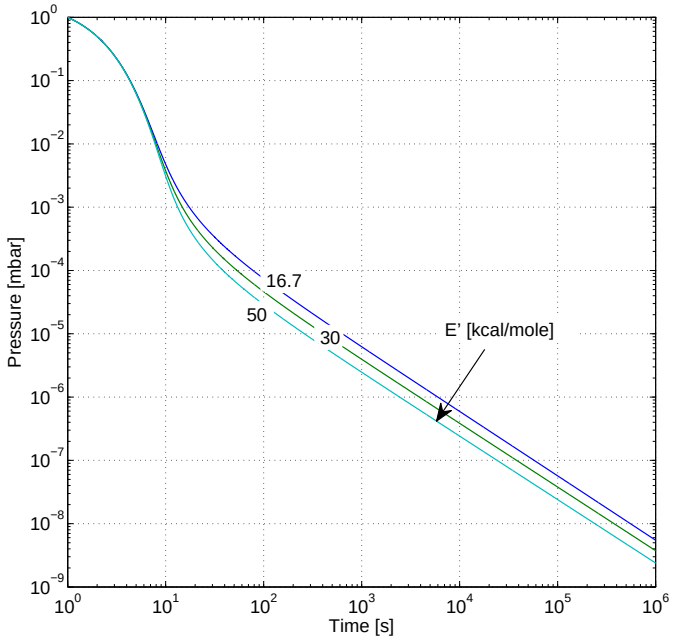

Figure 3.13: Variation of pump-down following the change of E' energy. Data for calculations are the same as for Fig. 3.5.

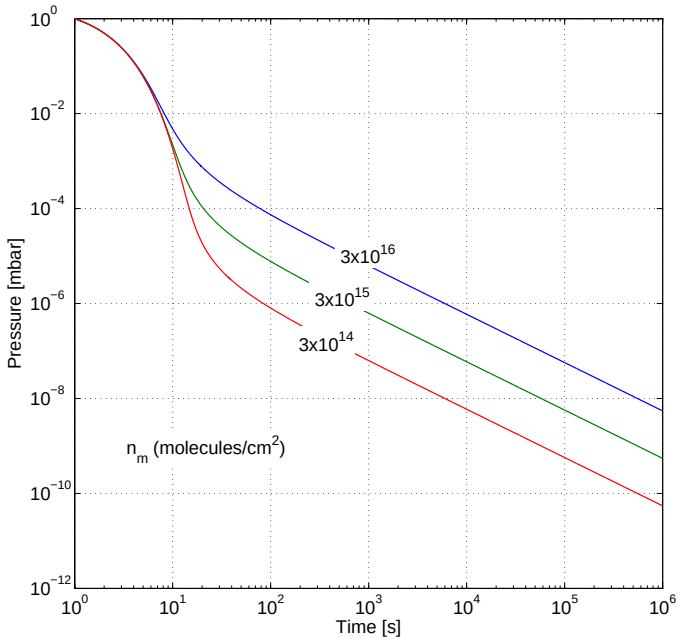

Figure 3.14: Variation of pump-down following the change of n_m density of sites. Data for calculations are the same as for Fig. 3.5.

Chapter 4

Measurements and results

The experimental activity was developed in order to reach the following goals:

1. Demonstrate the validity of isotherm model for water desorption on untreated metal chambers;
2. Explore the pump-down of metal vacuum chambers that underwent various treatments: air-bake, vacuum firing and electropolishing, palladium/silver coating.

4.1 Experiments on small untreated chamber

Different experiments were performed in order to understand if the isotherm model predicts the pump-down curves of the unbaked vacuum chamber.

4.1.1 Pump-down at room temperature

This experiment consists in the pump-down of as cleaned stainless steel vacuum vessel. The experimental set-up, installed in the laboratory with controlled temperature of $20 \pm 2°C$, is shown in Fig. 4.1.

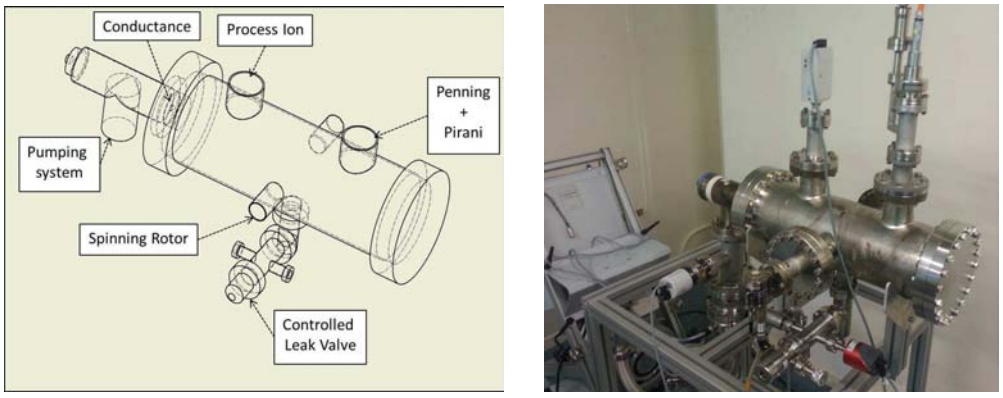

Figure 4.1: Vessel 1: in the scheme are highlighted the installed pressure gauges.

The chamber (V1) is made of stainless steel 304L, with volume $V_1 = 11.3\ \ell$ and surface $A_1 = 3946\ \text{cm}^2$. After cleaning (see App. B.1), four pressure gauges were

installed on it: a Penning gauge, a Pirani gauge, a Process Ion gauge and a Spinning Rotor Gauge. For details see App. A.
The system was connected to the pumping group through an all metal right-angle valve. An orifice[1] was installed between that valve and the chamber, resulting in an effective pumping speed for water at 20°C of 16.7 ℓ/s. A controlled leak valve allowed to vent the system to air.

The pump-down curve at 20°C, as recorded by the Penning and Pirani gauges, is shown in Fig. 4.2. Since our interest is focused on water vapour desorption, only the range of pressure of Penning gauge will be considered, the rest being the residual atmospheric gas. In addition, all pump-down curves will be expressed in terms of outgassing rate, i.e. mbar $\cdot\, \ell$/s/cm^2. The conversion from the pressure signal is obtained through Eq. 4.1:

$$Q = p\frac{S}{A} \qquad \left[\frac{\text{mbar} \cdot \ell}{\text{s cm}^2}\right] \tag{4.1}$$

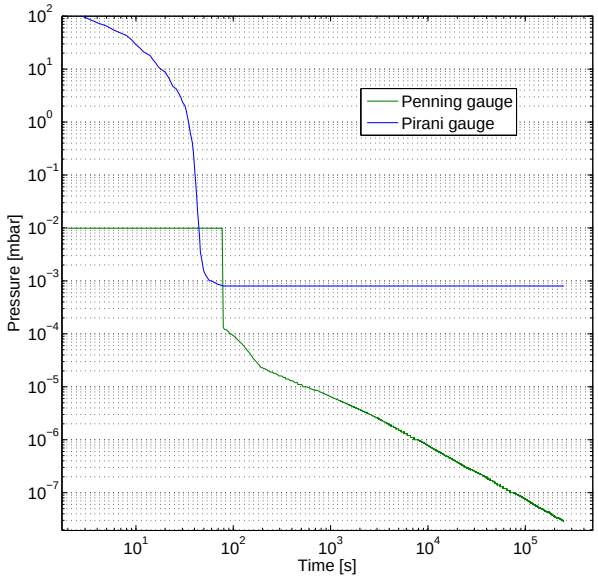

Figure 4.2: Experimental data for the pump-down of V1 at 20°C.

The isotherm model, as described by Eq. 3.7 has been implemented in Matlab for different isotherms.

$$\frac{dp}{dt} = -\frac{\frac{p}{\tau_p} + \frac{1}{p}\frac{N_m k_B T}{V}\frac{\partial\theta}{\partial T}\frac{dT}{dt}}{\left(1 + \frac{N_m k_B T}{V}\frac{\partial\theta}{\partial p}\right)} \tag{3.7}$$

[1]The orifice is made of a copper disc with a central circular hole of 1.2 cm diameter. The pumping speed for water at 20°C is

$$S = C' A_c = 14.7 \times \frac{\pi 1.2^2}{4} = 16.65 \qquad \frac{\ell}{\text{s}}$$

with C' value taken from Tab. 2.5.

Tab. 4.1 resumes the equations and parameters for the three selected isotherms.

Isotherm	**Equation** $\theta(p,T)$]	**Parameters**
Freundlich	$\theta_F = \left(\frac{p}{p_*}\right)^{\frac{RT}{E'}}$ $p_* = n_m/\nu s_0 \tau_0$	$\mathbf{n_m}$, $\mathbf{E'}$, s_0, τ_0
Temkin	$\theta_T = \frac{RT}{E_0 - E_1} \ln\left(\frac{1+\frac{p}{p_*}e^{\frac{E_0}{RT}}}{1+\frac{p}{p_*}e^{\frac{E_1}{RT}}}\right)$ $p_* = n_m/\nu s_0 \tau_0$	$\mathbf{n_m}$, $\mathbf{E_1}$, $\mathbf{E_0}$, s_0, τ_0
Sips	$\theta_S = \frac{K_s p^\alpha}{1+K_s p^\alpha}$ $K_s = \left(\frac{s_0\tau_0\nu}{n_m}\right)^{\frac{RT}{E'}}$ and $\alpha = \frac{RT}{E'}$	$\mathbf{n_m}$, $\mathbf{E'}$, s_0, τ_0

Table 4.1: Equations and parameters of the considered isotherms (in bold are the most important, i.e. the ones used as degrees of freedom in the optimization problem).

After imposing the boundary conditions (pumping speed, volume, surface, temperature, etc.), the fitting was obtained by least square optimisation on isotherm's parameters (see Fig. 4.3 for Temkin).

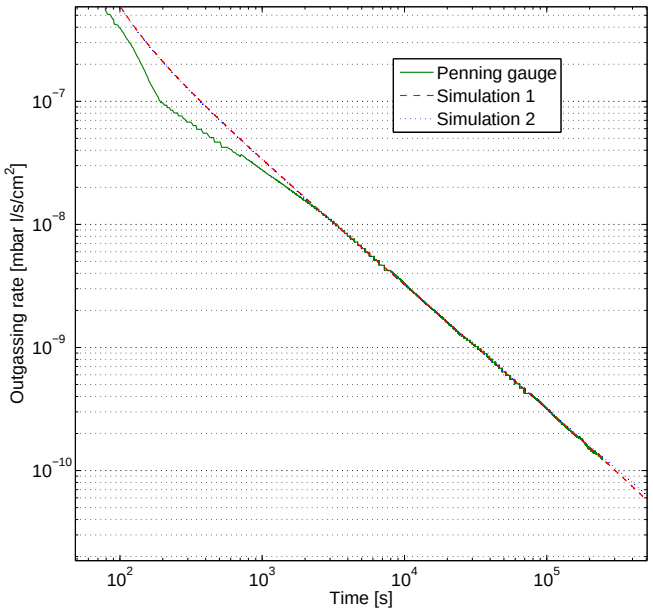

Figure 4.3: Pump-down of V1 at 20°C with optimized Temkin isotherm simulation. Simulation 1 is obtained for $n_m = 1.7 \times 10^{16}$ molecules/cm^2, $E_1 = 10.6$ kcal/mole, $E_0 = 23$ kcal/mole (values similar to Redhead paper [28]). Simulation 2 is obtained for $n_m = 3.3 \times 10^{16}$ molecules/cm^2, $E_1 = 10.6$ kcal/mole, $E_0 = 35$ kcal/mole.

The fitting code couldn't find a unique solution since the simulation presented too many degrees of freedom with respect to the data acquired. For example, the same fitting for the Temkin isotherm is obtained if the number of sites n_m or the energy boundaries (E_0 and E_1) are changed accordingly(see Fig. 4.3). To reduce this limitation, it was decided to conduct a set of measurements at different temperatures to obtain a unique set of parameters for best fitting.

4.1.2 Bake-out

As explained in Sec. 2.8.1, the bake-out consists in heating the vacuum chamber for a certain time in order to degas the adsorbed molecules. Heating at 120°C is considered enough to remove the molecules from the walls, so when the system is cooled down at room temperature, the chamber pressure is no more limited by water desorption.
An example of bake-out at 140°C for 24 hours is shown in Fig. 4.4.

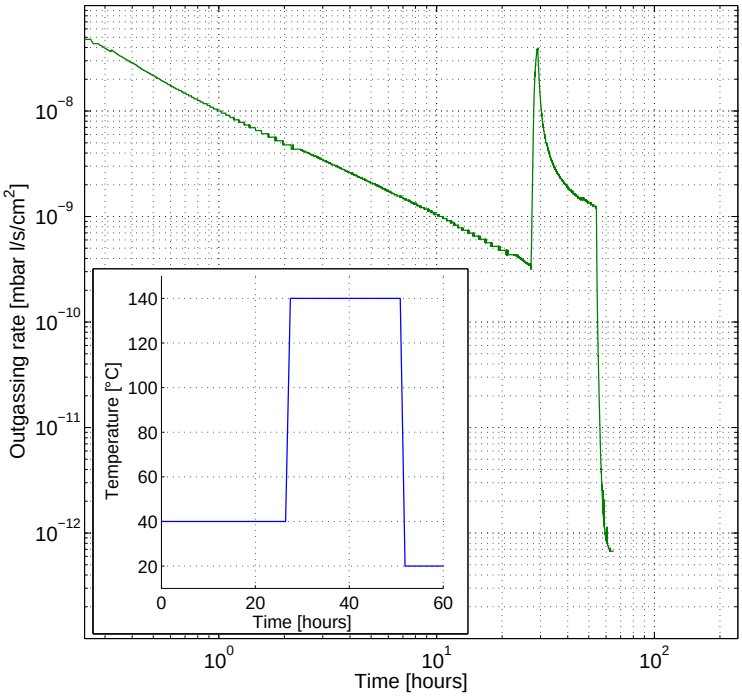

Figure 4.4: Bake-out at 140°C in V1 chamber. In the box is shown the temperature variation with time.

In order to fully calculate a pump-down curve that includes a bake-out cycle, hydrogen outgassing has been added to the model. It is presumed that H_2 outgassing assumes Arrhenius behaviour at constant hydrogen concentration. The hydrogen flux leaving the surface at 20°C ($Q_{H_2,20^\circ}$) is set as an additional parameter, while the outgassing dependence on temperature is obtained from Eq. 2.29

$$Q_{H_2}(T) = Ae^{-\frac{E}{k_B T}} \tag{2.29}$$

where

$$A = \frac{Q_{H_2,20^\circ}}{e^{-\frac{E}{k_B 293}}}$$

and $E = 0.52\text{eV}$, $k_B = 8.617 \times 10^{-5}\text{eV/K}$ [14].
$Q_{H_2,20^\circ}$ is obtained from outgassing measurements after bake-out. In fact, since water has been removed by heating, the outgassing rate is considered to be determined only by hydrogen.

Kanazawa [16] showed that the pressure curve during a bake-out in aluminium chambers can be simulated with Freundlich isotherm using 4 parameters ($E' = 16.7$ kcal/mole, $n_m = 4.6 \times 10^{16}$ molecules/cm^2, $s = 1$ and $\tau_0 = 5 \times 10^{-11}$ s, see Fig. 2.11). For 304L stainless steel chamber, a good fitting with Freundlich isotherm was obtained with data shown in Tab. 4.2.

$\mathbf{n_m}$	$\mathbf{E'}$	τ_0	$\mathbf{s_0}$	$\mathbf{Q_{H_2,20^\circ}}$
$5.6 \times 10^{16}\ \frac{\text{molecules}}{\text{cm}^2}$	$16.7\ \frac{\text{kcal}}{\text{mole}}$	5×10^{-11} s	1	$5 \times 10^{-12}\ \frac{\text{mbar}\ell}{\text{cm}^2\text{s}}$

Table 4.2: Values for Freundlich isotherm and hydrogen model fitting V1 bake-out between 40°C and 140°C.

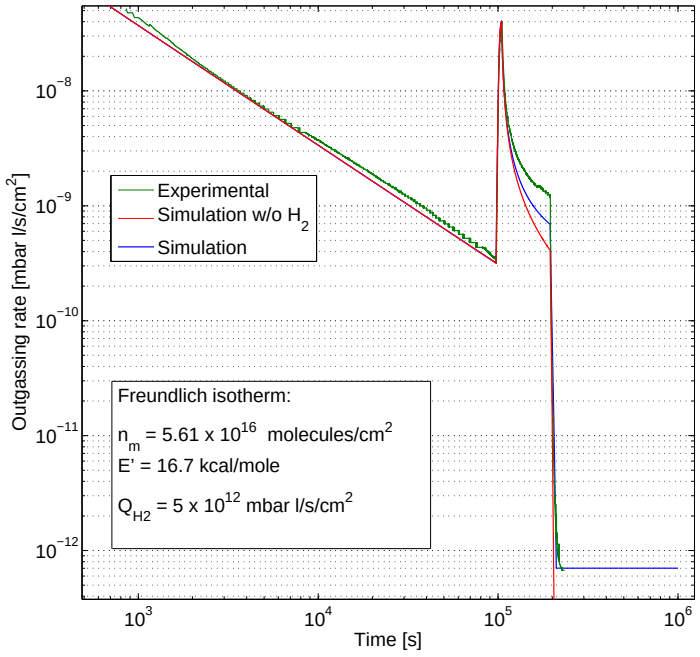

Figure 4.5: Freundlich fitting of a bake-out outgassing rate curve (bake-out temperature: 140°C).

Freundlich model seems to simulate well the experimental data, except for the final

part of the baking at 140°C. Even adding hydrogen outgassing, the model cannot describe that experimental behaviour (see Fig. 4.5).

Using Temkin isotherm, similar results are obtained (see Fig. 4.6) with the parameters shown in Tab. 4.3. These are consistent with one of the solutions for a pump-down at 20°C (see Fig. 4.3).

$\mathbf{n_m}$	$\mathbf{E_1}$	$\mathbf{E_0}$	τ_0	$\mathbf{s_0}$	$\mathbf{Q_{H_2,20^\circ}}$
3.3×10^{16} $\frac{\text{molecules}}{\text{cm}^2}$	10.6 $\frac{\text{kcal}}{\text{mole}}$	35 $\frac{\text{kcal}}{\text{mole}}$	10^{-13} s	1	5×10^{-12} $\frac{\text{mbar}\ell}{\text{cm}^2\text{s}}$

Table 4.3: Values for Temkin isotherm with hydrogen outgassing best fitting the bake-out curve of V1.

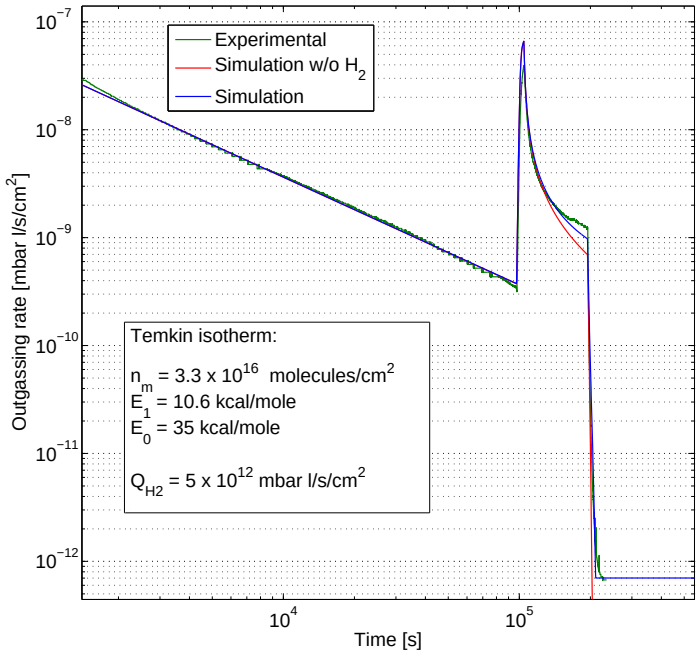

Figure 4.6: Temkin fitting of an outgassing rate curve during a bake-out at 140°C in V1 chamber.

4.2 Effect of temperature on the pump-down of untreated vacuum chambers

The pump-down curves have been measured at different temperatures after a modification of the experimental set-up. After cleaning (see App. B.1), a 3 meter-long 316L stainless steel chamber has been installed on Vessel 1 (Fig. 4.7 and Fig. 4.8). This vessel (V2) has a diameter of 100 mm, surface area 9425 cm^2 and volume 23 ℓ. A Penning gauge is installed at the extremity of vessel 2. The effective pumping speed is equal to that of previous experiments. The total surface and volume were $A_{1+2} = 13371$ cm^2 and $V_{1+2} = 35$ ℓ.

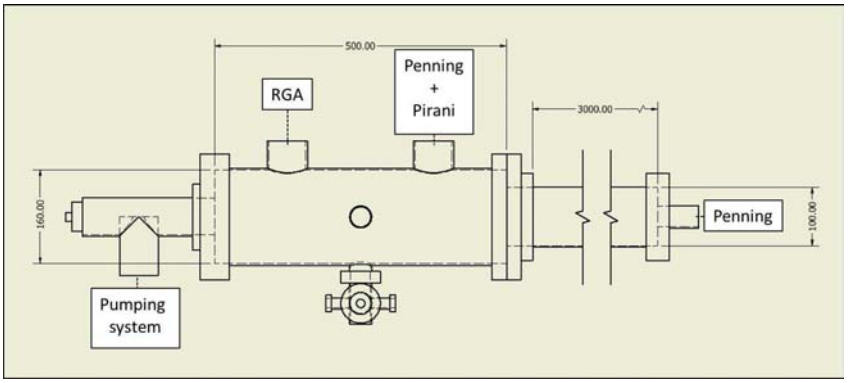

Figure 4.7: Drawing of the modified experimental set-up: a 3m chamber and a Penning gauge have been added.

Figure 4.8: Picture of updated experimental set-up.

4.2.1 Experimental details

Two types of measurements were performed: a pump-down at constant temperature (A) and a bake-out between 50°C and 150°C (B).
The following steps have been performed for each type A measurement:

1. system venting at 20 ± 2 °C with atmospheric air for 30 min;
2. pump-down until $p_0 \approx 10^{-1}$ mbar and pumping system valve closure;
3. heat-up until the desired temperature (50°C, 100°C, 120°C, 150°C) in static conditions;
4. start the pump-down during a period between 24 and 48 hours;
5. bake the system at 120°C for 12 hours;
6. cool down to 20 ± 2 °C and restart the process.

When the pump-down was performed at 150°C the 120°C bake-out was suppressed, so the chamber was cooled directly to 20°C. At each temperature, the process was repeated several time to check the repeatability of the measurement.
The procedure of the measurement B is showed below:

1. system venting at 20 ± 2 °C with atmospheric air for 30 min;
2. pump-down until $p_0 \approx 10^{-1}$ mbar and pumping system valve closure;
3. heat-up until 50°C in static conditions;
4. start the pump-down; after 1 hour of pumping, start heating to 150°C;
5. pump-down for 24 hours at the latter temperature
6. the system is cooled down again at 50°C.

The humidity of the venting air was not controlled in the laboratory, varying between 27 % and 60 %. At these values (see Dylla [21]) a stainless steel surface adsorbs more than one monolayer of water molecules. Redhead [29] demonstrated that a pump-down is not influenced (except for the first few seconds) by the number of adsorbed layers. This means that, since the surface was covered by more than one monolayer for each exposure, no effect of the uncontrolled humidity is seen, apart from the beginning of the pump-down.

4.2.2 Results

In Fig. 4.9 the results of measurement A are shown. All pump-down curves follow $1/t$ behaviour at all temperatures. At high temperature a change in the slope can be seen, leading the outgassing rate to a stabilization, maybe due to hydrogen outgassing. In Fig. 4.10 the outgassing rate during bake-out is shown in comparison with the pump-down curves performed at constant temperature at 50°C and 150°C.

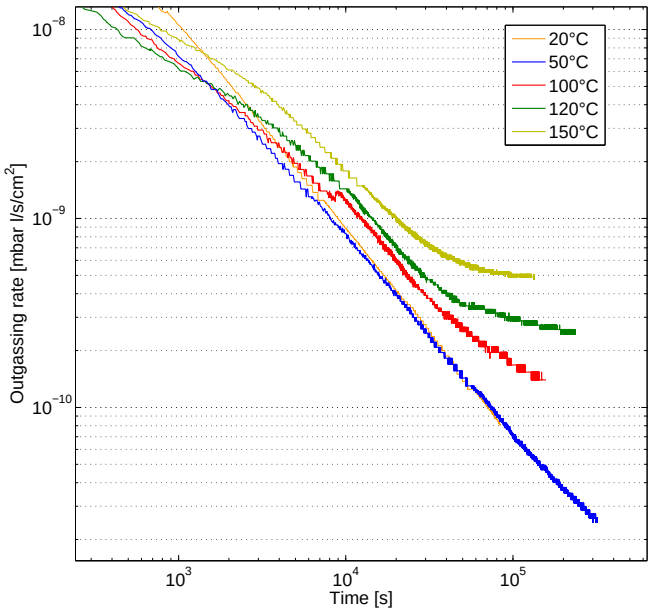

Figure 4.9: Pump-down curves for the untreated chamber at four different temperatures.

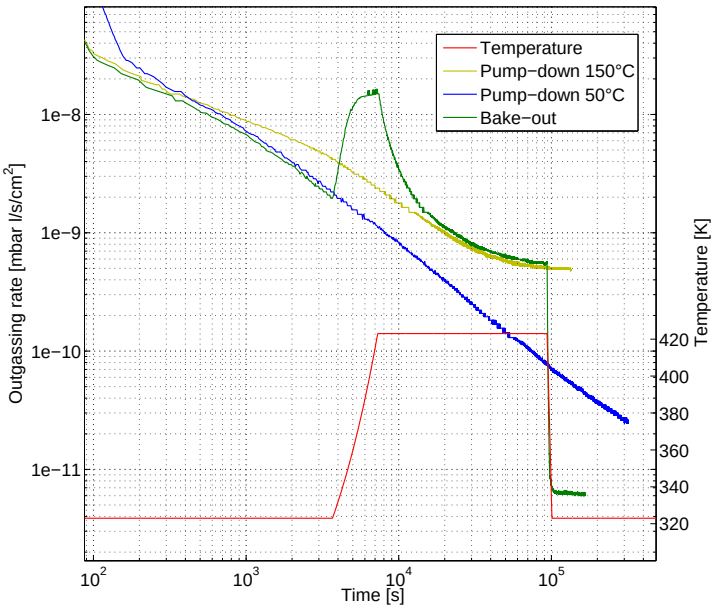

Figure 4.10: Pump-down curve during bake-out at 50°C and 150°C for the untreated chamber. The isothermal pump-down curves at 50°C and 150°C are reported as in Fig. 4.9

4.2.3 Results vs. Isotherm model

The isotherm model, was used to fit the experimental curves. The analysis has been conducted for three isotherms: Temkin, Freundlich and Sips.
The fitting code has been created in order to best fit all the pump-down curves (50°C, 100°C, 120°C and 150°C). Then, using these best-fit parameter values the bake-out curve at 50°C and 150°C was calculated to cross-check the validity of the model.
Note that for the fitting, only the final part of each pump-down was considered (see Fig. 4.11).

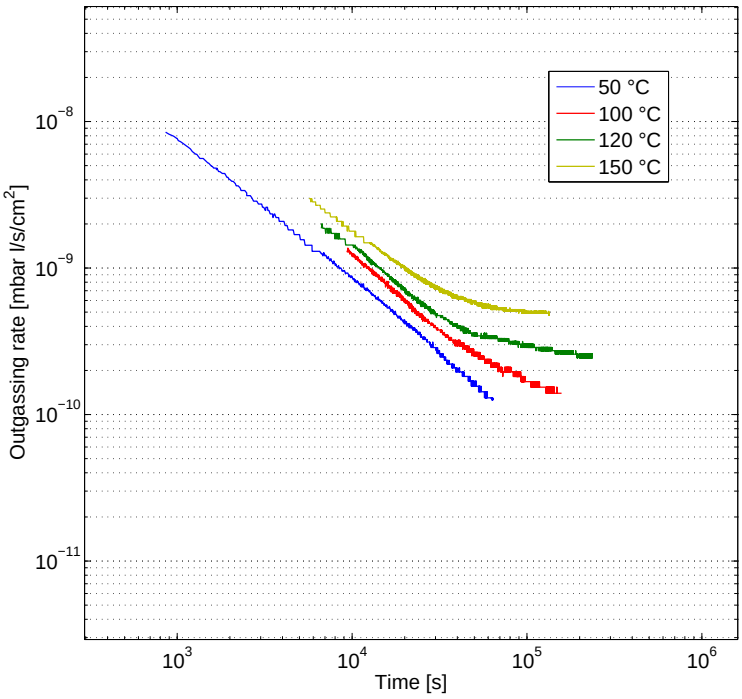

Figure 4.11: Data used for RMS minimization code.

Temkin isotherm fitting

The results of the optimization are shown in Fig. 4.12.

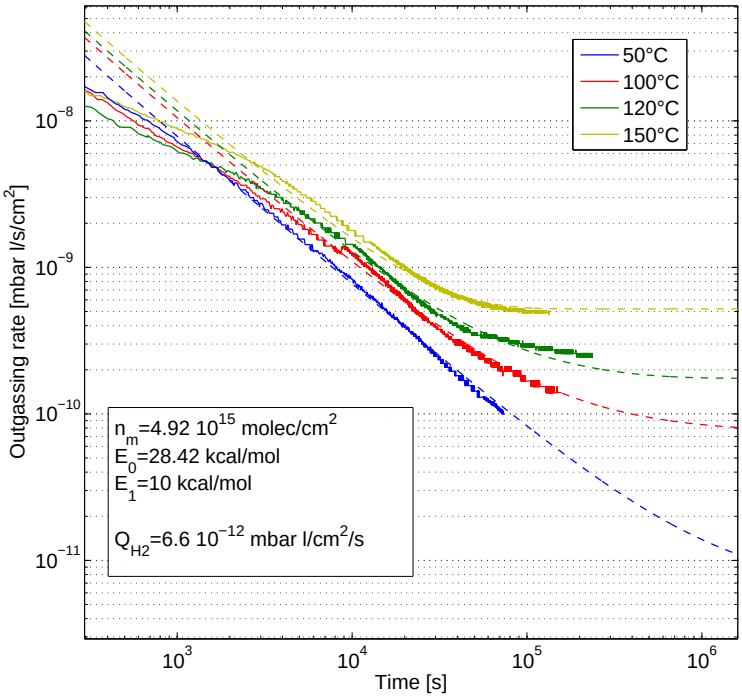

Figure 4.12: Results of the optimization for Temkin isotherm and diffusion model for H_2: simulations (dashed curves) vs real data (continuous curves).

The best fitting parameters for Temkin isotherm are summarized in Tab. 4.4. As

$\mathbf{n_m}$	$\mathbf{E_1}$	$\mathbf{E_0}$	$\mathbf{Q_{H_2,20^\circ}}$
4.92×10^{15} $\frac{\text{molecules}}{\text{cm}^2}$	10 $\frac{\text{kcal}}{\text{mole}}$	28.42 $\frac{\text{kcal}}{\text{mole}}$	6.6×10^{-12} $\frac{\text{mbar}\ell}{\text{cm}^2\text{s}}$

Table 4.4: Parameters obtained with Temkin isotherm optimization for pump-down data at different temperatures.

can be seen, the fitting is in agreement with the experimental results, except in the last part of the pump-down.

In order to check the optimized parameters we compared the calculated and measured curves of the bake-out 50°C/150°C (Fig. 4.13). The simulation, although in general good agreement with the profile, presents a limitation: the maximum calculated outgassing rate (edge around 10^{-8} mbar) is higher than the measured one. This could be justified by two explanations: not uniform temperature distribution on the chamber; the Penning mode of operation switching at 10^{-5} mbar, so the consequent difficulty to read the exact pressure at that level.

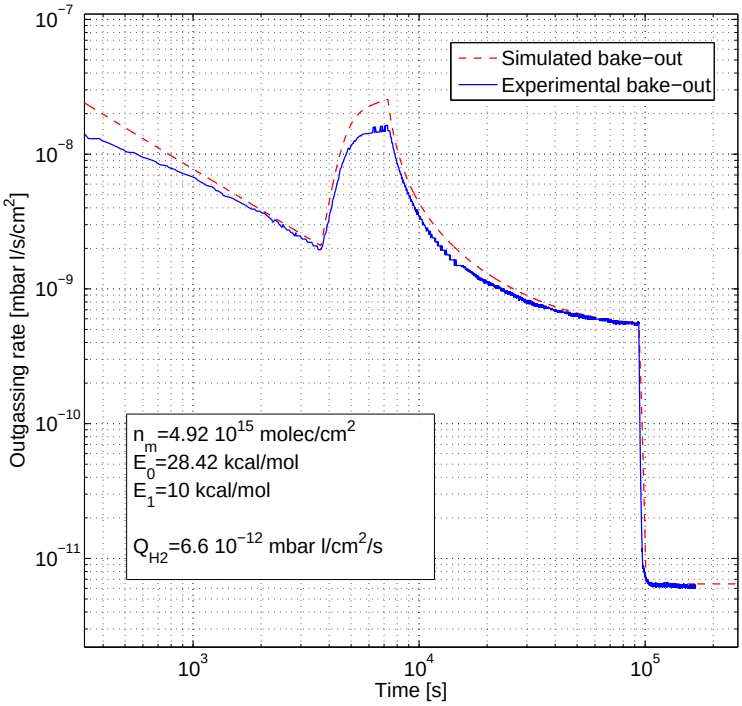

Figure 4.13: Results of the optimization for Temkin isotherm and diffusion model for H_2 on bake-out outgassing rate curve.

Freundlich isotherm fitting

For Freundlich isotherm, the same steps as before were performed.
The results are shown in Fig. 4.14 and Tab. 4.5.

$\mathbf{n_m}$	$\mathbf{E'}$	$\mathbf{Q_{H_2,20^\circ}}$
1.54×10^{16} $\frac{\text{molecules}}{\text{cm}^2}$	29.7 $\frac{\text{kcal}}{\text{mole}}$	5.8×10^{-12} $\frac{\text{mbar}\ell}{\text{cm}^2\text{s}}$

Table 4.5: Parameters obtained with Freundlich isotherm optimization for pump-down data at different temperatures.

Note that the density of sites n_m is increased by a factor three in comparison to Temkin isotherm and the parameter E' is outside Temkin energy interval, $[E_1, E_0]$.

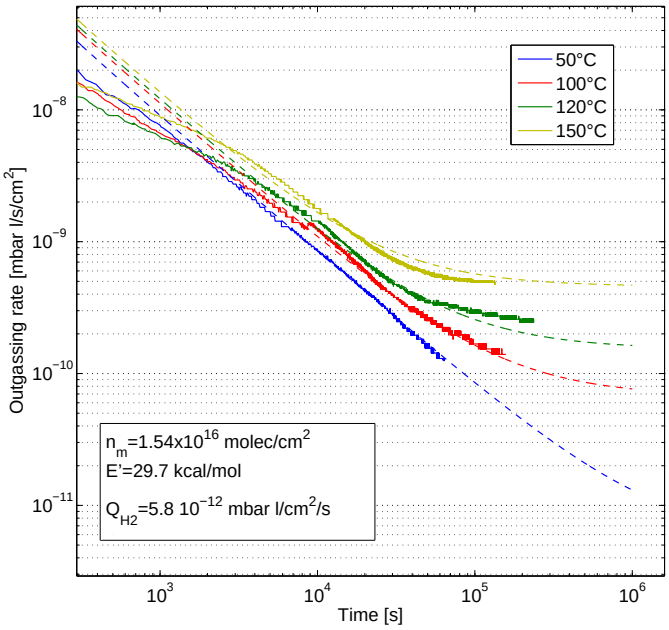

Figure 4.14: Pump-down curves calculated by the Freundlich isotherm at different temperatures (50°C, 100°C, 120°C, 150°C).

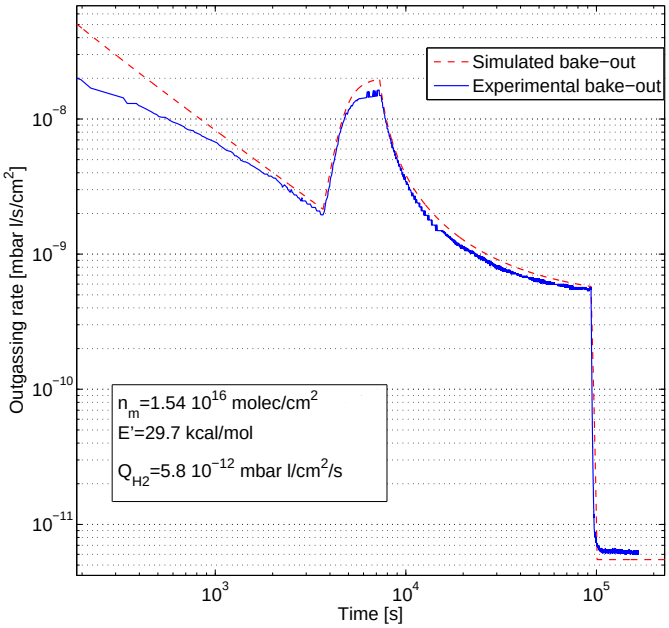

Figure 4.15: Results of the optimization for Freundlich isotherm and diffusion model for H_2 on bake-out pressure curve.

Sips isotherm fitting

As for Freundlich isotherm, Sips presents two main parameters: n_m and E'. The resulting fit and parameters are shown in Fig. 4.16, Fig. 4.17 and Tab. 4.6.

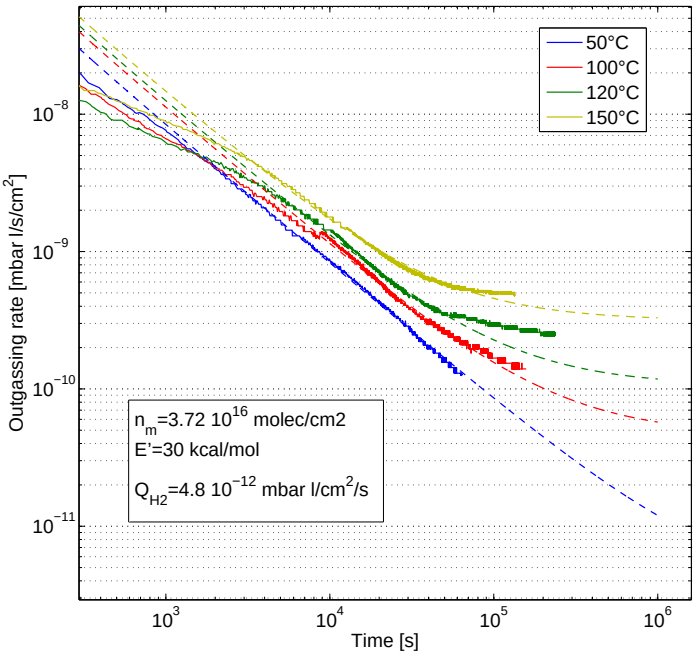

Figure 4.16: Pump-down curves calculated by the Sips isotherm at different temperatures (50°C, 100°C, 120°C, 150°C).

$\mathbf{n_m}$	$\mathbf{E'}$	$\mathbf{Q_{H_2,20^\circ}}$
3.72×10^{16} $\frac{\text{molecules}}{\text{cm}^2}$	30 $\frac{\text{kcal}}{\text{mole}}$	4.8×10^{-12} $\frac{\text{mbar}\ell}{\text{cm}^2\text{s}}$

Table 4.6: Parameters obtained with Sips isotherm optimization for pump-down data at different temperatures.

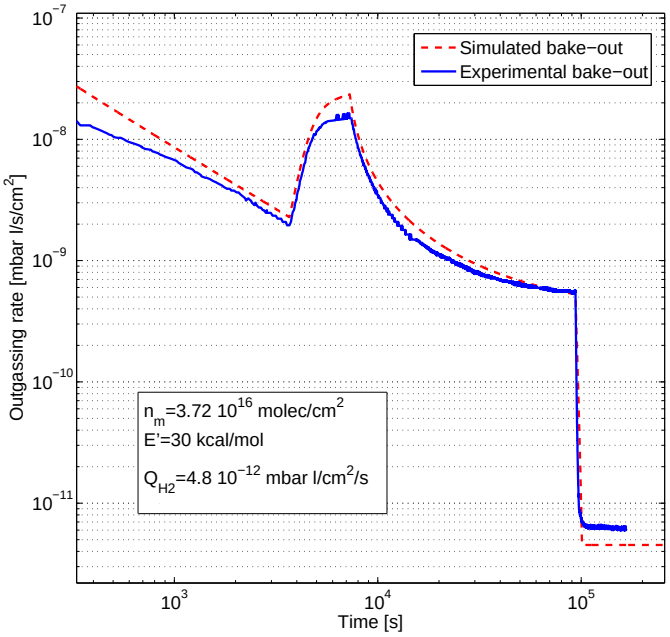

Figure 4.17: Results of the optimization for Sips isotherm and diffusion model for H_2 on bake-out outgassing rate curve.

Comparison between Temkin, Freundlich and Sips isotherms

In the literature various studies can be found on isotherm comparison [12, 15]. Ho [12] in particular, focuses his study on different error functions in order to analyse isotherm's fittings. For our project, it has been decided to consider the Root Mean Square error function, as defined in Eq. 4.2.

$$RMS = \sqrt{\sum_{i=1}^{N} \frac{1}{N} \left(\frac{p_i^{real} - p_i^{sim}}{p_i^{real}} \right)^2} \tag{4.2}$$

The results for the 3 isotherms are summarized in Tab. 4.7. It can be seen that

	Temkin	**Freundlich**	**Sips**
$\mathbf{RMS_{hp50°C}}$	0.08	0.05	0.03
$\mathbf{RMS_{hp100°C}}$	0.09	0.06	0.03
$\mathbf{RMS_{hp120°C}}$	0.05	0.15	0.03
$\mathbf{RMS_{hp150°C}}$	0.08	0.12	0.04
$\mathbf{RMS_{bake-out}}$	0.15	0.17	0.25

Table 4.7: Summary of RMS for the three isotherms.

Sips has the lowest RMS, except for outgassing curves during the bake-out. Temkin gives the best average over all measurements.

4.2.4 Why all isotherms give 1/t behaviour?

As shown in previous sections, the three isotherms give 1/t pump-down curves, that is:

$$p \propto \frac{1}{t} \tag{4.3}$$

Since the pressure evolution of a chamber in molecular regime is governed by walls outgassing, Eq. 4.3 can be re-written as:

$$\frac{dN}{dt} \propto \frac{1}{t} \tag{4.4}$$

From N and θ definitions dN/dt we obtain:

$$\frac{dN}{dt} = An_m \frac{d\theta}{dt} \propto \frac{d\theta}{dt} = \frac{\partial\theta}{\partial p}\frac{dp}{dt} \tag{4.5}$$

From Eq. 4.3:

$$\frac{d\theta}{dt} \propto -\frac{\partial\theta}{\partial p}\frac{1}{t^2}$$

Finally, in order to satisfy 4.4 :

$$\boxed{\frac{\partial\theta}{\partial p} \propto \frac{1}{p}} \tag{4.6}$$

This is the only requirement for an isotherm model to give 1/t behaviour during a pump-down.
It can be seen that condition 4.6 is satisfied if two hypothesis are set:

- Langmurian assumption for a single site of energy E: the desorption reaction is assumed to be of the first order;
- Energy density of sites $\rho(E)$ "almost" constant .

The demonstration comes from the evolution of the molecular density on the surface phase, starting from isotherms definition:

$$\theta(p) = \int \rho(E)\theta_L(p,E)dE$$

Considering $\rho(E) = cte$ in an interval $[E_1, E_0]$ and recalling the definition of θ_L, the integral gives:

$$\theta(p) = \int_{E_1}^{E_0} cte \frac{\frac{p}{p_*}e^{E/RT}}{1+\frac{p}{p_*}e^{E/RT}}\, dE$$

$$\theta(p) = cte * RT\left[\ln\left(1+\frac{p}{p_*}e^{E/RT}\right)\right]_{E_1}^{E_0}$$

$$\theta = cte * RT \ln\left(\frac{1+\frac{p}{p_*}e^{\frac{E_0}{RT}}}{1+\frac{p}{p_*}e^{\frac{E_1}{RT}}}\right)$$

It is clear that Temkin is an example of this isotherm type (replacing *cte* with $1/(E_0 - E_1)$). Using a simplified version of Temkin isotherm [28]:

$$\theta = \frac{RT}{E_0 - E_1} \ln\left(\frac{p}{p_*} e^{\frac{E0}{RT}}\right)$$

$$\theta = \frac{RT}{E_0 - E_1} \ln(p) - \frac{RT}{E_0 - E_1} \ln(p_*) + \frac{E0}{E_0 - E_1}$$

$$\Longrightarrow \boxed{\frac{\partial \theta}{\partial p} = \frac{RT}{E_0 - E_1} \frac{1}{p} \propto \frac{1}{p}} \tag{4.7}$$

This shows that starting from Langmuir isotherm and having a constant distribution it's a sufficient condition to have 4.6 satisfied.

For Freundlich isotherm, the energy density follows an exponential behaviour (see Eq. 3.14). Anyway, in the considered energy interval (between 10 kcal/mole, to 50 kcal/mole), the distribution is almost constant. In fact, from Eq. 3.15:

$$\theta_F = \left(\frac{p}{p_*}\right)^{\alpha}$$

$$\Longrightarrow \boxed{\frac{\partial \theta}{\partial p} \propto \frac{1}{p^{1-\alpha}}} \tag{4.8}$$

This means that to satisfy condition 4.6 we should have $\alpha \ll 1$. Recalling its definition:

$$\alpha = \frac{RT}{E'}$$

and using usual values of energy (29.7 kcal/mole) and temperature (295 K)

$$\alpha = 0.0198 \ll 1$$

The demonstration is not needed for Sips isotherm, since it's the general case of Freundlich, with the same behaviour at low pressures.

4.3 Measurements on treated surfaces

The same measurements described in the last section have been performed on three surface treated chambers: air-baked chamber, electropolished chamber and a silver/palladium coated chamber. The measurements on these surfaces were made to understand how water desorption changes with the surface composition/roughness/nature. The set-up used for this campaign is the same as shown in Fig. 4.7, except for the orifice position. The first 1.2 mm conductance has been removed, and a 7 mm conductance (pumping speed of 5.65 ℓ/s for water at 20°C) has been installed between Vessel 1 and the treated chamber, as in Fig. 4.18. In this way V2 pressure is influenced by the treated surface only.

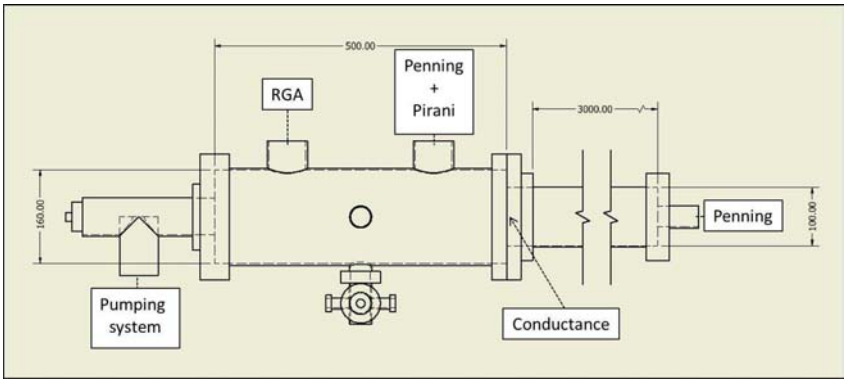

Figure 4.18: Scheme of experimental set-up, showing the position of the 7-mm diameter orifice.

4.3.1 Air baked chamber

The air baked surface was obtained with a heating treatment from the 3 meters clean chamber (V2). The volume has been heated in air at 300°C for 24 hours. The considered surface and volume for the simulations are $A_2 = 9425cm^2$ and $V_2 = 23.7\ \ell/s$. A picture of the chamber is shown in Fig. 4.19. The first pump-down,

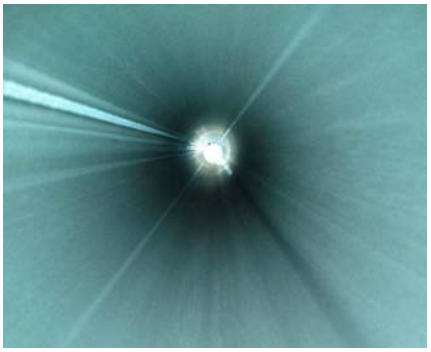

Figure 4.19: Picture of the internal surface after air-bake treatment.

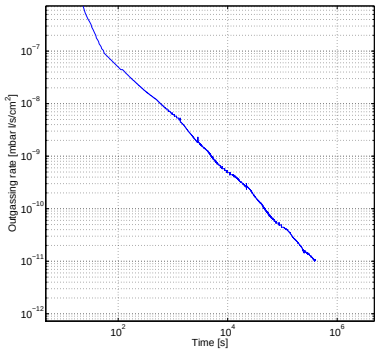

Figure 4.20: First pump-down curve at 20°C.

performed at 20°C, showed that air-baked surface has 1/t behaviour (Fig. 4.20). The results of the pump-down curves at different temperatures and during a bake-out are shown in Fig. 4.21 and Fig. 4.22.

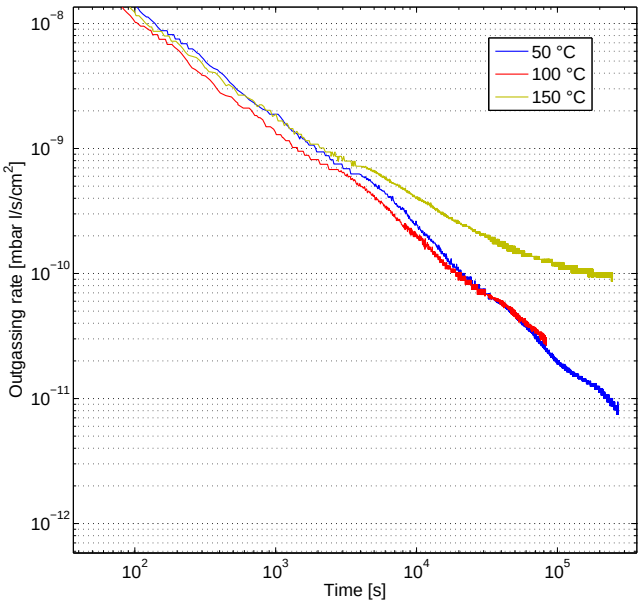

Figure 4.21: Pump-down curves at 50°C, 100°C, 150°C for air-baked chamber.

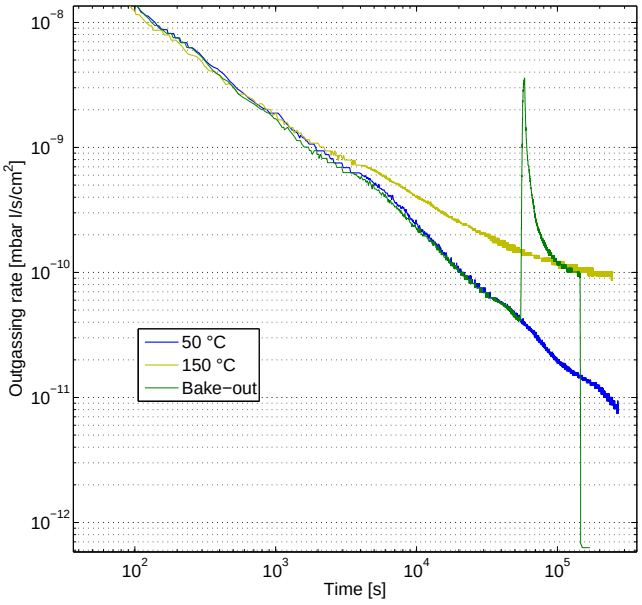

Figure 4.22: Bake out curve: here the bake started after 15 hours of pumping. In the figure are represented the pump-down curves at 50°C and 150°C.

4.3.2 Electropolished chamber

Four pipes DN 100, 50 cm long, ($A_{EP} = 6361\ cm^2$) underwent electropolishing after vacuum firing treatment[2]. CERN procedure for this treatment is described in App. B.2.
Fig. 4.23 shows the internal surface of the pipes after installation on the system. Fig. 4.24 represents the outgassing rate at almost 26°C (the laboratory cooling system was out of order during this measurement).
The results of the pump-down curves at different temperatures and bake-out are shown in Fig. 4.25 and Fig. 4.26.

Figure 4.23: Picture of installed electropolished pipes with mirror-like surface.

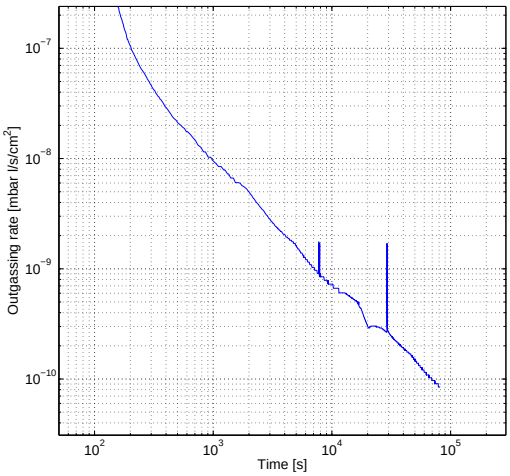

Figure 4.24: First pump-down curve for vacuum-fired and electropolished chamber at 26°C.

[2]Vacum firing treatment consists in heating in a vacuum furnace to temperature up to 1000°C. At CERN it is carried out at 950°C for 2 hours in a vacuum better than 10^{-5} mbar at the highest temperature. [3]

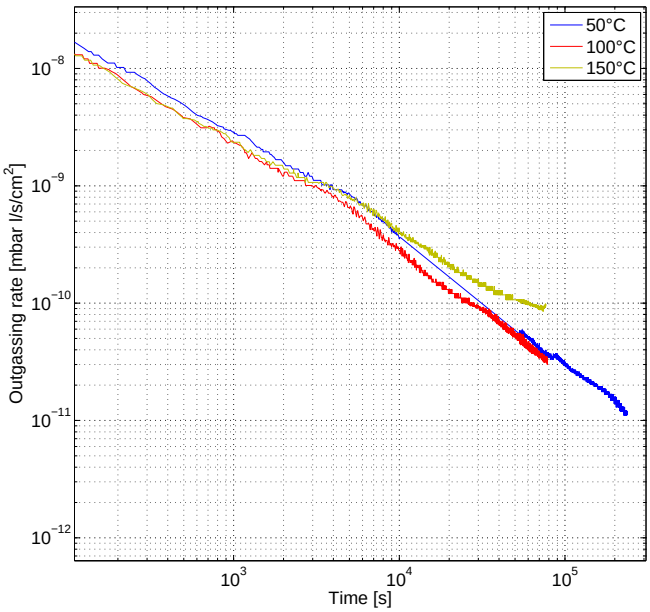

Figure 4.25: Pump-down curves at 50°C, 100°C, 150°C for vacuum-fired and electro-polished chamber.

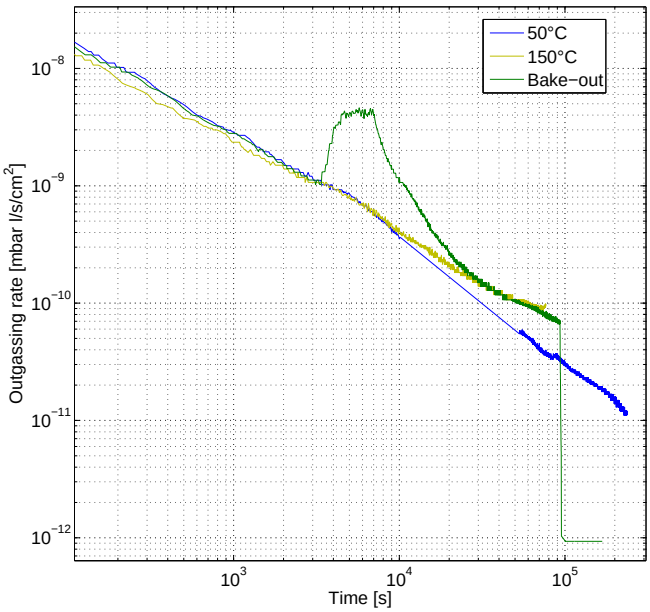

Figure 4.26: Bake-out of a vacuum fired and electro-polished chamber. The thermal cycle of the experiments is the same as in the untreated chamber.

4.3.3 Silver palladium coated chamber

This treated chamber has been obtained from a 316L 3 meter long pipe (DN100) after vacuum firing. The silver/palladium coating (250 nm thick) has been deposited on the surface by magnetron-sputtering from a wire with 70% Pd ans 30% Ag.
The results for this chamber showed the presence of a memory effect on the surface. In fact, if two equal measurements were repeated after a few bake-outs, a shift toward lower pressures was observed. For example, the change of 100°C curve is shown in Fig. 4.27.

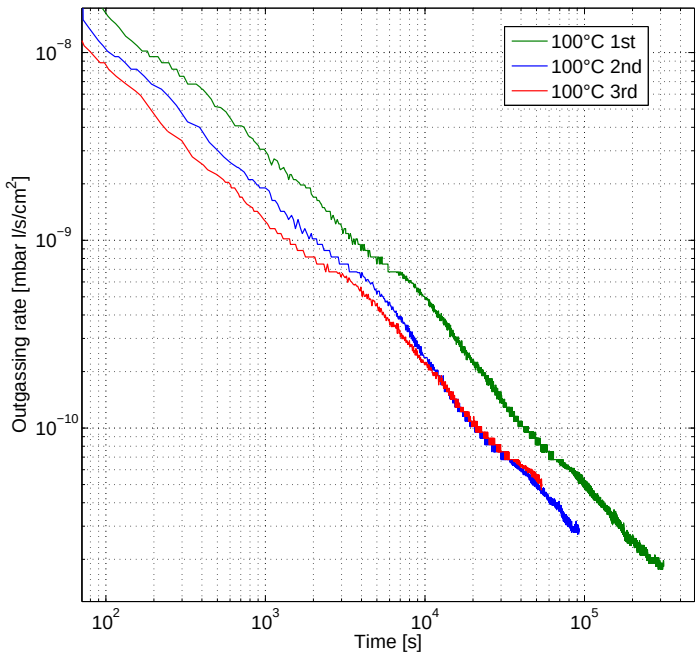

Figure 4.27: Silver/palladium coating: memory effect on 100°C pump-down curves. Between curve 1 and 2 the system underwent 5 bake-outs, while between 2 and 3 one bake-out.

For this reason, all measurements have been repeated three times. In Fig. 4.28 and Fig. 4.29 are shown the second set of experimental results.

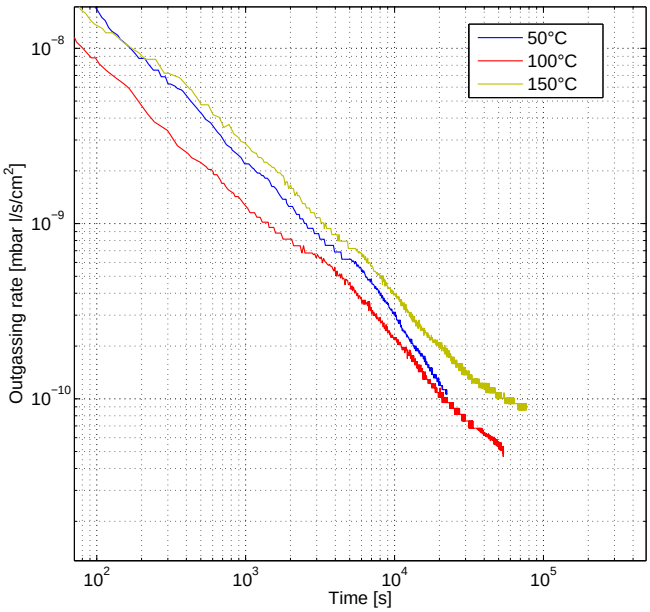

Figure 4.28: Pump-down curves at 50°C, 100°C, 150°C for silver/palladium coated chamber.

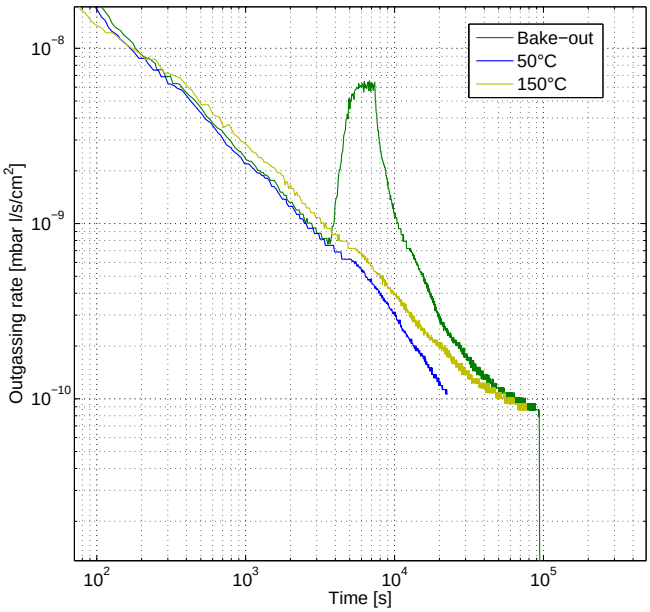

Figure 4.29: Bake-out of a silver/palladium coated chamber. The thermal cycle of the experiments is the same as in the untreated chamber.

4.4 Discussion of the results of pump-down curves at different temperatures

The desorption model proposed for the untreated stainless steel surface was unable to simulate the behaviour of the three treated chambers. In fact, the model implies that, when the temperature of the system is increased, the pump-down curve shifts (in log-log scale) toward higher outgassing rates. All treated surfaces instead presented an outgassing rate curve at 100°C lower than the curve at 50°C during the whole pump-down. This behaviour, in opposite direction compared to the isotherm model, prevented the achievement of a solution in the optimization code.

Comparison of the studied vacuum chambers

The outgassing rate comparison for each temperature is shown in Fig. 4.30.

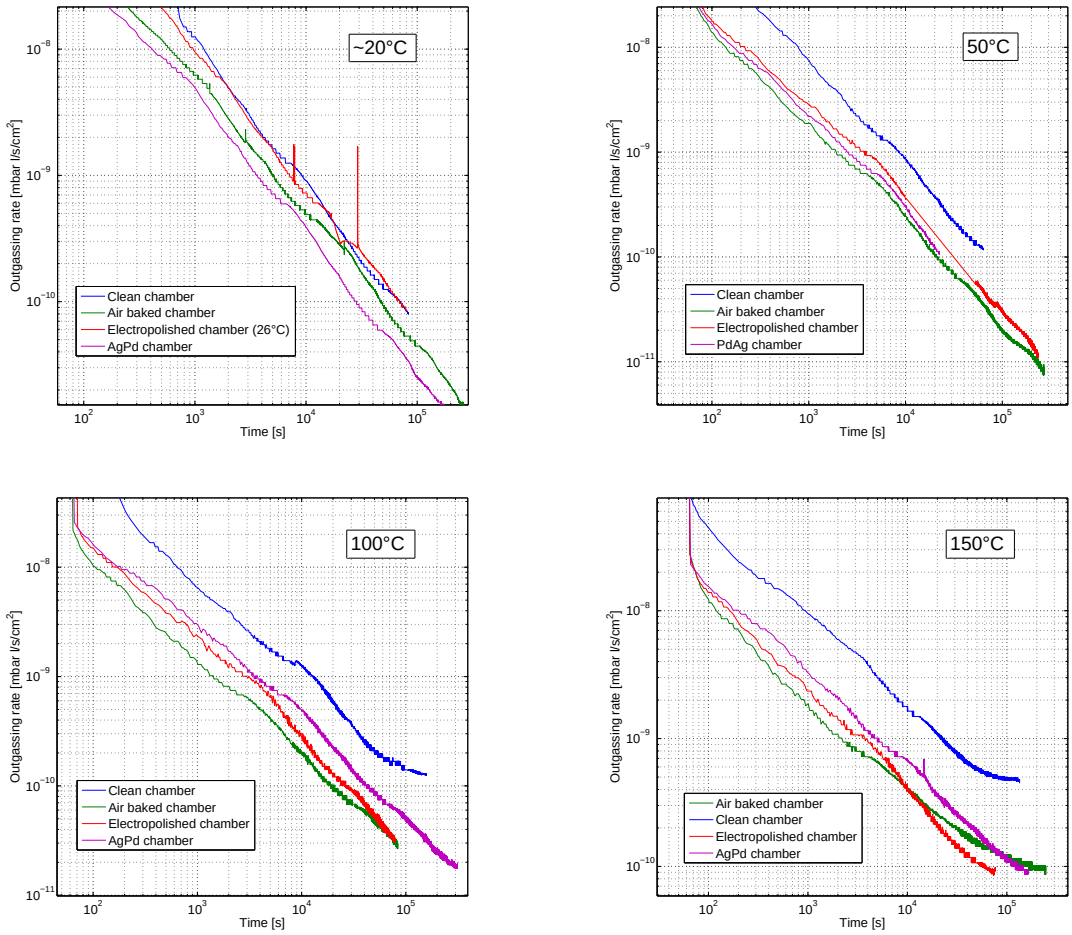

Figure 4.30: Comparison of pump-downs curves for as-received, air-baked, vacuum-fired/electropolished and silver/palladium coated chambers at different temperatures.

As can be noticed, all chambers follow 1/t behaviour at all temperatures, indepen-

dently from the treatment.
High temperature pump-down curves show an interesting behaviour: the gap between the treated chambers and the untreated chamber increases with the temperature. The former present an outgassing 3 to 5 times lower than the latter at 150°C. One possible explanation for this behaviour could be the influence of hydrogen outgassing. In fact, it is known that for air-baked and for vacuum fired chambers, Q_{H_2} is more than 2 order of magnitudes lower than on untreated chamber [1, 37, 38]. At high temperature, the hydrogen flux could have a role in water outgassing by reacting with surface oxides and hydroxides. Further investigations should be conducted about water-hydrogen reactions on metal surfaces, in order to understand this complex process.

Roughness influence

In order to characterize the surfaces, a roughness measurement with a stylus instrument was performed on 4 samples. Each sample (2 cm×50 cm plate, 1.5 mm thick) underwent the same treatments as the 4 experimental chambers: 316L as received, 316 L air-baked at 300°C, 316 LN vacuum fired and electro-polished, 316L vacuum fired and AgPd coated.
To compare the results, the arithmetic average of absolute values R_a, was considered. For each sample, the measurements were taken in two directions, X and Y, in 5 different positions. The values are shown in Tab. 4.8.

$\overline{\mathbf{R_a}}$	**Vacuum Fired+ Electropolished**	**300°C Airbaked**	**Untreated**	**AgPd Coated**
X [μ**m**]	0.096	0.253	0.3064	0.346
Y [μ**m**]	0.0768	0.2286	0.2206	0.276

Table 4.8: R_a values for the treated samples, averaged on X and Y directions.

Fig. 4.31 compares R_a with the outgassing of the surfaces after 10 hours of pumping at 50°C. As can be seen, there is no clear effect of the surface roughness on the outgassing rate. The electropolished chamber doesn't present a lower outgassing, as already experienced by Dylla [7].

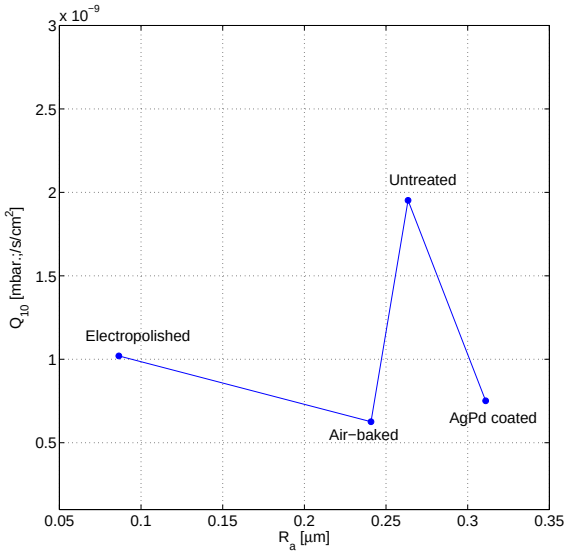

Figure 4.31: Roughness influence on the outgassing after 10 hours of pumping for 50°C pump-down curve.

XPS measurements

Other 4 samples, treated in the same way as the studied vacuum chambers, were analyzed by X-ray Photoelectron Spectroscopy (XPS). The samples were measured under a pressure of 2×10^{-9} mbar.
The main difference in the studied surfaces is represented by the iron and chromium proportions. For the untreated surface, iron was slightly higher than chromium. The air-bake treatment enhanced Fe presence and reduces Cr level. Conversely, the electropolishing increased the chromium content and decreases the iron peak. These results are in agreement with previous analysis on the same treatments on stainless steel surfaces [2].

Chapter 5

SPS vacuum improvement

The effect on a pressure profile of the addition of NEG lump pumps in LSS1 (Long Straight Section 1 of SPS) is evaluated in this chapter. The dumping system of SPS is located in this section, making this area the most radioactive of the LHC injectors. The high radiation level affects the insulation of ion pump cables, causing pumps to fail, making the needed vacuum more difficult to achieve.
NEG cartridges were thought to be good candidates as additional pumping to mitigate this problem.

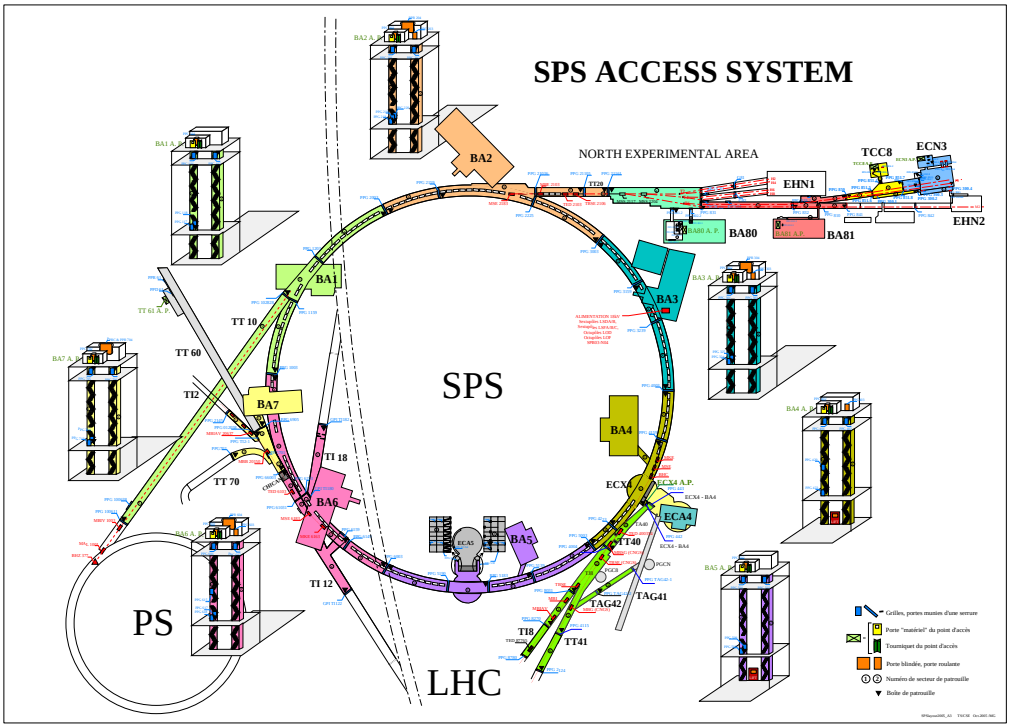

Figure 5.1: SPS overview.

5.1 Combination of ion pump with NEG

In LSS1, two third of ion pumps are connected to the beam line as shown in Fig. 5.2. The sublimation pumps found in the VPTC element, are installed above the VPSC ion pumps. Since these sublimators are no longer in use, the NEG cartridges can be installed in this volume. A Molflow [17] model was created in

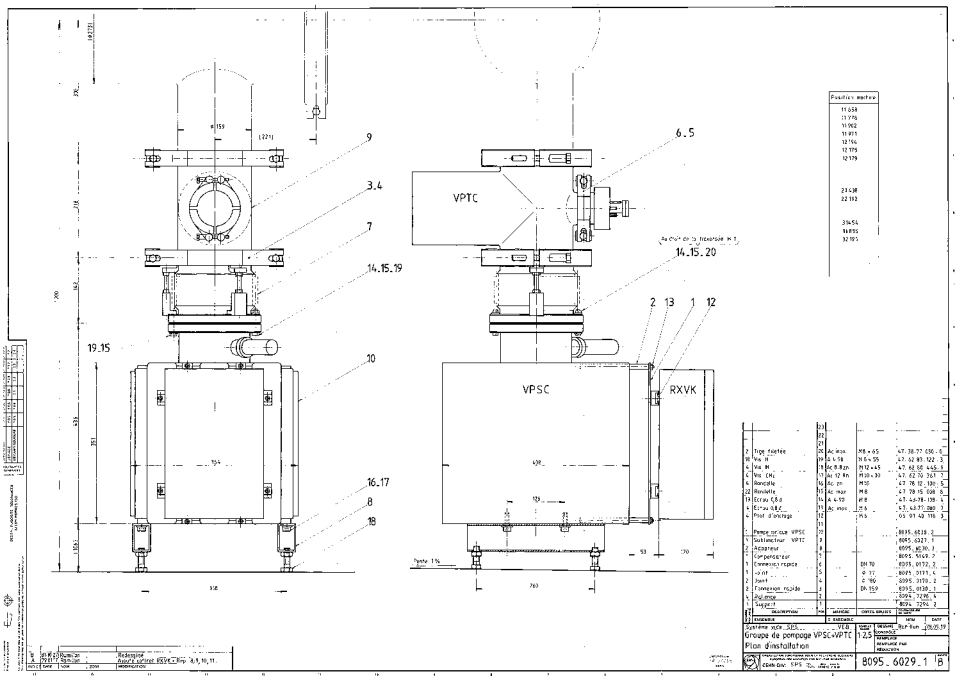

Figure 5.2: Pumping system schema for SPS pump VPICA.

order to calculate the influence on pressure and on the effective pumping speed of NEG cartridge. Later, NEG saturation time was obtained with a time dependent simulation using LTSpice software [8].
The analysis has been performed for different gases (N_2, H_2, H_2O, CO) assuming each was the only one present in the system.

5.1.1 Ion pump: Leybold IZ350

These ion pumps have a nominal pumping speed of 350 ℓ/s for N_2. A constant value of $S^{IP}_{N_2} = 150\ \ell/s$ was assumed in our model.
The pumping speed, for gases other than N_2, was obtained multiplying the speed by the suitable factor k_{IP} shown in Tab. 5.1.

Gas	Air	N_2	H_2	CO	H_2O
k_{IP}	1	1	1.5-2	0.9	0.8

Table 5.1: Conversion factor for Ion Pump [3].

5.1.2 NEG pump: CapaciTorr D1000

This pump, commercialised by SAES Getters presents NEG plates inserted in a metal body (see Fig. 5.3). After its activation, i.e. when native oxide layer

Figure 5.3: NEG pump CapaciTorr D1000 by SAES Getter, [11].

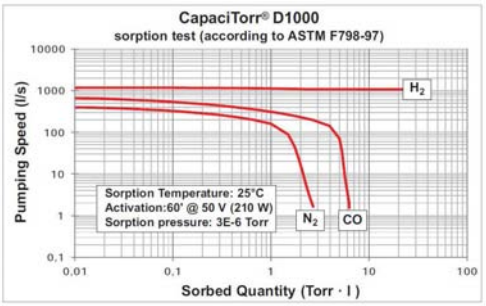

Figure 5.4: Pumping speed variation with quantity of sorbed molecules, [11].

is dissolved in the NEG material [3], the pump has a decreasing pumping speed dependent on the amount of adsorbed gas.
As can be seen in Fig. 5.4, the capacity is different for each gas. Note that when the pump is saturated with a gas (except for H_2), the pumping speed for other gases is also reduced. For example, if NEG is saturated with water, hydrogen pumping speed is also reduced.

5.1.3 Molflow model and analysis

In order to compare the effective pumping speed with and without NEG, two geometries have been studied in Molflow.
The first, without CapaciTorr D1000, is shown in Fig. 5.5 (case A). In order to

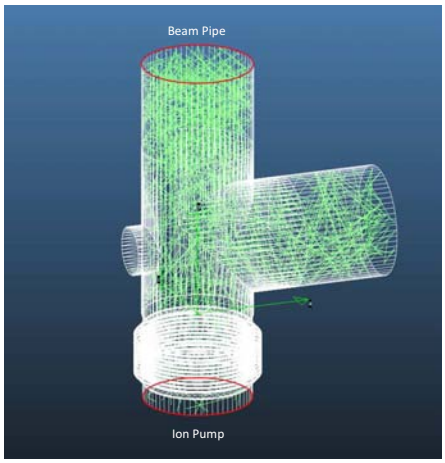

Figure 5.5: Molflow model of VPIC connection pipe.

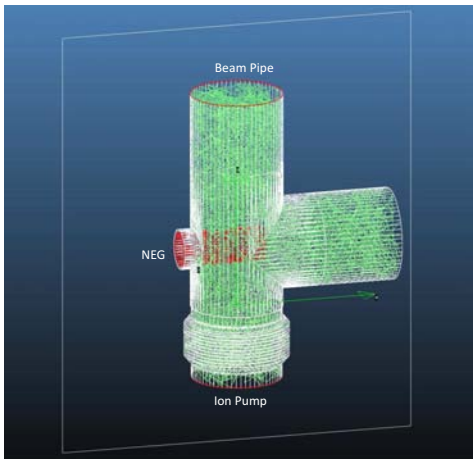

Figure 5.6: Molflow model of VPIC connection pipe with added NEG.

calculate the effective pumping speed on the beam pipe (surface 1), the following steps have been performed:

1. A fixed flux has been imposed on surface 1. The transmission probability τ_A (from surface 1 to the ion pump) was calculated in Molflow, obtaining $\tau_A = 0.26$;

2. The conductance of the pipe was determined from Eq. 2.16. For H_2:

$$C^A_{H_2} = \frac{\bar{v}_{H_2}}{4} A_1 \tau_A = 2269 \, \frac{\ell}{s} \tag{5.1}$$

   where $\bar{v}_{H_2} = 1761$ m/s at room temperature (from Tab. 2.3), and A_1 is the surface on the top of the vacuum chamber.

3. The effective pumping speed was calculated as the combination of $S^A_{H_2} = S^{IP}_{N_2} k_{IP,H_2} = 300 \, \ell/s$ and $C^A_{H_2}$.

$$S^{A,eff}_{H_2} = \frac{S\,C}{S + C} = 265 \, \frac{\ell}{s}$$

Tab. 5.2 summarizes the values obtained for different gases.

$\mathbf{S^{A,eff}}[\ell/\mathbf{s}]$	N_2	H_2	CO	H_2O
Ion Pump	121	265	111	105

Table 5.2: Effective pumping speed for the ion pump.

The second simulation, with NEG and ion pump combined, is shown in Fig. 5.6 (case B). The NEG pump, inserted in the sublimation cavity was simulated as a cylinder.
The effective pumping speed calculation for different gases needs the following inputs: the outgassing load from the beam line, the IP pumping speed and the NEG pumping speed.
To evaluate the outgassing load, a pressure of 10^{-8} mbar for the ion pump alone was assumed on surface 1 (in agreement with SPS experimental data).
For example, for hydrogen, the incoming flux is:

$$Q_{1,\mathrm{H_2}} = p_1^A \, S_{H_2}^{A,eff} = 2.65 \times 10^{-6} \, \frac{\mathrm{mbar} \cdot \ell}{\mathrm{s}} \tag{5.2}$$

The first result of the simulation is the pressure p_1^B, that results lower than 10^{-8} mbar thanks to NEG pumping (see Tab. 5.3).

$\mathbf{p_1}[\mathbf{mbar}]$	N_2	H_2	CO	H_2O
A	10^{-8}	10^{-8}	10^{-8}	10^{-8}
B	3.3×10^{-9}	2.7×10^{-9}	2.3×10^{-9}	2.8×10^{-9}

Table 5.3: Pressure on surface 1 in cases A (ion pump alone) and B (ion pump combined with NEG lump pump).

Since Q_1 is imposed, the effective pumping speed for case B is directly calculated from p_1^B values:

$$S^{B,eff} = \frac{Q_1}{p_1^B}$$

The results are shown in Tab. 5.4.

$\mathbf{S^{eff}}[\ell/\mathbf{s}]$	N_2	H_2	CO	H_2O
A	121	265	111	105
B	347	953	454	357

Table 5.4: Effective pumping speed on surface 1 in cases A (ion pump alone) and B (ion pump combined with NEG lump pump).

Tab. 5.5 shows the percentage of molecules pumped by the two pumps in NEG fully activated scenario. Note that the NEG cartridges pump more than 70% of molecules for all gases. This is due both to the bigger pumping speed and to the NEG position (closer to the beam pipe).

$\mathbf{Q_{pump}/Q_{tot}}[\%]$	N_2	O_2	H_2	CO	H_2O
Ion Pump	26.2	26.8	22.7	15.9	21.9
CapaciTorr D1000	73.8	73.2	77.3	84.1	78.1

Table 5.5: Percentage of pumped molecules in Ion pump and NEG for different gases.

5.1.4 Conductance analysis

In order to verify the validity of the simulation, the problem was analysed using a different approach, exploiting the electrical network analogy (see Sec. 2.6).
From the Molflow model, the transmission probabilities between the three surfaces were obtained (τ_{IP}^{beam} or τ_{13}, τ_{NEG}^{beam} or τ_{12} ,τ_{IP}^{NEG} or τ_{23}). The conductances between the three surfaces were calculated and implemented in the electrical equivalent network of Fig. 5.7.

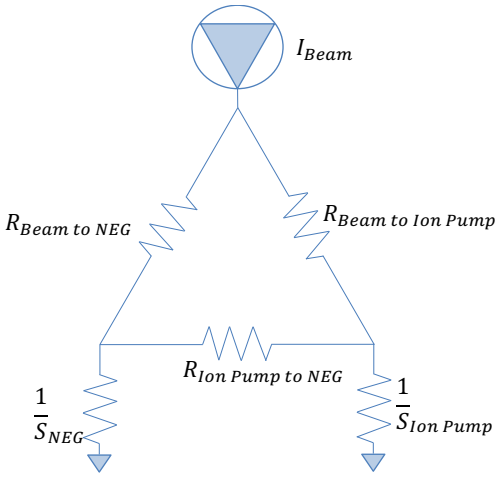

Figure 5.7: Electrical equivalent network for VPTC pumping group.

Where:

$$\begin{cases} R_{Beam\ to\ NEG} = \frac{1}{C_{Beam\ to\ NEG}} \\ R_{Ion\ Pump\ to\ NEG} = \frac{1}{C_{IonPump\ to\ NEG}} \\ R_{Beam\ to\ Ion\ Pump} = \frac{1}{C_{Beam\ to\ Ion\ Pump}} \\ I_{Beam} = Q_1 \end{cases} \tag{5.3}$$

Operating a triangle-star conversion, the system was solved in order to find the equivalent resistance, i.e. the inverse of the effective pumping speed. The results are similar to the previous analysis (see Tab. 5.6). The difference between the

$\mathbf{S^{eff}}[\ell/s]$	N_2	H_2	CO	H_2O
Electric network	339	932	428	330
Molflow pressures	347	953	454	357

Table 5.6: Comparison of the results obtained with the two approaches.

two approaches, less than 10%, is due to statistical scattering of the Monte Carlo simulation.

5.1.5 Time dependent simulation

A time dependent simulation in LTspice was performed to evaluate the pumping speed variation and saturation time of the NEG lump pump.
In this model only the main gas sources of an unbaked system (water and hydrogen) were considered. From Sec. 2.8.1, water outgassing can be calculated as:

$$Q_{H_2O} = \frac{3 \times 10^{-9}}{t[h]} \frac{\text{mbar} \cdot \ell}{\text{s cm}^2} \tag{5.4}$$

Hydrogen outgassing for stainless steel was obtained from Tab. 2.8:

$$Q_{H_2} = 3 \times 10^{-12} \frac{\text{mbar} \cdot \ell}{\text{s cm}^2} \tag{5.5}$$

The pumping speeds, S^{NEG} and S^{IP}, were modified following the pumps specifications. For the ion pump, H_2 and H_2O pumping speeds were obtained via k_{IP}. For NEG pump, hydrogen pumping speed was assumed to undergo a decrease due to water saturation.

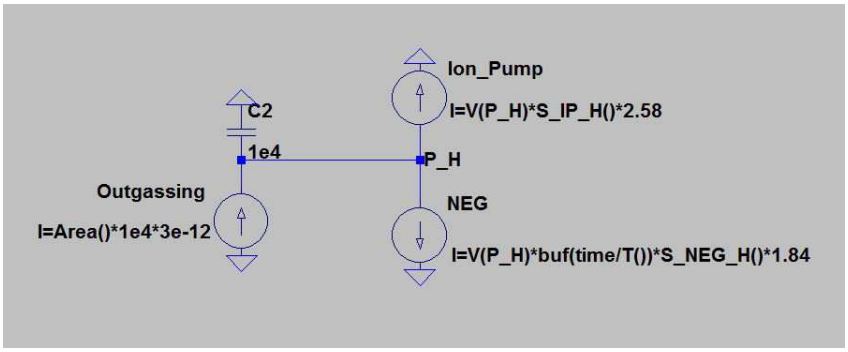

Figure 5.8: LTspice model for water outgassing. An equivalent model has been created for H_2 outgassing.

The simulations have been launched for different gas loads (surfaces of 1 m^2, 10 m^2, 50 m^2 and 100 m^2) and different delay from the beginning of the pump-down and the NEG activation times (10 and 24 hours after the start of the pump-down). The activation of the pump was simulated as the moment in which this has pumping speed bigger than zero; the gas load due to the activation process was not included in the model.
Fig. 5.9, shows how NEG activation affects the pump-down: when this pump is activated, a "jump" toward lower pressures is observed. The difference between the pressure in the NEG-on and NEG-off scenario tends to decrease until the NEG no longer contributes to the pump-down.

The improvement of the pressure after activation is bigger when the pump is activated at lower pressures (see Tab. 5.7).

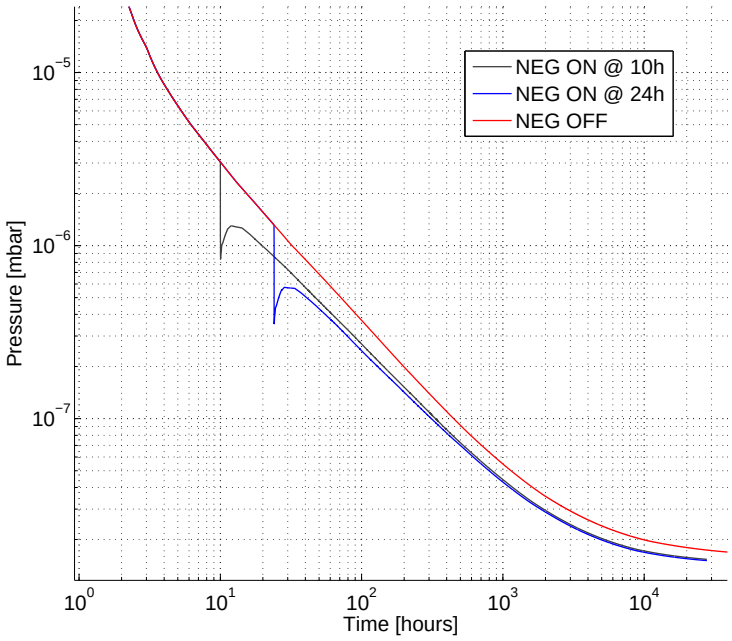

Figure 5.9: Pressure evolution with (blue and black lines) and without (red lines) NEG activation.

p_{IP}[mbar]	1.6×10^{-6}	6.9×10^{-7}	4×10^{-8}	1.7×10^{-8}
$p_{(IP+NEG)}/p_{IP}$	3.8	4	4.6	5

Table 5.7: Pressure improvement variation: p_{IP} and p_{IP+NEG} are respectively the pressure before and after activation. Their ratio increases as the p_{IN} decreases.

The time until saturation was evaluated (Fig. 5.11) assuming that the pump was activated after 10 hours of pumping. With this condition and after one year of operation, the NEG is not saturated when the outgassing flux is lower than the water outgassing of 37.5 m^2 of stainless steel.

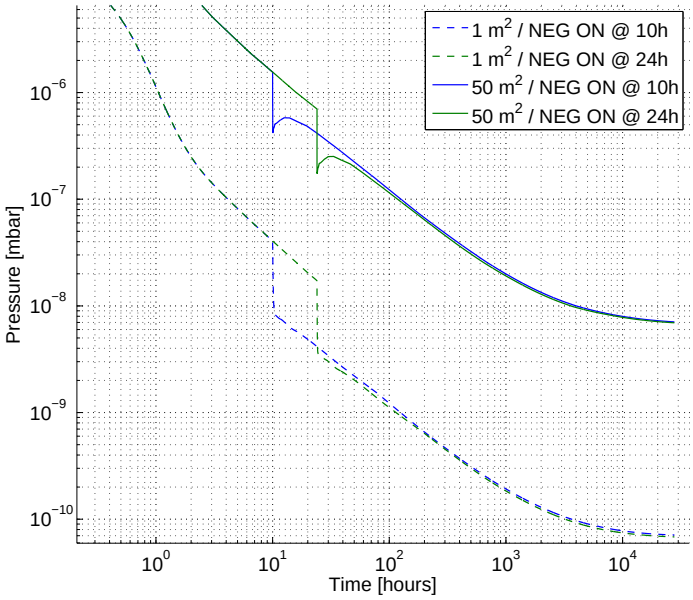

Figure 5.10: Pressure evolution with NEG activation after 10 hours (blue lines) and 24 hours (green lines) with gas load from 1 m^2 (dashed lines) and 50 m^2 (solid lines).

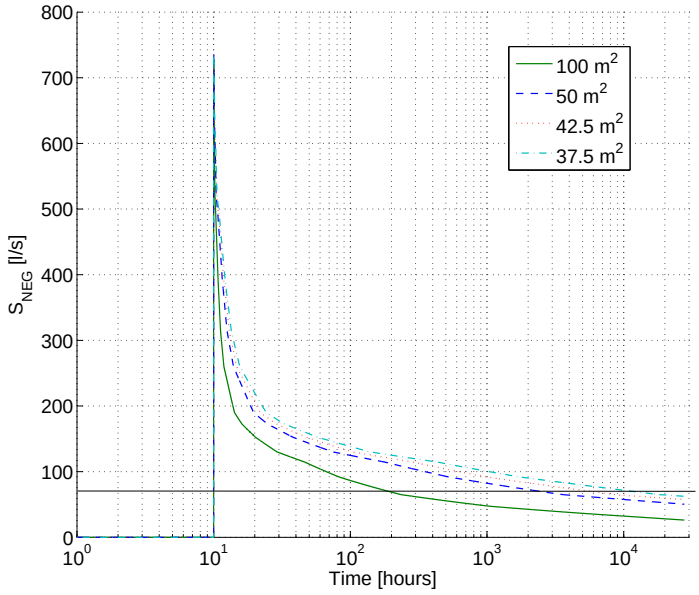

Figure 5.11: NEG effective pumping speed vs Time of pumping for 4 different gas loads: 37.5, 42.5, 50, 100 m^2. These loads are equivalent to p_{IP} of 1.1×10^{-6}, 1.3×10^{-6}, 1.6×10^{-6}, 3×10^{-6} mbar respectively.

5.2 BA1 Simulation

In this section the LSS1 vacuum system is simulated. To simulate pressure profiles in the beam line the following steps have been performed:

1. Calculation of transmission probabilities of every element of the beam line;
2. Development of an equivalent electrical network on LTspice software [8];
3. Update of pumping units with NEG pumps.

5.2.1 Transmission probability calculation for a component

To show how transmission probabilities are calculated, the analysis of MKPA 11955 (kicker magnet) is presented.
For each element, the 3D model of the volume under vacuum has been created using Autodesk Inventor (see Fig. 5.12 and Fig. 5.13).

Figure 5.12: Section view of 3D model.

Figure 5.13: Internal volume of MKPA.

This model was exported to Molflow [17] and the transmission probabilities (τ) were calculated between all the open surfaces: in this example, between the entrance and the exit of the beam and the apertures of the four pumps.
Complex elements were divided in several parts to have a better simulation using the electrical network analysis. In this example MKPA was divided in four pieces (Fig. 5.14).

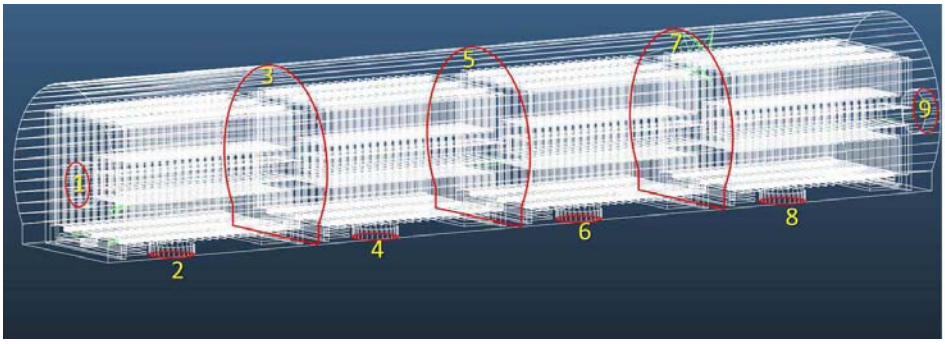

Figure 5.14: Molflow model for MKPA 11955. In the figure are highlighted the surfaces used for transmission probabilities calculations.

5.2.2 LTspice model for a component

With the obtained transmission probabilities, the conductances were calculated using Eq. 2.16:

$$C = C' A_1 \tau_{1\to 2}$$

where A_1 is the area of the outgassing surface, and C' is the conductance of an orifice of unit surface area.
Finally, the equivalent electrical network was inserted in LTspice. For the kicker MKPA, it is shown in Fig. 5.15.

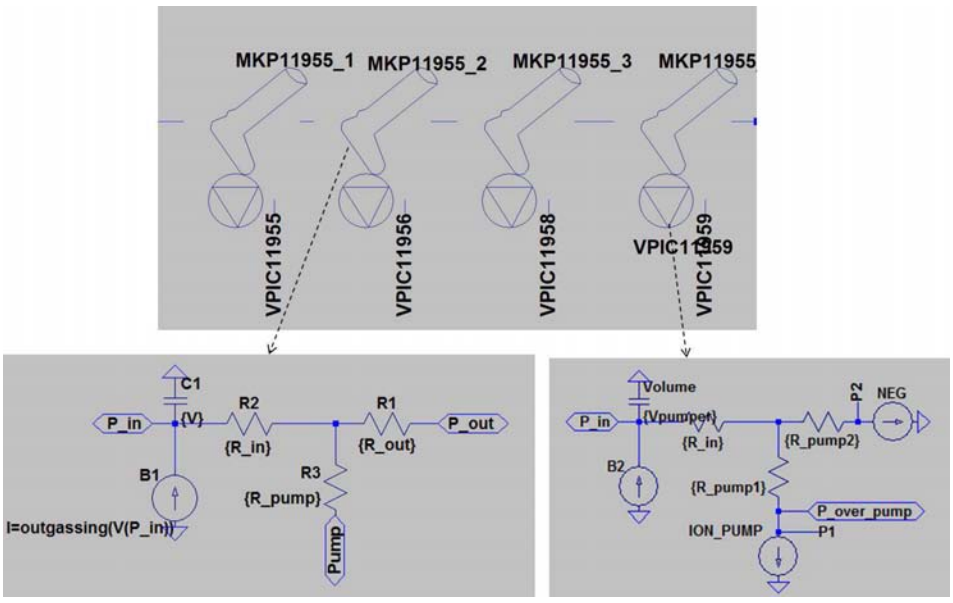

Figure 5.15: LTspice model for MKPA 11955. The four parts represents the volumes between surfaces shown in Fig. 5.14.

5.2.3 Global LTspice model

Following the steps described in previous section, the entire sector was recreated in LTspice (see Fig. C.1). The parameters of the simulation were chosen following these assumptions:

1. Pumping system: 27 ion-pumps with sublimator (Leybold IZ350, eligible of NEG adding), 12 ion pumps without sublimator (Leybold IZ400) and 10 small ion pumps (20 ℓ/s). The pumping speed for IZ350 and IZ400 was set at 150 ℓ/s and 200 ℓ/s respectively. NEG pumps installation has been simulated only on 5 pumping groups, close to the most critical elements (dumps TIDH and TIDVG);

2. Outgassing: in order to simulate water desorption of simple tubes, Temkin isotherm model with optimized parameters for unbaked chambers was implemented. For more complex elements (dumps or kickers) the following expression was used:
$$Q = kQ_{TEMKIN} \tag{5.6}$$
with $k_{KICK} = 10$ for kickers and $k_{DUMP} = 100$ for dumps.

In order to validate the model, the pressure profile has been compared with real data from SPS database (Fig. 5.16)

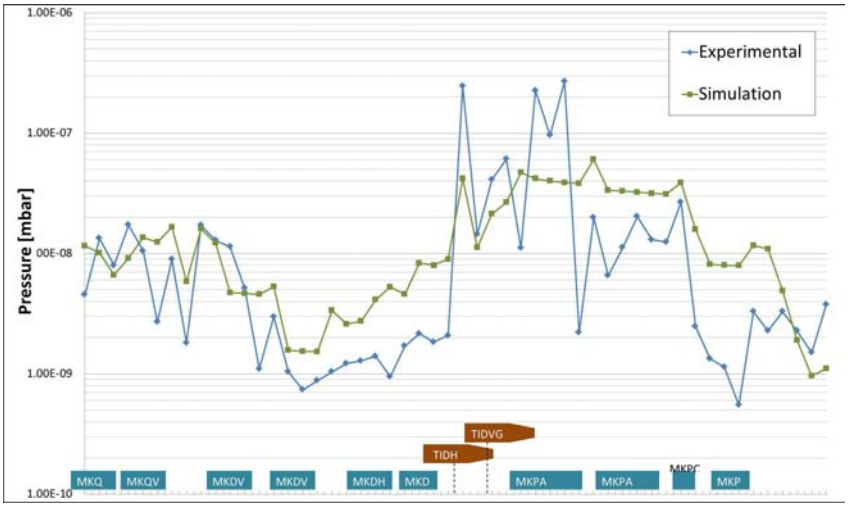

Figure 5.16: Pressure profile comparison between real data and LTspice model after 100 hours pump down.

The error between the simulation and the real data can be attributed to different reasons:

- Error in 3D models due to old drawings that could be different from the actual installed elements
- Presence of materials other than stainless steel in the beam line, as graphite, copper, tungsten etc.
- Error in gauges and pumps real measurement: the installed equipment is old and some gauges could be damaged.

5.2.4 Upgrade using NEG cartridges

Five NEG pumps have been added in the beam line close to the dumps (TIDVH and TIDVG): VPIC 11778, VPIC 11801, VPIC 11860, VPIC 11878 and VPIC 11902.
The analysis has been conducted for two different scenarios. In the first one (case A), NEG pumps were activated after a fixed time. In the second (case B), after NEG pumps activation, two ion pumps failure was simulated.

In scenario A, the pump-down was simulated for 1 year, with the ion pumps working all the time, and NEG activated 15 hours after the beginning of pumping. The aim of this simulation is to evaluate the saturation time of NEG cartridges. The pressure profiles as recorded from the gauges between the two dumps are shown in Fig. 5.17. Fig. 5.18 shows NEG pumping during 365 days. S_{NEG} stabilizes after

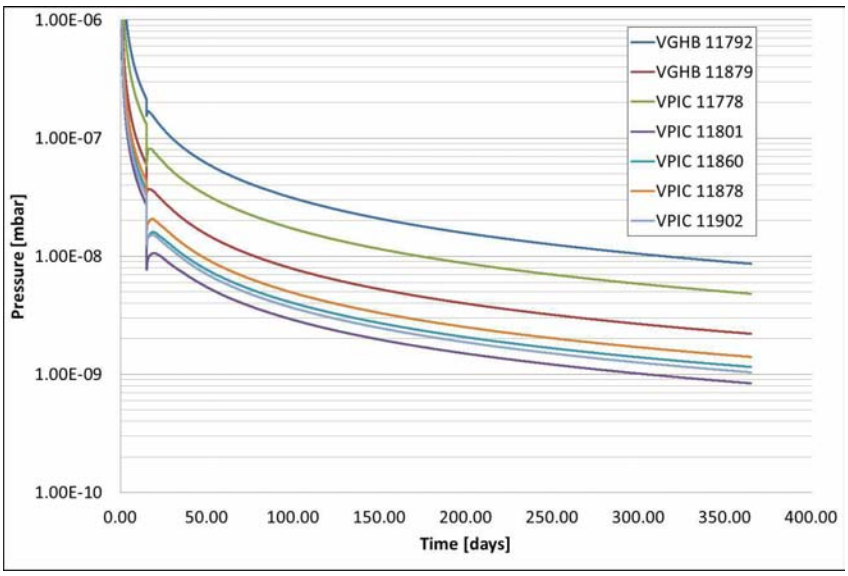

Figure 5.17: Pump-down curves for the ion pumps and gauges in the considered beam-line: NEG are activated after 15 days of pumping.

almost 100 days at a value between 40 and 50 ℓ/s. NEG 11778 pumping speed is lower than the others because of the higher flux at this location.

In scenario B, after NEG activation, two ion pumps (VPIC 11878 and VPIC 11902) were switched off after a time t_{OFF} of 30 days. The aim of this simulation was to understand if NEG cartridges can prevent the pressure increase due to ion pumps failure, and which saturation time would they have in this case.
The pressure profile comparison between with and without NEG case is shown in Fig. 5.19. NEG pumping lower the pressure "jump" by a factor 2 in the two considered ion pumps positions.
The pumping speed evolution of NEG cartridges is shown in Fig. 5.20. The higher flux on NEG cartridge causes a faster decrease in the pumping speed (in comparison with Fig. 5.18). For example, after 1 year, NEG 11902 pumps 26 ℓ/s in case B, instead of 43 ℓ/s in case A.

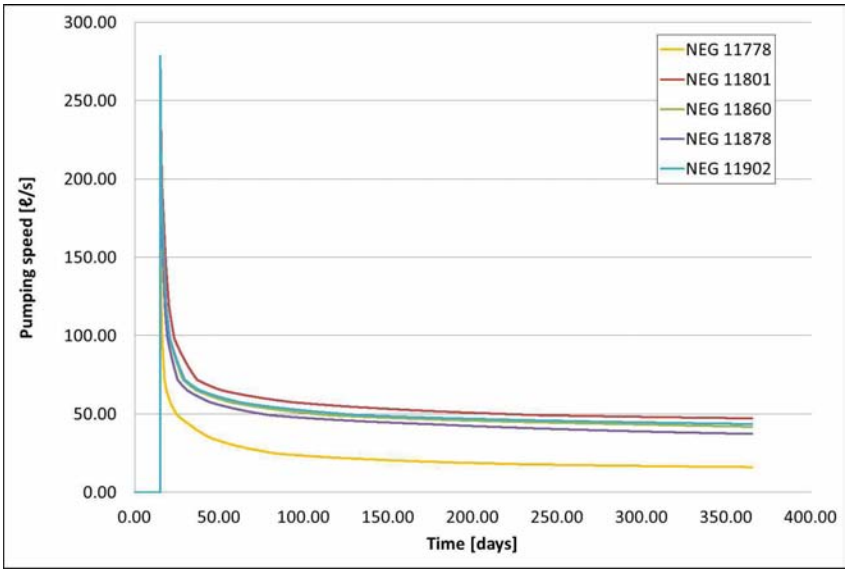

Figure 5.18: NEG pumping speed evolution (NEG are activated after 15 days of pumping).

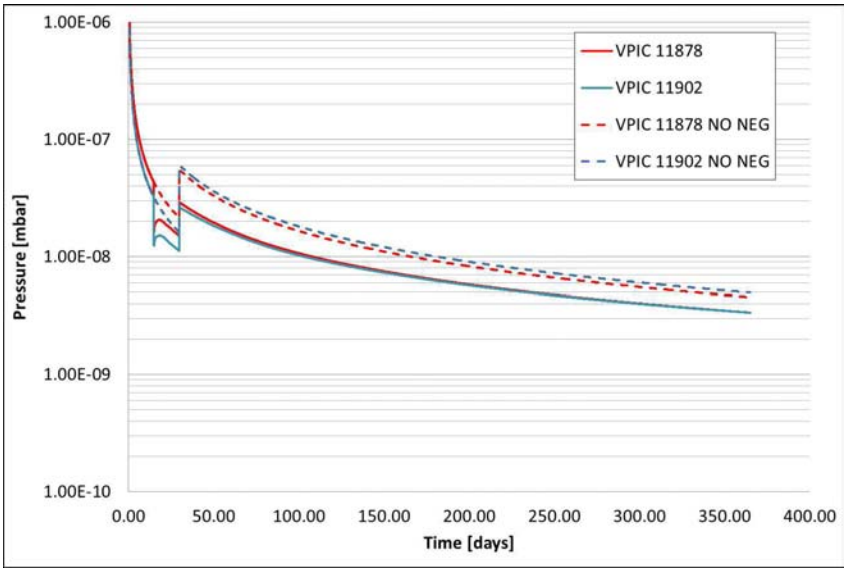

Figure 5.19: Pump-down curves at the position of the ion pumps VPIC 11878 and VPIC 11902 in case of failure after 30 days, with (solid line) and without (dashed line) activated NEG pump .

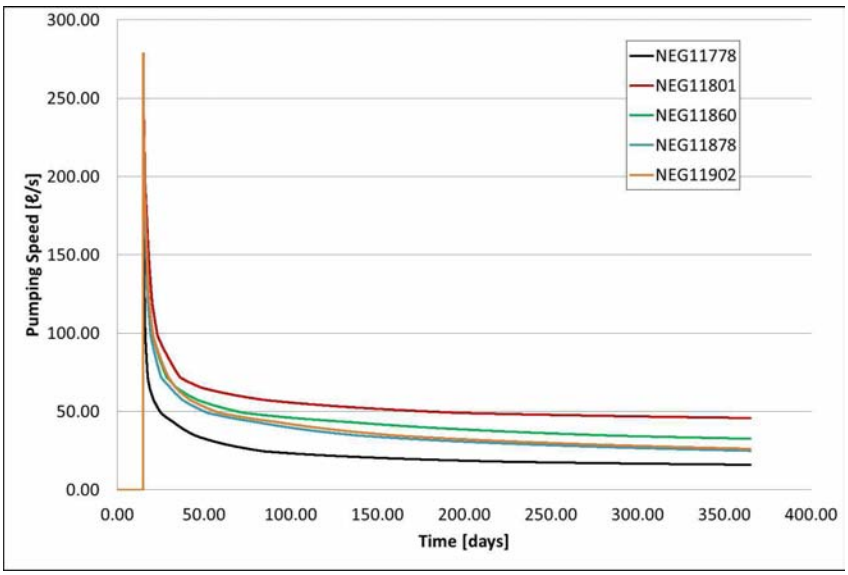

Figure 5.20: Pumping speed evolution of NEG pumps: VPIC 11878 and VPIC 11902 are switched off after 30 days of pumping.

Chapter 6

Conclusions

Water vapour desorption from metal vacuum systems has been studied throughout this project.

A numerical model for the calculation of pressure evolution has been presented. This model is based on the use of adsorption isotherms for water and on the diffusion model for hydrogen. In particular, Temkin, Freundlich and Sips isotherms have been analysed.
A set-up was built to compare experimental data with the numerical simulation. The behaviour of an untreated 316L stainless steel chamber has been successfully simulated for the subsequent experiments: constant temperature pump-down curves (at 20°C, 50°C, 100°C, 120°C and 150°C) and bake-outs at 150°C. The three isotherms showed similar results. It has been demonstrated that this similarity is due to their common hypothesis of constant energy distribution of the adsorption sites.

The behaviour of three differently treated stainless steel chambers has been compared to the outgassing value of an untreated chamber. The chambers underwent the following treatments: air-baking at 300°C, vacuum firing followed by electropolishing and silver-palladium coating. All substrates showed a 1/t behaviour at all temperatures. The difference between the outgassing values of the untreated and treated chambers increases with increasing temperature.

In LSS1 analysis, the effect of the addition of NEG lump pumps (CapaciTorr D1000) has been simulated in two situations: as an auxiliary pump during a pump-down, and as a recovery pump in case of a sudden stop of the main pumping system.

Appendix A

Vacuum equipment description

In this chapter are briefly described the main instruments used during the project.

A.1 Pressure gauges

The measurement range of different gauges is show in Fig. A.1.

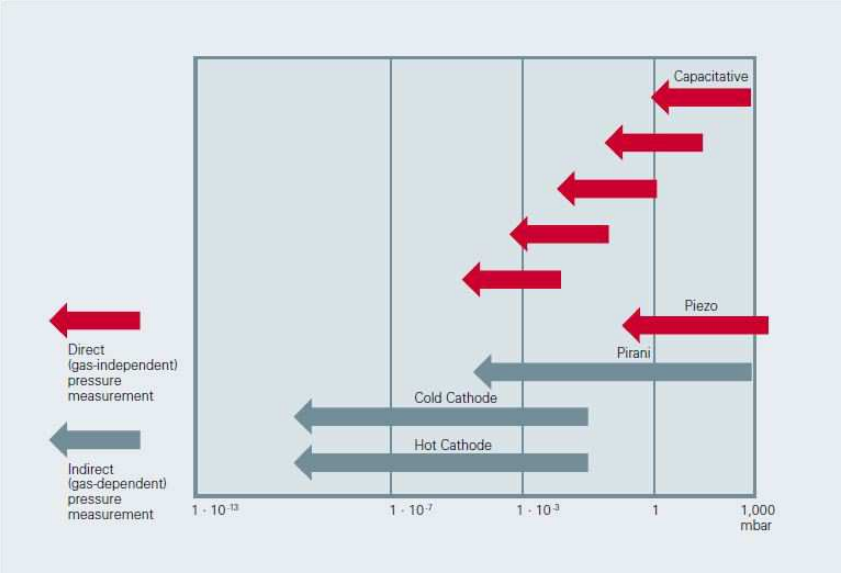

Figure A.1: Scheme of measurement ranges for main gauges [27].

A.1.1 Cold cathode gauge or Penning gauge

The pressure is measured through a gas discharge within a gauge head whereby the gas discharge is ignited by applying a high tension. The resulting ion current is output as a signal which is proportional to the prevailing pressure. The gas discharge is maintained also at low pressures with the aid of a magnet. The range of this gauges was 10^{-3} to 10^{-11} mbar.

A.1.2 Pirani gauge

The Pirani gauge head is based around a heated wire placed in a vacuum system, the electrical resistance of the wire being proportional to its temperature. At atmospheric pressure, gas molecules collide with the wire and remove heat energy from it (effectively cooling the wire). As gas molecules are removed (when the system is pumped down) there are less molecules and therefore less collisions. Fewer collisions mean that less heat is removed from the wire and so it heats up. As it heats up, its electrical resistance increases. A simple circuit utilising the wire detects the change in resistance and, once calibrated, can directly correlate the relationship between pressure and resistance. This effect only works in the pressure region from atmosphere to approx 10^{-3} mbar. That is why this kind of gauge is usually coupled with a Penning gauge.

A.1.3 Hot cathod gauge or Process Ion Gauge

A hot cathode gauge is based on gas ionization. Electrons emitted by the hot cathode ionize a number of molecules proportional to the pressure in the measure chamber. The ion collector (IC) collects the generated ion current I_+ and feeds it to the electro-meter amplifier of the measuring instrument. The ion current is dependent on the emission current I_e, the gas type and the gas pressure p according to the following relationship:

$$I_+ = I_e p C$$

with C the sensitivity of the gauge for a specific gas (it is 1 for N_2). The measurement range is between 10^{-2} mbar and 10^{-6} mbar.

A.1.4 Spinning Rotor Gauge

The Spinning Rotor Gauge (SRG) is a high-vacuum gauge that operates by measuring the amount of viscous drag on a magnetically-levitated spinning ball, which is directly related to the number of molecules in the chamber (i.e. pressure). Its accuracy specification of 1 % of reading is guaranteed over the range of 10^{-2} mbar to 5×10^{-7} mbar, and it can operate with reduced accuracy up to 1 mbar. Commonly it is used for calibration and metrology of other high-vacuum gauge sensors such as cold cathode and hot-filament ionization tubes. In our application the main goal was having a gauge that didn't interact with the gas by release of molecules (unlike cathode gauges) in order to not perturb the measured value of pressure.

A.2 Heating system

It's the system responsible of the experiment's temperature control. It is made by three parts:

- Rack for power supply and temperature control;
- Collars, jackets, heating stripes: all the objects that actually heat the chamber;

- Thermocouples: necessary to measure the temperature and control the power given to heating objects.

The insulation was granted by glass fiber blocked with aluminium paper.

A.3 Pumping system

Composed of a primary scroll pump and of a turbomolecular pump. The scroll pump was exploited to go from atmospheric pressure to 10^{-3} mbar, while from 10^{-3} to XHV molecules were removed with the turbomolecular pump. The former is a dry pump (no use of oil, i.e. no contamination) that uses two interleaving scrolls to pump the gas from the chamber. The latter belongs to the category of kinetic vacuum pumps. Their design is similar to that of a turbine. A multi-stage, turbine-like rotor with bladed disks rotates in a housing. Interposed inversely between the rotor disks are bladed stator disks having similar geometries. The particular system used in the experiment was an Agilent TPS Mobile.

Appendix B

CERN surface treatments procedures

B.1 Cleaning for UHV applications

Here below are the steps for CERN standard cleaning procedure for Stainless Steel:

1. Chemical degreasing with detergent and ultrasonic. Temperature: 50-60°C. Time: 30-60 minutes;
2. Rinsing with water;
3. Pickling. Temperature: 20°C. Time: 30-90 minutes;
4. Rinsing with water;
5. Neutralization with detergent and ultrasonic. Temperature: 50-60°C. Time: 30-60 minutes;
6. Rinsing with water;
7. Rinsing with demineralised water and alcohol;
8. Drying with clean compressed air.

B.2 Electropolishing

Here below are the steps for CERN standard electropolishing procedure:

1. Ultrasonic cleaning in alkaline detergent at 50°C for 30-60 minutes; the detergent is NGL 17-40 (supplied by Cleaning Technologies) at concentration of 10 g/l;
2. Rinsing in tap water;
3. Electropolishing in Sulphuric Acid 210 ml/l + Phosphoric Acid 790 ml/l at 60°C. Current density 20 A/dm^2 (etching rate about 1.5 mm/min);

4. Rinsing in tap water;
5. Light acid attack: Chromic Acid 80 g/l + Sulphuric Acid 3 ml/l, at room temperature for about 10 seconds;
6. Rinsing in tap water;
7. Rinsing with deionised water (resistivity>= $1M\Omega$cm);
8. Rinsing with ethylic alcohol
9. Drying in air at 80°C.

Appendix C

Drawings and schemes for LSS1 model

Here are reported some of the drawings and figures used to model LSS1 section.
In Fig. C.2 the entire sector is represented.
In Fig. C.3 a focus is done on the dumps TIDVG and TIDH and on the pumps that underwent NEG cartridge upgrade.
Finally, the model as seen by LTspice is shown in Fig. C.1.

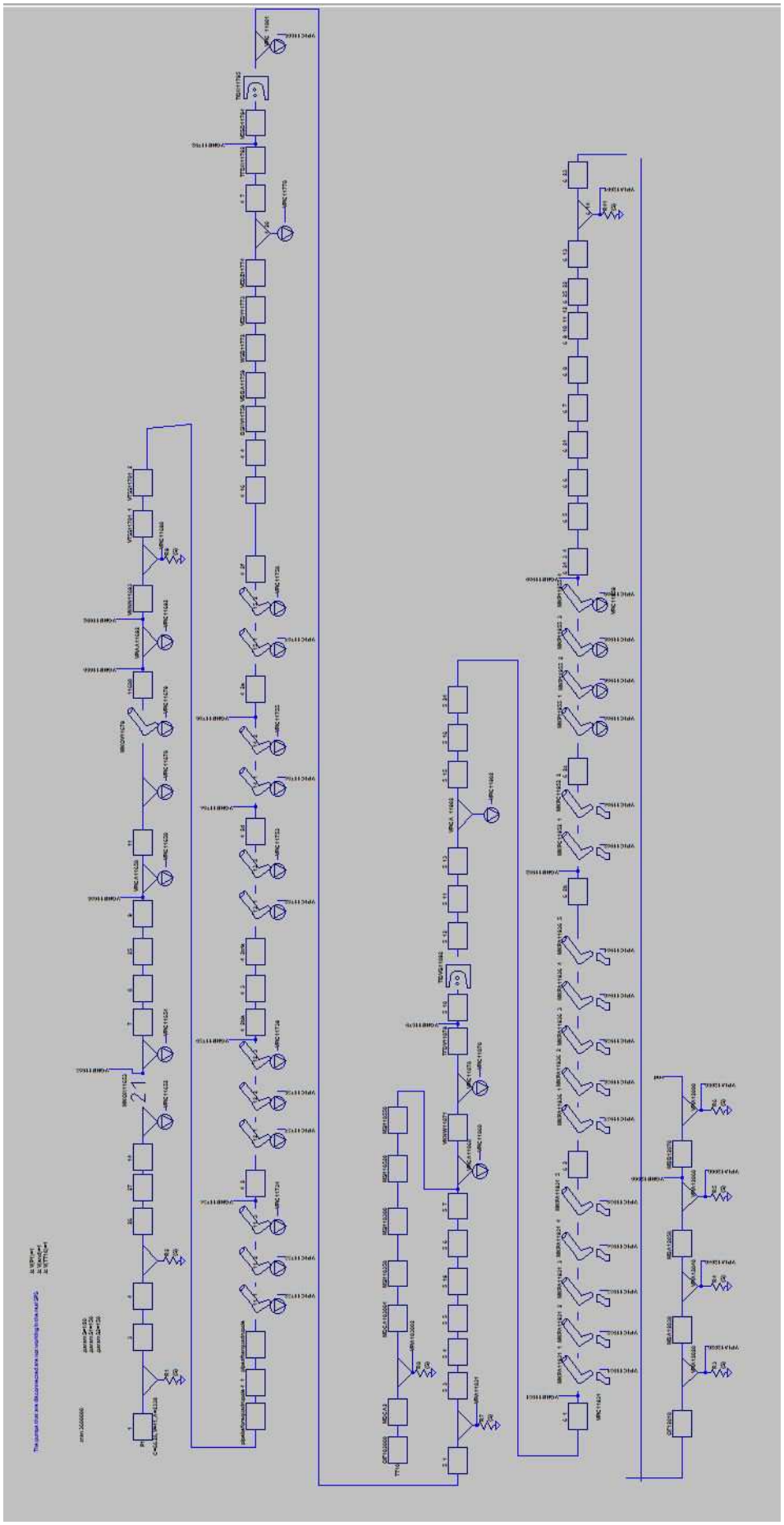

Figure C.1: BA1 network

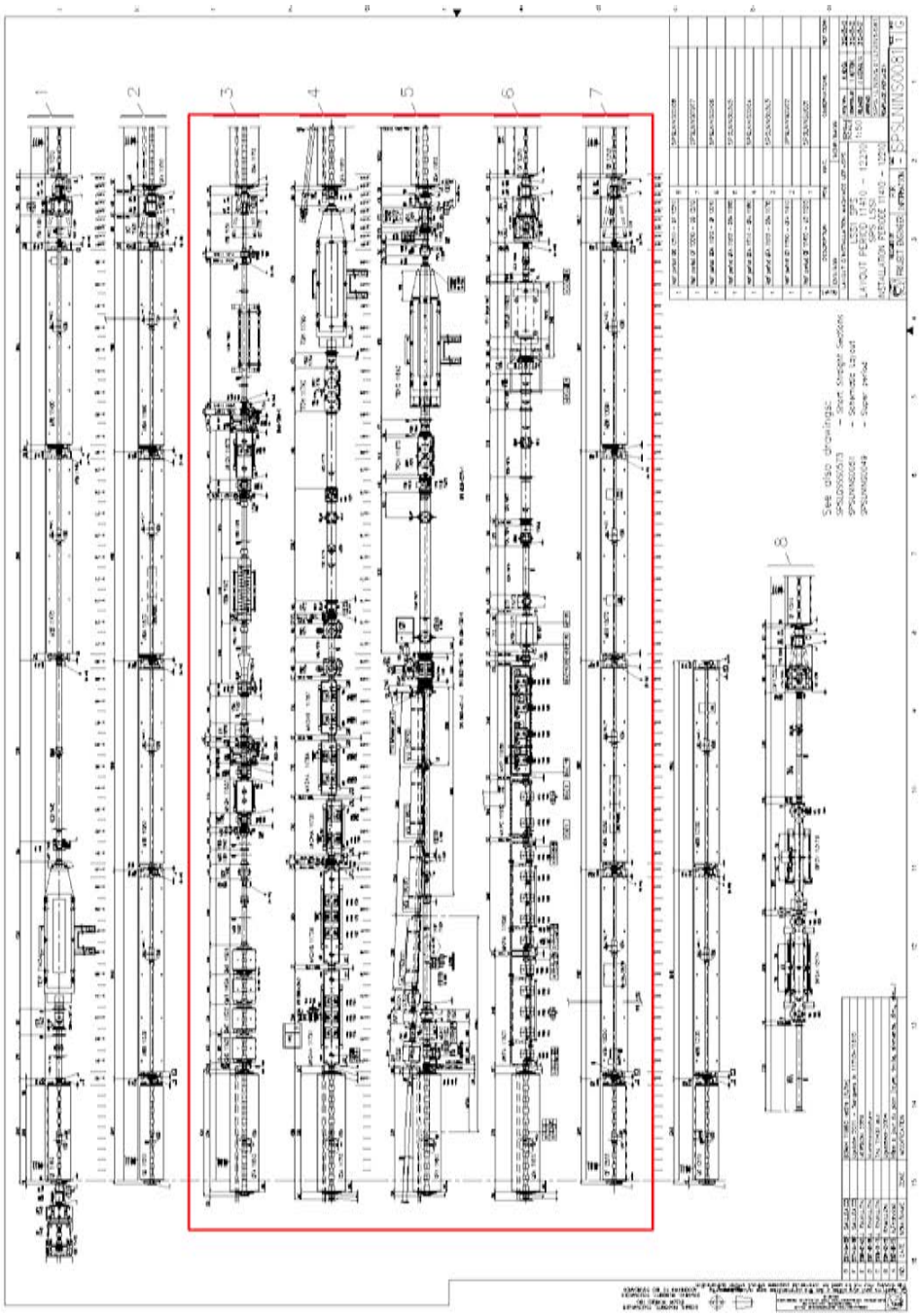

Figure C.2: BA1 global drawing: the simulated part is delimited by the red box.

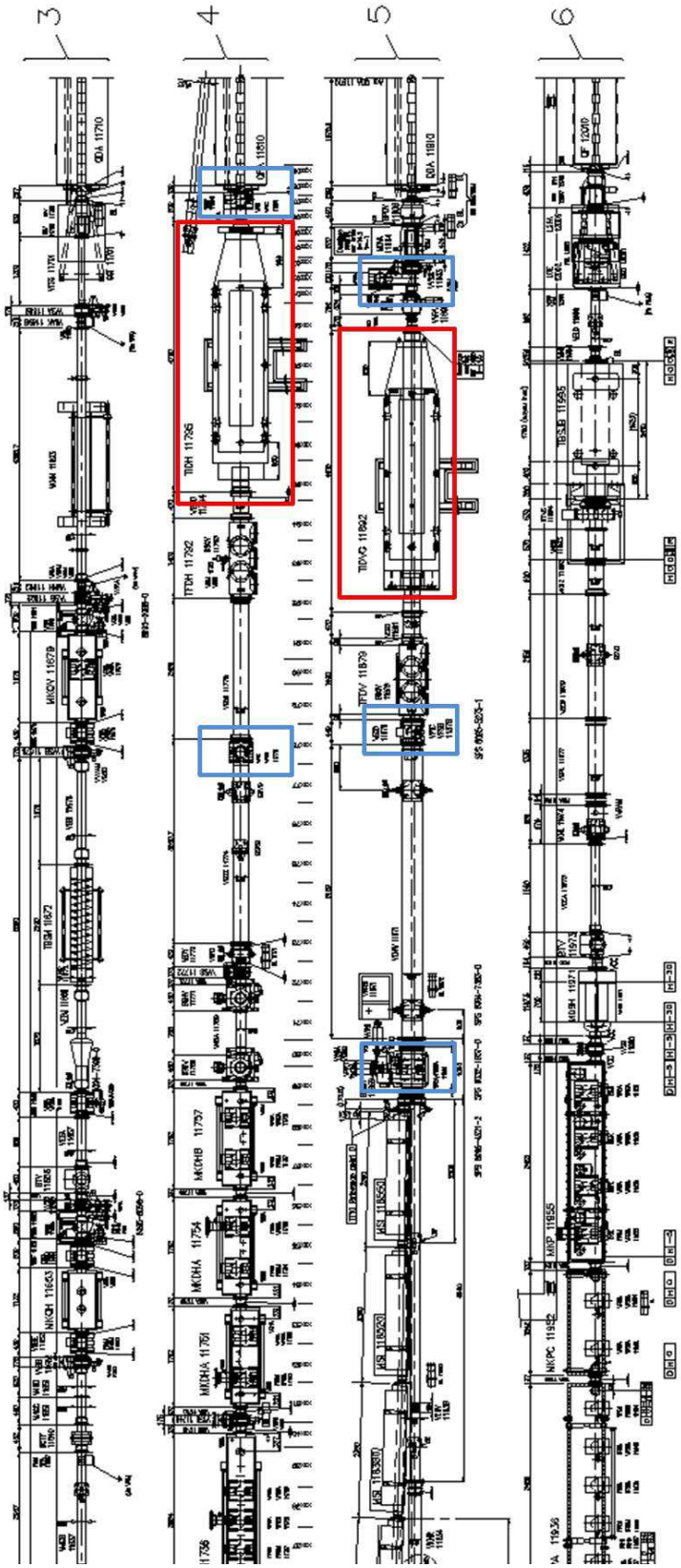

Figure C.3: Zoom on TIDH and TIDVG (red boxes), and on the 5 ion pumps upgraded with NEG lump pumps (blue boxes).

Bibliography

[1] M. Bernardini, S. Braccini, R. De Salvo, A. Di Virgilio, A. Gaddi, A. Gennai, G. Genuini, A. Giazotto, G. Losurdo, H. B. Pan, A. Pasqualetti, D. Passuello, P. Popolizio, F. Raffaelli, G. Torelli, Z. Zhang, C. Bradaschia, R. Del Fabbro, I. Ferrante, F. Fidecaro, P. La Penna, S. Mancini, R. Poggiani, P. Narducci, A. Solina, and R. Valentini. Air bake-out to reduce hydrogen outgassing from stainless steel. *Journal of Vacuum Science & Technology A*, 16(1):188–193, January 1998.

[2] Paolo Chiggiato. Influence of thermal and surface treatments on the outgassing of the austenitic stainless steels studied by thermal and electron stimulated desorption, 2002.

[3] Paolo Chiggiato. Vacuum technology for particle accelerators, 2010.

[4] Inkyu Chun, Boklae Cho, and Sukmin Chung. Outgassing rate characteristic of a stainlesssteel extreme high vacuum system. *Journal of Vacuum Science & Technology A*, 14(4):2636–2640, July 1996.

[5] P. Clausing. The flow of highly rarefied gases through tubes of arbitrary length. *Journal of Vacuum Science & Technology*, 8(5):636–646, September 1971.

[6] D. H. Davis. Monte carlo calculation of molecular flow rates through a cylindrical elbow and pipes of other shapes. *Journal of Applied Physics*, 31(7):1169–1176, March 1960.

[7] H. F. Dylla, D. M. Manos, and P. H. LaMarche. Correlation of outgassing of stainless steel and aluminum with various surface treatments. *Journal of Vacuum Science & Technology A*, 11(5):2623–2636, September 1993.

[8] Mike Engelhardt. LTSpice, February 2014.

[9] H. Freundlich. Of the adsorption of gases. section II. kinetics and energetics of gas adsorption. introductory paper to section II. *Trans. Faraday Soc.*, 28(0):195–201, January 1932.

[10] Cedric Garion. On bake-out related design costs for LHC accelerator., March 2014.

[11] SAES Getter. CapaciTorr pumps MK5 series, 2012.

[12] Y. S. Ho, J. F. Porter, and G. McKay. Equilibrium isotherm studies for the sorption of divalent metal ions onto peat: Copper, nickel and lead single component systems. *Water, Air, & Soil Pollution*, 141(1-4):1–33, November 2002.

[13] G. Horikoshi. Physical understanding of gas desorption mechanisms. *Journal of Vacuum Science & Technology A*, 5(4):2501–2506, July 1987.

[14] D. E. Jiang and Emily A. Carter. Diffusion of interstitial hydrogen into and through bcc fe from first principles. *Phys. Rev. B*, 70(6):064102, August 2004.

[15] B. H. Hameed K. Y. Foo. Insights into the modeling of adsorption isotherm systems. *Chemical Engineering Journal*, 156(1):2–10, 2010.

[16] K. Kanazawa. Analysis of pumping down process. *Journal of Vacuum Science & Technology A*, 7(6):3361–3370, November 1989.

[17] R. Kersevan and J.-L. Pons. Introduction to MOLFLOW+: new graphical processing unit-based monte carlo code for simulating molecular flows and for calculating angular coefficients in the compute unified device architecture environment. *Journal of Vacuum Science & Technology A*, 27(4):1017–1023, June 2009.

[18] K. Vasanth Kumar, Juan Carlos Serrano-Ruiz, Hileia K. S. Souza, Ana Maria Silvestre-Albero, and Vinod Kumar Gupta. Site energy distribution function for the sips isotherm by the condensation approximation method and its application to characterization of porous materials. *J. Chem. Eng. Data*, 56(5):2218–2224, May 2011.

[19] J. M Lafferty. *Foundations of vacuum science and technology.* Wiley, New York, 1998.

[20] Irving Langmuir. THE ADSORPTION OF GASES ON PLANE SURFACES OF GLASS, MICA AND PLATINUM. *J. Am. Chem. Soc.*, 40(9):1361–1403, September 1918.

[21] Minxu Li and H. F. Dylla. Model for the outgassing of water from metal surfaces. *Journal of Vacuum Science & Technology A*, 11(4):1702–1707, July 1993.

[22] Minxu Li and H. F. Dylla. Model for water outgassing from metal surfaces. II. *Journal of Vacuum Science Technology A: Vacuum, Surfaces, and Films*, 12(4):1772–1777, 1994.

[23] Minxu Li and H. F. Dylla. Modeling of water outgassing from metal surfaces (III). *Journal of Vacuum Science Technology A: Vacuum, Surfaces, and Films*, 13(4):1872–1878, 1995.

[24] A. Malek and S. Farooq. Comparison of isotherm models for hydrocarbon adsorption on activated carbon. *AIChE Journal*, 42(11):31913201, 1996.

[25] Alice Michet. Statistiques concernant les interventions ralises par IVM sur les injecteurs en 2012, November 2012.

[26] L. Ter Minassian-Saraga. Thin films including layers: terminology in relation to their preparation and characterization (IUPAC recommendations 1994). *Pure and Applied Chemistry*, 66(8), January 1994.

[27] Vacuum Pfeiffer. Vacuum technology know how, March 2009.

[28] P. A. Redhead. Modeling the pumpdown of a reversibly adsorbed phase. i. monolayer and submonolayer initial coverage. *Journal of Vacuum Science & Technology A*, 13(2):467–475, March 1995.

[29] P. A. Redhead. Modeling the pumpdown of a reversibly adsorbed phase. II. multilayer coverage. *Journal of Vacuum Science & Technology A*, 13(6):2791–2796, November 1995.

[30] Ron Reid. Vacuum science and technology in accelerators, 2010.

[31] Donald J. Santeler. Exit loss in viscous tube flow. *Journal of Vacuum Science & Technology A*, 4(3):348–352, May 1986.

[32] Robert Sips. On the structure of a catalyst surface. *The Journal of Chemical Physics*, 16(5):490–495, January 1948.

[33] Robert Sips. On the structure of a catalyst surface. II. *The Journal of Chemical Physics*, 18(8):1024–1026, March 1950.

[34] Agilent Technologies. VacIon plus 300 pumps user manual, 2011.

[35] A.Ya. Temkin. A contribution to non-equilibrium chemical kinetics. *Chemical Physics*, 83(12):105–114, January 1984.

[36] A.Ya. Temkin. A contribution to non-equilibrium chemical kinetics. II. strongly non-equilibrium hot reactions in liquids and solids. *Chemical Physics*, 99(2):223–237, October 1985.

[37] L Westerberg, B Hjrvarsson, E Walln, and A Mathewson. Hydrogen content and outgassing of air-baked and vacuum-fired stainless steel. *Vacuum*, 48(79):771–773, September 1997.

[38] Nagamitsu Yoshimura, Haruo Hirano, Tomoshige Sato, Ichiro Ando, and Sachiko Adachi. Outgassing characteristics and microstructure of a vacuum fired (1050 C) stainless steel surface. *Journal of Vacuum Science & Technology A*, 9(4):2326–2330, July 1991.

[39] Nicolas Zelko. Private talk with nicolas zelko., January 2014.